ACCURATE AND PRECISE CALIBRATION OF ADVANCED LIGO

DETECTORS IN THE ERA OF GRAVITATIONAL WAVE ASTRONOMY

by

SUDARSHAN KARKI

A DISSERTATION

Presented to the Department of Physics
and the Graduate School of the University of Oregon
in partial fulfillment of the requirements
for the degree of
Doctor of Philosophy

March 2019

DISSERTATION APPROVAL PAGE

Student: Sudarshan Karki

Title: Accurate and Precise Calibration of Advanced LIGO Detectors in the Era of Gravitational Wave Astronomy

This dissertation has been accepted and approved in partial fulfillment of the requirements for the Doctor of Philosophy degree in the Department of Physics by:

James Brau	Chair
Raymond Frey	Advisor
Robert Schofield	Core Member
Richard L. Savage	Core Member
Brian Smith	Core Member
Dejing Duo	Institutional Representative

and

Janet Woodruff-Borden	Dean of the Graduate School

Original approval signatures are on file with the University of Oregon Graduate School.

Degree awarded March 2019

DISSERTATION ABSTRACT

Sudarshan Karki

Doctor of Philosophy

Department of Physics

March 2019

Title: Accurate and Precise Calibration of Advanced LIGO Detectors in the Era of Gravitational Wave Astronomy

The first direct detection of gravitational waves in 2015, and the multiple detections that followed ushered in the era of gravitational-wave astronomy. With these developments, the focus of the gravitational-wave community shifted from *detection* to *precision* measurement, requiring a factor of ten improvement in calibration accuracy to maximize the astrophysical information that can be extracted from these detected signals.

This dissertation discusses the implementation and characterization of a radiation-pressure-based calibration system called the Photon calibrator that is used as the primary calibration reference for the Advanced LIGO detectors. It also discusses the techniques and procedures used to realize sub-percent accuracy calibration of *absolute displacement fiducials* introduced using the Photon calibrator system during Advanced LIGO's first and second observing runs.

Using the Photon calibrator systems, frequency dependent calibration of the interferometer responses was achieved at the level of 2-3% in magnitude and 3-5 degrees in phase across the LIGO detection band. This level of calibration accuracy has already played a significant role in extracting astrophysical parameters from LIGO's detections. With the LIGO and Virgo detectors operating at design

sensitivity, updated rate estimates indicate that measurement of the Hubble constant with gravitational waves with 1% accuracy will be possible within the next decade. This will require absolute amplitude calibration of the detectors at the sub-1% level. This dissertation also discusses the improvements that have been implemented in the Photon calibrator systems that will reduce the uncertainty in absolute displacement to below 0.5%.

The gravitational waves from the post-merger phase of binary neutron stars are expected to contain interesting features at frequencies up to few kHz, carrying rich information about neutron-star astrophysics. This dissertation discusses the calibration errors introduced by test mass deformations caused by calibration forces at frequencies above 1 kHz. The errors, estimated using Finite Element Analysis, is in reasonable agreement with measurement results in the 1 to 5 kHz band. These investigations have enabled the reduction of calibration uncertainty at these frequencies, which should enhance our ability to decipher the neutron star astrophysics encoded in the gravitational wave signals from the post-merger phase.

This dissertation includes previously published co-authored material.

CURRICULUM VITAE

NAME OF AUTHOR: Sudarshan Karki

GRADUATE AND UNDERGRADUATE SCHOOLS ATTENDED:
    University of Oregon, Eugene, OR
    University of Missouri-Kansas City, Kansas City, MO

DEGREES AWARDED:
    Doctor of Philosophy, Physics, 2019, University of Oregon
    Masters in Science, Physics, 2015, University of Oregon
    Bachelors in Science, Physics, 2010, University of Missouri Kansas City(UMKC)

AREAS OF SPECIAL INTEREST:
    Gravitational-wave physics, Data-analysis, Model-building

PROFESSIONAL EXPERIENCE:

    LIGO Fellow, LIGO-Hanford, Aug 2014- Dec 2016

    Graduate Research Assistant, University of Oregon, Aug 2014- Mar 2019

    Graduate Teaching Assistant, University of Oregon, Sept 2012- Aug 2014

    Research Associate, University of Missouri-KC, Jan 2011 Aug 2012

    Student Research Assistant, University of Missouri-KC, May 2008 Dec 2010

GRANTS, AWARDS AND HONORS:

    Special Breakthrough Prize-Fundamental Physics, Milner Foundation, 2016

    Guber Cosmology Prize, Guber Foundation, 2016

    LIGO Fellowship, LIGO-Caltech, 2014

    K. F. Cheng Physics Scholarship, UMKC, 2010

    K. L. Cheng Physics Scholarship, UMKC, 2009

    SEARCH Grant, Teaching Physics in High School, UMKC, 2008

PUBLICATIONS:

S. Karki, et al. The Advanced LIGO Photon Calibrators. Review of Scientific Instruments, 87:114503, 2016.

D. Tuyenbayev, et al. Improving LIGO calibration accuracy by tracking and compensating for slow temporal variations. Classical and Quantum Gravity, 34(1):015002, 2017.

C. Cahillane, et al. Calibration uncertainty for Advanced LIGOs first and second observing runs. Phys. Rev. D, 96:102001, 2017.

C. Biwer, et al. Validating gravitational-wave detections: The advanced LIGO hardware injection system. Phys. Rev. D, 95:062002, 2017.

A. D. Viets, et al. Reconstructing the calibrated strain signal in the Advanced LIGO detectors. Classical and Quantum Gravity, 35(9):095015, 2018.

B. P. Abbott et al. GWTC-1: A Gravitational-Wave Transient Catalog of Compact Binary Mergers Observed by LIGO and Virgo during the First and Second Observing Runs. Submitted to PRX, 1811.12907, 2019.

B. P. Abbott et al. Binary Black Hole Population Properties Inferred from the First and Second Observing Runs of Advanced LIGO and Advanced Virgo. Submitted to ApJ 1811.12940, 2019.

B. P. Abbott et al. Tests of General Relativity with GW170817. Submitted to PRL, 1811.00364, 2019.

B. P. Abbott et al. Search for gravitational waves from a long-lived remnant of the binary neutron star merger GW170817. Submitted to ApJ 1810.02581, 2019

B. P. Abbott et al. Properties of the binary neutron star merger GW170817. Phys. Rev. X 9, 011001, 2019

B. P. Abbott et al. GW170817: Measurements of neutron star radii and the equation of state Phys. Rev. Lett. 121, 161101 2018

B. P. Abbott et al. Search for Tensor, Vector, and Scalar Polarizations in the Stochastic Gravitational-Wave Background. Phys. Rev. Lett., 120(20):201102, 2018.

B. P. Abbott et al. Full Band All-sky Search for Periodic Gravitational Waves in the O1 LIGO Data. Phys. Rev., D97(10):102003, 2018.

B. P. Abbott et al. Constraints on cosmic strings using data from the first advanced LIGO observing run. Phys. Rev. D, 97:102002, May 2018.

P. B. Covas et al. Identification and mitigation of narrow spectral artifacts that degrade searches for persistent gravitational waves in the first two observing runs of advanced ligo. Phys. Rev. D, 97:082002, Apr 2018.

B. P. Abbott et al. GW170817: Implications for the Stochastic Gravitational-Wave Background from Compact Binary Coalescences. Phys. Rev. Lett., 120(9):091101, 2018.

B. P. Abbott et al. All-sky search for long-duration gravitational wave transients in the first Advanced LIGO observing run. Class. Quant. Grav., 35(6):065009, 2018.

B. P. Abbott et al. Effects of data quality vetoes on a search for compact binary coalescences in Advanced LIGOs first observing run. Class. Quant. Grav., 35(6):065010, 2018.

B. P. Abbott et al. First search for nontensorial gravitational waves from known pulsars. Phys. Rev. Lett., 120(3):031104, 2018.

B. P. Abbott et al. First narrow-band search for continuous gravitational waves from known pulsars in advanced detector data. Phys. Rev., D96(12):122006, 2017.

B. P. Abbott et al. GW170608:Observation of a 19-solar-mass Binary Black Hole Coalescence. Astrophys. J., 851(2):L35, 2017.

B. P. Abbott et al. First low-frequency Einstein@Home all-sky search for continuous gravitational waves in Advanced LIGO data. Phys. Rev., D96(12):122004, 2017.

B. P. Abbott et al. Search for Post-merger Gravitational Waves from the Remnant of the Binary Neutron Star Merger GW170817. Astrophys. J., 851(1):L16, 2017.

B. P. Abbott et al. On the Progenitor of Binary Neutron Star Merger GW170817. Astrophys. J., 850(2):L40, 2017.

B. P. Abbott et al. Estimating the Contribution of Dynamical Ejecta in the Kilonova Associated with GW170817. Astrophys. J., 850(2):L39, 2017.

B. P. Abbott et al. Search for High-energy Neutrinos from Binary Neutron Star Merger GW170817 with ANTARES, IceCube, and the Pierre Auger Observatory. Astrophys. J., 850(2):L35, 2017.

B. P. Abbott et al. A gravitational-wave standard siren measurement of the Hubble constant. Nature, 551(7678):8588, 2017.

B. P. Abbott et al. Gravitational Waves and Gamma-rays from a Binary Neutron Star Merger: GW170817 and GRB 170817A. Astrophys. J., 848(2):L13, 2017.

B. P. Abbott et al. Multi-messenger Observations of a Binary Neutron Star Merger. Astrophys. J., 848(2):L12, 2017.

B. P. Abbott et al. Gw170817: Observation of gravitational waves from a binary neutron star inspiral. Phys. Rev. Lett., 119:161101, Oct 2017.

B. P. Abbott et al. GW170814: A Three-Detector Observation of Gravitational Waves from a Binary Black Hole Coalescence. Phys. Rev. Lett., 119(14):141101, 2017.

B. P. Abbott et al. Upper Limits on Gravitational Waves from Scorpius X-1 from a Model-Based Cross-Correlation Search in Advanced LIGO Data. Astrophys. J., 847(1):47, 2017.

B. P. Abbott et al. All-sky Search for Periodic Gravitational Waves in the O1 LIGO Data. Phys. Rev., D96(6):062002, 2017.

B. P. Abbott et al. Search for intermediate mass black hole binaries in the first observing run of Advanced LIGO. Phys. Rev., D96(2):022001, 2017.

B. P. Abbott et al. Search for gravitational waves from Scorpius X-1 in the first Advanced LIGO observing run with a hidden Markov model. Phys. Rev., D95(12):122003, 2017.

B. P. Abbott et al. GW170104: Observation of a 50-Solar- Mass Binary Black Hole Coalescence at Redshift 0.2. Phys. Rev. Lett., 118(22):221101, 2017.

B. P. Abbott et al. Search for Gravitational Waves Associated with Gamma- Ray Bursts During the First Advanced LIGO Observing Run and Implications for the Origin of GRB 150906B. Astrophys. J., 841(2):89, 2017.

T. D. Abbott et al. Search for continuous gravitational waves from neutron stars in globular cluster NGC 6544. Phys. Rev., D95(8):082005, 2017.

B. P. Abbott et al. Effects of waveform model systematics on the interpretation of GW150914. Class. Quant. Grav., 34(10):104002, 2017.

B. P. Abbott et al. First search for gravitational waves from known pulsars with Advanced LIGO. Astrophys. J., 839(1):12, 2017.

B. P. Abbott et al. Upper Limits on the Stochastic Gravitational-Wave Background from Advanced LIGOs First Observing Run. Phys. Rev. Lett., 118(12):121101, 2017.

B. P. Abbott et al. Directional Limits on Persistent Gravitational Waves from Advanced LIGOs First Observing Run. Phys. Rev. Lett., 118(12):121102, 2017.

B. P. Abbott et al. All-sky search for short gravitational-wavebursts in the first Advanced LIGO run. Phys. Rev., D95(4):042003, 2017.

B. P. Abbott et al. Exploring the Sensitivity of Next Generation Gravitational Wave Detectors. Class. Quant. Grav., 34(4):044001, 2017.

B. P. Abbott et al. The basic physics of the binary black hole merger GW150914. Annalen Phys., 529(1-2):1600209, 2017.

B. P. Abbott et al. Supplement: The Rate of Binary Black Hole Mergers Inferred from Advanced LIGO Observations Surrounding GW150914. Astrophys. J. Suppl., 227(2):14, 2016.

B. P. Abbott et al. The Rate of Binary Black Hole Mergers Inferred from Advanced LIGO Observations Surrounding GW150914. Astrophys. J., 833(1):L1, 2016.

B. P. Abbott et al. Upper Limits on the Rates of Binary Neutron Star and Neutron Starblack Hole Mergers From Advanced Ligos First Observing run. Astrophys. J., 832(2):L21, 2016.

B. P. Abbott et al. Results of the deepest all-sky survey for continuous gravitational waves on LIGO S6 data running on the Einstein@Home volunteer distributed computing project. Phys. Rev., D94(10):102002, 2016.

B. P. Abbott et al. Binary Black Hole Mergers in the first Advanced LIGO Observing Run. Phys. Rev., X6(4):041015, 2016.

T. D. Abbott et al. Improved analysis of GW150914 using a fully spin precessing waveform Model. Phys. Rev., X6(4):041014, 2016.

B. P. Abbott et al. Directly comparing GW150914 with numerical solutions of Einsteins equations for binary black hole coalescence. Phys. Rev., D94(6):064035, 2016.

B. P. Abbott et al. Comprehensive all-sky search for periodic gravitational waves in the sixth science run LIGO data. Phys. Rev., D94(4):042002, 2016.

B. P. Abbott et al. Supplement: Localization and broadband follow-up of the gravitational-wave transient GW150914. Astrophys. J. Suppl., 225(1):8, 2016.

B. P. Abbott et al. Localization and broadband follow-up of the gravitational-wave transient GW150914. Astrophys. J., 826(1):L13, 2016.

B. P. Abbott et al. GW151226: Observation of Gravitational Waves from a 22-Solar-Mass Binary Black Hole Coalescence. Phys. Rev. Lett., 116(24):241103, 2016.

B. P. Abbott et al. Properties of the Binary Black Hole Merger GW150914. Phys. Rev. Lett., 116(24):241102, 2016.

B. P. Abbott et al. Observing gravitational-wave transient GW150914 with minimal assumptions. Phys. Rev., D93(12):122004, 2016.

B. P. Abbott et al. GW150914: First results from the search for binary black hole coalescence with Advanced LIGO. Phys. Rev., D93(12):122003, 2016.

B. P. Abbott et al. Characterization of transient noise in Advanced LIGO relevant to gravitational wave signal GW150914. Class. Quant. Grav., 33(13):134001, 2016.

B. P. Abbott et al. GW150914: Implications for the stochastic gravitational wave background from binary black holes. Phys. Rev. Lett., 116(13):131102, 2016.

B. P. Abbott et al. GW150914: The Advanced LIGO Detectors in the Era of First Discoveries. Phys. Rev. Lett., 116(13):131103, 2016.

B. P. Abbott et al. Astrophysical Implications of the Binary Black-Hole Merger GW150914. Astrophys. J., 818(2):L22, 2016.

B. P. Abbott et al. Observation of Gravitational Waves from a Binary Black Hole Merger. Phys. Rev. Lett., 116(6):061102, 2016.

B. P. Abbott et al. Prospects for Observing and Localizing Gravitational-Wave Transients with Advanced LIGO, Advanced Virgo and KAGRA. Living Rev. Rel., 21:3, 2018.

ACKNOWLEDGEMENTS

I owe my gratitude to many people who made this journey a fun ride and were also there to guide me when the going got tough.

I would like to begin by thanking my advisor Prof. Raymond Frey (Ray) and Dr. Richard Savage (Rick) for providing continued support. Ray, thank you for believing in me and encouraging me to work at the LIGO site from the very beginning, providing me valuable guidance throughout graduate school. Rick, thank you for taking me under your wing and guiding me on my research. This would not have been possible without you. Thank you Prof. James Brau for willing to chair my dissertation committee and provide valuable input throughout the dissertation writing process. Thank you to all the dissertation committee members, your input has been valuable.

I would also like to thank my undergraduate advisor, Prof. Anthony Caruso at University of Missouri, for letting me play with and help build the cool tools in your Thin Film lab even though I had zero prior experience.

I am grateful to many brilliant people, whom I met at LIGO sites, who were patient with me and took time to teach me about different aspects of the interferometer. I would also like thank all the members of the LIGO calibration group who I got chance to work closely with and learned a lot in the process.

A very special gratitude to D. Tuyenbayev for bearing with me in the same office and working together on the Photon calibrator system, establish scheme to measure the responsivity ratios between the power sensors among many others. I would also like to thank N. DeLillo and S. Kandhasamy, for spearheading the COMSOL modeling setup and initial analysis that has been valuable part of Chapter 5 of this dissertation.

To my near and dear friends scattered around the world, thank you for being there whenever I needed a friend, in celebration and hard times. Special thank you to all the friends I made during my time at LIGO, at several collaboration meetings, and at University of Oregon, you have made this a worth-while experience, with all the memories and adventures.

And finally, thank you all my family members, this journey would not have been possible without your support. Special thank you to Priyata Shrestha, for your support and encouragement.

This is to you dad and mom.

TABLE OF CONTENTS

xvii

LIST OF TABLES

CHAPTER 1

GRAVITATIONAL WAVES

On the 14th of September 2015, the second generation Laser Interferometer Gravitational-wave Observatory (LIGO), referred to as Advanced LIGO, made the first direct detection of gravitational waves from the merger of a pair of black holes. The direct detection of the gravitational waves, which were predicted by the theory of general relativity formulated a century ago, was in itself a remarkable feat. However, additional gravitational-wave detections have been made since then, marking the beginning of the era of gravitational-wave astronomy, and enabling astronomers to use gravitational waves to probe the physics of the dense matter objects that produce these waves. Among the detections that Advanced LIGO made during its first and second observing runs, a signal from a pair of merging neutron stars created great interest among astronomers and scientists. The event was followed up by more than seventy electromagnetic observatories and more than one thousand scientists, leading to the detection of multiple signals in electromagnetic frequencies emitted by the source of this event. This was the first joint detection of gravitational and electromagnetic waves from a single event, giving birth to multi-messenger astronomy. This single event helped us to understand the answers to some of the long-sought questions within the scientific community, ranging from the source of Gamma Ray Bursts (GRBs) to the speed of propagation of gravitational waves and whether the hypothesized kilonova are the source of heavy metals like gold and platinum. The Advanced LIGO interferometers will undoubtedly be able to detect more of these signals in the future and allow us to probe the physics of the dense matter inside these neutron stars, of which we have limited understanding. In this dissertation we

describe a crucial aspect for GW detection – the calibration of the detector response in physical units, thus enabling quantitative interpretation of the gravitational-wave detections for astrophysics.

1.1. Theory of Gravitational waves

1.1.1. Special Theory of Relativity

Einstein introduced the special theory of relativity in 1905 [1], combining the theory of electromagnetism and Newton's equations of motion, to describe the dynamics of moving bodies more accurately. In Newtonian theory, time and space are absolute quantities for all observers. With the theory of special relativity, Einstein changed the notion of absolute time and space. He postulated that space and time are not separate entities but are closely tied together in what he termed as *"spacetime."* In this theory, a spacetime interval is an invariant quantity and in free space is defined by

$$ds^2 = -c^2dt^2 + dx^2 + dy^2 + dz^2 \tag{1.1a}$$

$$= \eta_{\mu\nu}dx^\mu dx^\nu \tag{1.1b}$$

where $dx^\mu = (cdt, dx, dy, dz)$ and $\eta_{\mu\nu}$ is represented by the Minkowski metric,

$$\eta_{\mu\nu} = \begin{bmatrix} -1 & 0 & 0 & 0 \\ 0 & 1 & 0 & 0 \\ 0 & 0 & 1 & 0 \\ 0 & 0 & 0 & 1 \end{bmatrix} \tag{1.2}$$

Because it is described by the Minkowski metric, special relativity operates in the realm of flat Euclidean spacetime where the effect of gravitational fields on spacetime itself is ignored.

1.1.2. General Theory of Relativity

Since the special theory of relativity does not take into account the effect of gravitational fields on spacetime, Einstein worked on a more complete theory for about a decade and formulated the "general theory of relativity," which included the effect of gravity as well [2]. In the general theory of relativity, spacetime is no longer Euclidean (flat). The energy in the spacetime produces distortion resulting in curved spacetime. The general theory of relativity can be summarized by Einstein's field equation

$$R_{\mu\nu} - \frac{1}{2} g_{\mu\nu} R = \frac{8\pi G}{c^4} T_{\mu\nu} \qquad (1.3)$$

where $g_{\mu\nu}$ is the metric tensor, $R_{\mu\nu}$ is the Ricci tensor and R the scalar curvature, all of which describe the geometry of the spacetime and $T_{\mu\nu}$ is the energy-momentum tensor that describes the radiation and matter in the spacetime. G is the universal gravitational constant and c is the speed of light [3]. As John Wheeler put it brilliantly, Einstein's general theory of relativity describes the phenomenon where "matter tells spacetime how to curve, and curved spacetime tells matter how to move." [4]

There are a number of physical consequences of the general theory of relativity that were not previously described by Newton's theories of moving bodies and gravitation. Some of the most striking ones are gravitational time dilation and the gravitational redshift, gravitational lensing, effects on the orbit of moving bodies and the existence of gravitational waves [5].

All of these predictions except gravitational waves had been experimentally verified. The fact that the measured perihelion precession of Mercury's orbit could not be explained by Newtonian physics but agreed well with the prediction of the general theory of relativity provided credence to this theory from the very beginning [6].

Time dilation due to gravity has been measured with precision using atomic clocks [7]. One of the most consequential everyday evidence of time dilation is provided by modern-day GPS tracking systems that rely on satellites far from Earth's surface where time runs faster than on Earth. Thus, time dilation effects must be taken into account to give correct position information and thus accurate routes while using GPS systems.

Similarly the prediction that light is redshifted due to gravitational fields has been tested and verified on several occasions [8]. One example is the gravitational redshift of the light coming from Sirius-B, which has been measured at 80.65±0.77 km/sec using the Hubble telescope [9].

The prediction that gravitational fields bend light and other electromagnetic waves was first tested by Eddington in 1919 during a solar eclipse. He showed that light from a distant source was bent by the gravitational field of the Sun. Modern astronomers have measured the gravitational deflection of radio waves by the Sun using very-long-baseline interferometery [10].

1.1.3. Gravitational Waves in General Relativity

Einstein realized that there exists a wave-like solution for his field equation, Eq. 1.3 [5]. If one solves Einstein's field equation, one can completely determine both the gravitational field ($g_{\mu\nu}$) and the motion of the matter in the spacetime described by $R_{\mu\nu}$. In the limit of weak gravitational fields, when the spacetime metric is only

4

slightly deviated from a flat metric, we can write

$$g_{\mu\nu} = \eta_{\mu\nu} + h_{\mu\nu} \tag{1.4}$$

where $\left| h_{\mu\nu} \right| << 1$. Here $\eta_{\mu\nu}$ is the flat Minkowski metric, the same used for special relativity and $h_{\mu\nu}$ is a linear term in the curved spacetime metric due to the gravitational field. This approximation is referred to as *linearized gravity*. Using this approximation Einstein's field equation, in the Lorenz gauge for a trace-reversed metric perturbation $(\tilde{h}_{\mu\nu})$, can be written as

$$\Box \tilde{h}_{\mu\nu} = -16\pi T_{\mu\nu} \tag{1.5}$$

where $\Box$ is the d'Alembert operator. The $h_{\mu\nu}$ in Eq. 1.4 is the metric perturbation and $\tilde{h}_{\mu\nu}$ in Eq. 1.5 is the gravitational field (trace reverse of $h_{\mu\nu}$); their relationship is given by

$$\tilde{h}_{\mu\nu} = h_{\mu\nu} - \frac{1}{2}\eta_{\mu\nu}h^{\alpha}{}_{\alpha} = h_{\mu\nu} - \frac{1}{2}\eta_{\mu\nu}h \tag{1.6}$$

where h is the trace of $h_{\mu\nu}$.

The linearized field equation (Eq. 1.5) very far from the source of the gravitational field, where the energy-momentum tensor is effectively zero, can be written as

$$\Box \tilde{h}_{\mu\nu} = \left(-\frac{1}{c^2}\frac{\partial^2}{\partial t^2} + \nabla^2 \right)\tilde{h}_{\mu\nu} = 0 \tag{1.7}$$

This is a three-dimensional wave equation and the plane wave solution to this equation has the form

$$\tilde{h}_{\mu\nu} = A_{\mu\nu}e^{ik_{\alpha}x^{\alpha}} \tag{1.8}$$

where $A_{\mu\nu}$ is a 4×4 constant symmetric tensor in which information about the amplitude and the polarization of the wave is encoded. Thus, it is also referred to as a polarization tensor. k_α is a wave vector that determines the propagation direction of the wave and its frequency. If we assume that the gravitational waves propagate along the z-axis with frequency ω, then the four-momentum wave vector must have the form:

$$k^\alpha = \left(\frac{\omega}{c}, 0, 0, k\right) \tag{1.9}$$

1.1.4. Polarization of Gravitational Waves

The polarization tensor, in Eq. 1.8 is a 4×4 symmetric tensor and thus should generally have ten independent components. However, the freedom of coordinate transformation such as $x^\mu \to x'^\mu = x^\mu + \varepsilon^\mu(x)$ gives

$$\tilde{h}_{\mu\nu} = h_{\mu\nu} - \partial_\mu \varepsilon_\nu - \partial_\nu \varepsilon_\mu \tag{1.10}$$

and leaves

$$\partial_\nu \tilde{h}_\mu^\nu - \frac{1}{2}\partial_\mu \tilde{h}_\nu^\nu = 0 \tag{1.11}$$

This does not change the physical meaning of the the field equations, but provides a boundary condition such that any four components of $h_{\mu\nu}$ can be set to zero. Using this condition, we can choose to set

$$\tilde{h}_{0i} = 0 \qquad (i = 0, 1, 2, 3) \tag{1.12}$$

and in terms of the polarization tensor $A_{\mu\nu}$, we can write:

$$A_{0i} = 0 \qquad (i = 0, 1, 2, 3) \tag{1.13}$$

6

This reduces the ten independent components to six. However, the requirement that the solution satisfies the Lorentz gauge condition,

$$\frac{\partial \tilde{h}^{\alpha\mu}}{\partial x^\alpha} = 0 \tag{1.14}$$

implies that

$$A_{\mu\nu}k^\mu = 0 \tag{1.15}$$

This can be explicitly written as:

$$A_{11}k^1 + A_{12}k^2 + A_{13}k^3 = 0 \tag{1.16a}$$

$$A_{21}k^1 + A_{22}k^2 + A_{23}k^3 = 0 \tag{1.16b}$$

$$A_{31}k^1 + A_{32}k^2 + A_{33}k^3 = 0 \tag{1.16c}$$

Solving these three equations and using the fact that $k^1 = k^2 = 0$ from Eq. 1.9 we can write:

$$A_{13} = A_{23} = A_{33} = 0 \tag{1.17}$$

Therefore, for the 4×4 symmetric tensor $A_{\mu\nu}$, there are only three surviving independent components, A_{11}, $A_{12} = A_{21}$ and A_{22}. The solution we are seeking is traceless, i.e.

$$\mathrm{Tr}A = A^\mu_\mu = 0$$

This imposes the condition $A_{11} = -A_{22}$. Thus, the polarization tensor defined in Eq. 1.8 ends up with only two independent components and is of the form:

$$A_{\mu\nu} = \begin{bmatrix} 0 & 0 & 0 & 0 \\ 0 & A_{11} & A_{12} & 0 \\ 0 & A_{12} & -A_{11} & 0 \\ 0 & 0 & 0 & 0 \end{bmatrix} \tag{1.18}$$

Considering that we chose a plane wave solution moving in the z direction with frequency ω, we can write, $ik_\alpha x^\alpha = -i(\omega t - kz)$. Thus the general solution of Einstein's linearized equations can be written as:

$$\tilde{h}_{\mu\nu}(t,z) = \begin{bmatrix} 0 & 0 & 0 & 0 \\ 0 & A_{11} & A_{12} & 0 \\ 0 & A_{12} & -A_{11} & 0 \\ 0 & 0 & 0 & 0 \end{bmatrix} e^{i(kz-\omega t)} \tag{1.19}$$

The component of the wave that is proportional to $A_{11} = A_{22}$ is called the plus polarization (denoted by +) and the component proportional to $A_{12} = A_{21}$ is called the cross polarization (denoted by $\times$). In terms of these two polarization the equations above can be written as:

$$\tilde{h}_{\mu\nu}(t,z) = \begin{bmatrix} 0 & 0 & 0 & 0 \\ 0 & A_+ & A_\times & 0 \\ 0 & A_\times & -A_+ & 0 \\ 0 & 0 & 0 & 0 \end{bmatrix} e^{i(kz-\omega t)} \tag{1.20}$$

8
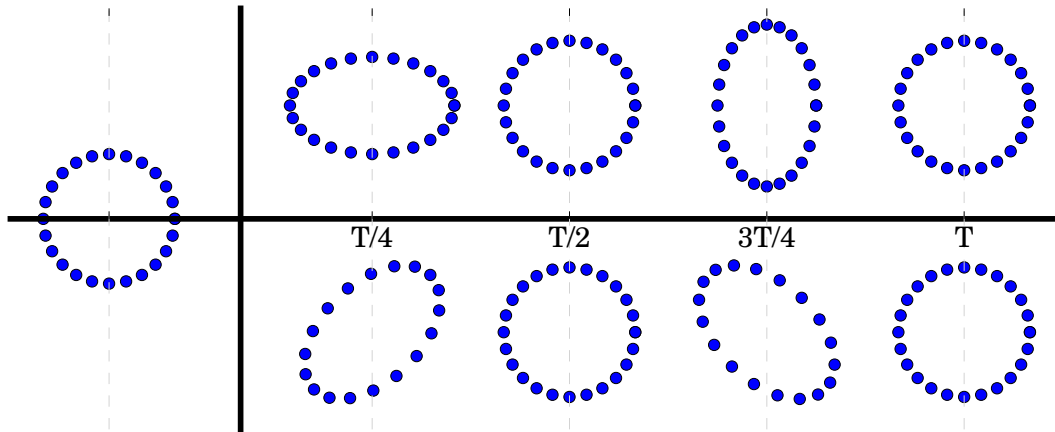
FIGURE 1.1. Gravitational waves traveling perpendicular to the plane containing a ring of masses stretches and contracts them as shown in the figure. The top figure shows the effect of plus polarization and bottom one cross polarization

where A_+ and $A_\times$ denote the amplitude of the plus polarization and cross polarization components respectively.

1.1.5. Effects of Gravitational Waves

We have established that gravitational waves are perturbations of a flat spacetime metric. If we consider a ring of test masses and the gravitational waves propagating perpendicular to the plane containing the ring, the passing gravitational wave changes the proper distance between the test masses in the ring. The waves that have plus polarization cause the two transverse axes to contract and expand alternately as shown in the top panel of Fig. 1.1. However, if the gravitational waves are purely cross-polarized, they will produce expansions and contractions that are rotated by $45°$ as shown in the lower panel of Fig. 1.1. In general, the gravitational waves from any astrophysical source will contain a linear combination of these two polarizations. Thus gravitational waves can be detected by measuring changes in the proper distances between the test masses in such a ring. However, even for the most

energetic astronomical events the relative change in distance, $\Delta L/L$, is on the order of $\approx 10^{-21}$ and thus instruments designed to detect gravitational waves must be sensitive enough to measure these extremely small relative length variations. A more detailed description of how the passing gravitational wave causes contraction and expansion of a set of test masses is given in Chapter 2.

1.1.6. Generation of Gravitational waves

The generation of gravitational waves can be understood using the analogy of the generation of electromagnetic radiation. In the long wavelength approximation, where the wavelength of the radiation is much larger than the size of the source, we can use a multipole expansion to describe the process of gravitational wave generation. As we know, the electric monopole cannot produce electromagnetic radiation due to conservation of charge; conservation of energy forbids gravitational radiation from having a monopole component. Additionally, conservation of momentum prevents gravitational radiation from having a dipole moment. The lowest order and the most significant component of gravitational radiation comes from the quadrupole moment of the mass distribution.

The amplitude of the gravitational wave that arises from this quadrupole moment is directly proportional to the second derivative of the quadruple moment of the mass distribution and is given by [11]

$$h_{\mu\nu} = \frac{2G}{rc^4}\ddot{I}_{\mu\nu}(t - \frac{r}{c}) \qquad (1.21)$$

10

where the quadrapole moment of the mass distribution $I_{\mu\nu}$ is given by

$$I_{\mu\nu} = \int \rho(r,t) \left(x_\mu x_\nu - \frac{1}{3}\delta_{\mu\nu}r^2 \right) d^3r \qquad (1.22)$$

where $\rho(r,t)$ is the time dependent mass distribution of the system.

Using the relations above one can estimate the amplitude of gravitational waves (dimensionless quantity) from a typical binary star system rotating in circular motion around each other using the following relation [11]

$$|h| \approx \frac{r_{s_1} r_{s_2}}{r_0 R} \qquad (1.23)$$

where r_{s_1} and r_{s_2} are the Schwarzschild's radius of the binary components, r_0 is the distance from the center of mass to each binary component and R is the distance from the source at which the gravitational-wave amplitude is measured. If we consider a binary system with each component having a mass of 1.4 times the solar mass (Chandrasekhar limit for a neutron star) and have come fairly close to each other such that $r_0 = 10$ km and are at a distance of 40 Mpc from the Earth, the amplitude of the gravitational waves emitted by the system will be 1.6×10^{-21} when they arrive at a detector on earth [11].

1.2. Gravitational Wave Sources

The direct detection of these gravitational waves remained elusive for a long time because they have amplitude in the order of 10^{-18} m by the time they arrive at detectors on Earth. Producing measurable effects requires astronomical masses moving at relativistic velocities. Compact binary systems composed of black holes and neutron stars are the prime candidates. Depending upon the type of sources and

the type of signals they generate, gravitational-wave sources can be classified into three different types.

1.2.1. Transient Sources

The orbiting pairs of massive and dense objects like white dwarfs, black holes, and neutron stars radiate gravitational waves bringing them ever closer and increasing their rotation speed around each other. They eventually merge together releasing a huge burst of energy in form of gravitational waves. The gravitational waves from some of these sources are and will be visible to LIGO-like detectors at the very end of their life-cycle. The most prominent types of compact binaries are two blacks holes, a black hole and a neutron star, or two neutron stars. These sources are referred to as transient gravitational wave sources. For such a binary system, the time evolution of the system during the inspiral phase where the two components are separate from each other can be determined accurately using weak field approximations of Einstein's field equations. In these approximations, the amplitude of the gravitational waves that arrive at the detector can be written as [12]

$$h(t) = \frac{4}{R} \left(\frac{G\mathcal{M}}{c^2} \right)^{5/3} \left(\frac{\pi f_{gw}(t)}{c} \right)^{2/3} e^{-i\phi_{gw}(t)} \tag{1.24}$$

where $\mathcal{M} = \mu^{3/5} M^{2/5}$ is called the chirp mass, $\mu = m_1 m_2 / M$ is the reduced mass and $M = m_1 + m_2$ is the total mass of the system. $f_{gw}(t)$ and $\phi_{gw}(t)$ are the frequency and the phase of the gravitational wave, respectively. For the simple case of a circular binary system, the frequency and the phase of the system can be computed using

Newtonian approximations and written as [12]

$$f_{gw}(t) = \frac{5}{8\pi} \left(\frac{c^3}{5G\mathcal{M}} \right)^{5/8} \left[\frac{1}{t_c - t} \right]^{3/8} \tag{1.25}$$

$$\phi_{gw}(t) = -2 \left[\frac{c^3(t_c - t)}{5G\mathcal{M}} \right]^{5/8} + \phi_c \tag{1.26}$$

where t_c is the time of merger and ϕ_c is the phase at the time of merger. Note that the amplitude and the frequency of the wave from a binary system increase with time. However, to accurately describe the waveform from a gravitational wave sources when the orbital velocity of the binaries approach significant fraction of the speed of light, Newtonian approximations are not enough and models that include post-Newtonian correction terms are required. A detailed description of the required post-Newtonian corrections can be found in [12]. The first gravitational-wave detection, GW150914, that LIGO made came from such a transient source and is shown Fig. 1.2.

1.2.2. Narrow-Band Sources

Gravitational waves are also produced by a single spinning massive object, like a neutron star, if the mass distribution of the star is not perfectly symmetric about the rotation axis. There are several mechanisms that could lead to the formation of asymmetry in these dense objects. The neutron star may develop deviations from symmetry during its crystallization period. Also, a strong magnetic field in the neutron star, if not aligned with the rotational axis will result in magnetic-pressure-induced distortion. The accretion of matter onto a neutron star from a companion can also produce asymmetry. These asymmetries within the neutron star will result in the emission of gravitational waves [14]. The *continuous* gravitational waves emitted

13
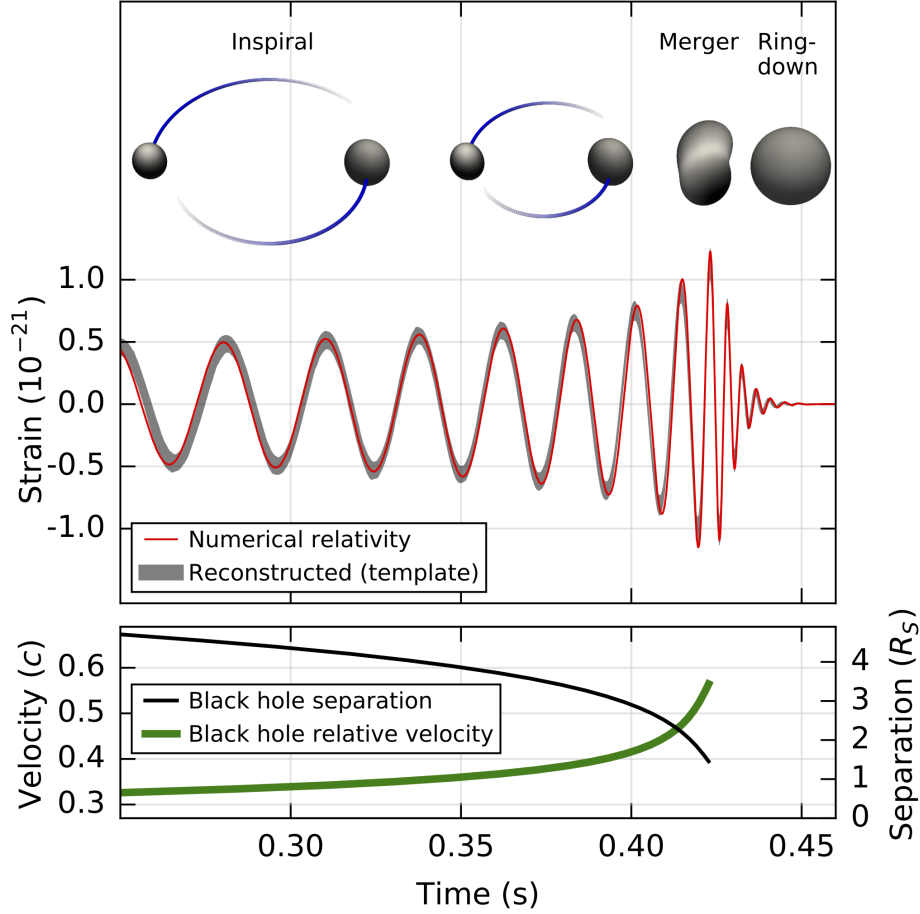
FIGURE 1.2. Top: Estimated gravitational-wave strain amplitude from GW150914 projected onto H1. The inset images show numerical relativity models of the black hole horizons as the black holes coalesce. Bottom: The Keplerian effective black hole separation in units of Schwarzschild radii ($R_S = 2GM/c^2$) and the effective relative velocity given by the post-Newtonian parameter $v/c = (GM\pi f/c^3)^{1/3}$, where f is the gravitational-wave frequency calculated with numerical relativity and M is the total mass [13].

by these sources, with relatively small time varying quadrupolar moment, are narrow-band signals and are typically smaller in amplitude compared with the short-duration signals from the *burst* sources. However, these sources will emit gravitational waves for a long period of time allowing us to integrate the signal over time intervals as long as one year [15]. The amplitude of the gravitational waves from such a system is given by [16]

$$h_0 = \left(\frac{16\pi^2 G}{c^4} \right) \left(\frac{\epsilon I f^2}{R} \right) \tag{1.27}$$

where f is the sum of the rotation frequency of the source and the frequency of precession, I is the moment of inertia with respect to rotation axis, ϵ is the ellipticity of the source and R is the distance from the source to the detector.

1.2.3. Stochastic Background

In addition to the events that produce strong gravitational-wave signals that are detected as individual events, there are numerous weak and unresolved sources. It also includes the gravitational wave radiation of cosmological origin [17]. The integrated effect of these weak sources are referred to as *stochastic gravitational-wave background*. If this background is stronger than the noise in a detector, it can be detected directly. However, the noise level of the ground-based detectors are well above the possible background signals.

But these signals can be discerned from the detector noise by cross-correlating the data streams from two or more detectors. If the detectors instrumental noise is uncorrelated, one can look for the correlated noise created by gravitational wave background by cross-correlation [17]. LIGO searches for these signals using this cross-correlation method [18]

1.3. History of Gravitational-wave Detectors

After decades of debates regarding the existence of gravitational waves, Joseph Weber at the University of Maryland started an effort to detect them in 1960, using resonant bar detectors. These detectors were made of aluminum cylinders, isolated from external vibrations and designed to resonate at certain frequencies. The passing gravitational waves would set these bar in motion and the piezoelectric sensors attached to the cylinders would be able to detect these tiny motions. Although Weber claimed to have detected gravitational waves, it was never independently verified and other people could not make detections using the same technique. Variants of these bar detectors, some spherical in shape and others cooled to sub-kelvin level were designed later [19]. However, due to the lack of success, alternative methods of detection were sought and interferometer-based detectors were conceived.

The idea of an interferometric detector was first proposed by Michael Gertsenshtein and Vladislav Pustovoit in Russia in 1962 [20] and later independently by Rainier Weiss in the United States. Rainier Weiss went on to write a more detailed paper outlining the noise sources these detectors would encounter and a prescription for dealing with those noises [21].

A crucial breakthrough in the detection of gravitational waves came in the form of binary pulsar system called PSR 1913+16 discovered by Hulse and Taylor in 1974. Careful radio observations of the evolution of the system's orbit showed that the energy loss was through the emission of gravitational waves exactly as predicted by general relativity [22]. Gravitational waves was no longer merely theoretical. Though this was only indirect evidence of gravitational waves, it stimulated a dramatic increase in research activities related to gravitational-wave detectors.

Building upon the vision of Rainier Weiss and the research of many others, the Laser Interferometer Gravitational-wave Observatory (LIGO) project started in the early 90's and led to the operation of Initial LIGO (2002-2005) and Enhanced LIGO (2005-2010). Both versions were variations of Michelson interferometers with enhancements to increase their sensitivities. The searches carried out during Initial and Enhanced LIGO did not produce any detection of gravitational waves but provided crucial insight into the upgrades required to make Advanced LIGO possible, resulting in the subsequent direct detection of gravitational waves. Currently there are networks of ground-based interferometric detectors that are operating (LIGO, Virgo, GEO), under construction (Kagra) and planned (LIGO-India).

CHAPTER 2

ADVANCED LIGO DETECTORS AND ACCURATE CALIBRATION

2.1. Gravitational Waves and Laser Interferometers

The LIGO detectors are laser interferometers with light propagating between large suspended mirrors in two perpendicular arms. They are power-recycled Michelson interferometers with Fabry-Perot cavities in each interferometer arm and a signal-recycling cavity at the output of the detector.

The power-recycling, signal-recycling and Fabry-Perot cavities are added to enhance the sensitivity of the detector. However the fundamentals of gravitational wave detection using interferometers can be best understood using the example of a simple Michelson interferometer. In a standard Michelson interferometer, shown schematically in Fig. 2.1, laser light from a source divides at the beam splitter and travels on perpendicular paths along each arm of the interferometer. The light reflects from the mirrors at the ends and returns to the beam splitter before combining to reach the photodetectors. If the two arms of the interferometer are of same length than the two beams will return precisely in phase. If the length of one or both arms changes due to passing gravitational waves, the light returning from the two arms incur a phase shift, $\Delta\phi$, with respect to each other given by

$$\Delta\phi = \frac{2\pi}{\lambda}\Delta x \qquad (2.1)$$

where λ is the wavelength of the interferometer laser beam and Δx is the length change between the two arms. This phase shift is related to the interference produced by the
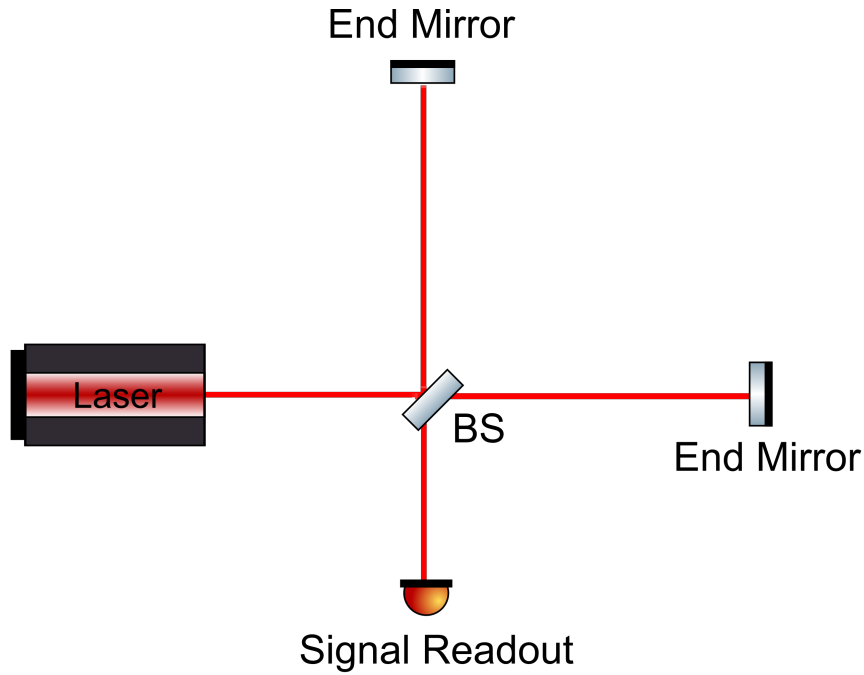
FIGURE 2.1. A simple Michelson interferometer showing laser beam being divided at the beam splitter (BS) and travelling along the two perpendicular paths. The reflected beam combines at the BS and reaches the signal readout photodetector. Template credit: "ComponentLibrary" by A. Franzen.

two beams through $\Delta\phi = \pm 2m\pi$ for constructive interference and $\Delta\phi = (2m+1)\pi$ for destructive interference where, $m = 0, 1, 2...$

By monitoring the change in the interference pattern we can measure the relative change in the lengths of interferometer arms and thus the gravitational wave that caused it [11].

Consider a gravitational wave with a single polarization (+) traveling along the z-axis such that

$$h_+(t) = h_0 \sin(kz - \omega t) \tag{2.2}$$

The Advanced LIGO test masses are suspended, and thus are freely falling along the laser beam direction. The coordinates are labeled by these freely falling masses and

19

for ease of calculation we can assign the beam splitter to be the origin and two arms of the interferometer, each with a length of L_0, to be along the x and y axes with the test masses at $(L_0, 0)$ and $(0, L_0)$. We know, from Eq. 1.1b, that the interval between two events is given by

$$ds^2 = g_{\mu\nu}dx^\mu dx^\nu \tag{2.3a}$$

$$= -c^2 dt^2 + [1 + h_0 \sin(kz - \omega t)]dx^2 + [1 + h_0 \sin(kz - \omega t)]dy^2 + dz^2 \tag{2.3b}$$

For the light traveling along the x arm (assuming $h \ll 1$ such that the higher order terms in h can be ignored) the travel time from the beam splitter to the end and back to the beam splitter is given by

$$\tau_x(t) = \frac{2L_0}{c} + h_0 \sin(kz - wt)\frac{L_0}{c} \tag{2.4}$$

In the absence of gravitational waves, $\tau_x(t) = 2L_0/c$. Thus, the variation in propagation time due to the gravitational wave, $\delta\tau$, can be written as

$$\delta\tau = \frac{\Delta L_0}{c} = h_+(t)\frac{L_0}{c} \tag{2.5}$$

This equation can be rewritten in the following form to show that the gravitational waves produces strain in the interferometer arm

$$\frac{\Delta L_0}{L_0} = h_+(t) \tag{2.6}$$

Furthermore, the light traveling in the y-arm will also incur the same amount of perturbations but in the opposite direction. The light in the two arms of the

20

interferometer that interacted with the gravitational wave while traveling from the beam splitter to the end mirror and returning back to the beamsplitter will incur a travel time difference of

$$\Delta\tau(t) = h_0 \sin(kz - wt)\frac{2L_0}{c} \tag{2.7a}$$

$$= h_+(t)\frac{2L_0}{c} \tag{2.7b}$$

We can rewrite this equation as a phase shift between the lights resonating in two interferometer arms

$$\Delta\phi(t) = h_+(t)\frac{4\pi L_0}{\lambda} \tag{2.8}$$

where λ is the wavelength of the laser light. This shows that the phase shift incurred is directly proportional to the amplitude of the gravitational wave and also the length of the interferometer arms.

2.2. Advanced LIGO Design and Sensitivity

Advanced LIGO detectors are a variants of a Michelson interferometer with enhancements added to increase the sensitivity of the detector. A schematic of the Advanced LIGO interferometer is shown in Fig. 2.2.

The main laser source for the interferometer is a 2-W Nd:YAG non-planar, ring oscillator operating at 1064 nm, followed by two amplification stages with a maximum output power of 200 watts. [23, 24]. The output light passes through an input mode cleaner (IMC) that filters the laser light before it enters the interferometer. The power recycling mirror (PRM), after the IMC, forms a resonant cavity between the laser source and the interferometer to increase the laser power circulating in the interferometer. The arm Fabry-Perot cavities, one in each of the interferometer

21
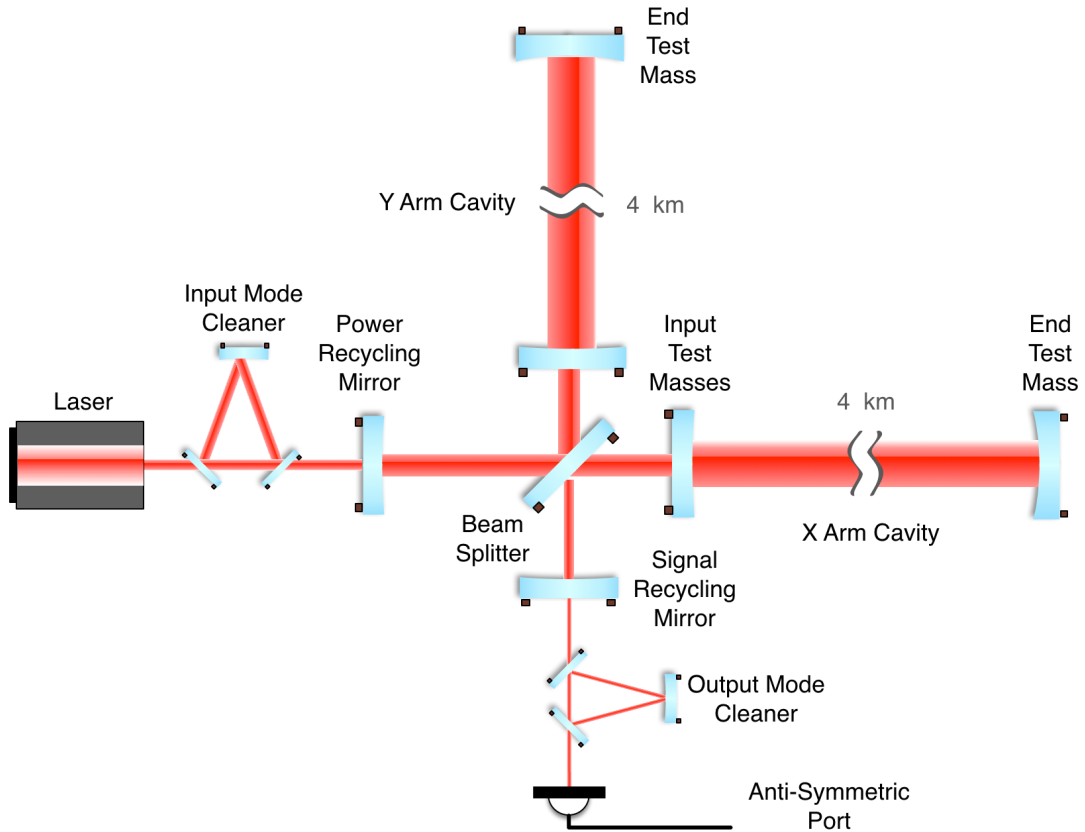
FIGURE 2.2. Advanced LIGO interferometer design showing the Michelson interferometer with power recycling cavity (PRM) at the input end, signal-recycling cavity(SRM) at the signal readout end and Fabry-Perot cavities in each interferometer arm. It also contains input mode cleaner (IMC) and output mode cleaner (OMC) at the input and the output end of the interferometer.

arms, are approximately 4 km long. The circulating light makes ≈ 140 round trips ($finesse = 450$, $Q = 3.6 \times 10^{12}$). This increases the effective length of the arms by a factor of 140 and thus increases the sensitivity of the detector by building up the phase shift produced by any arm length change. This helps to make the Advanced LIGO detectors sensitive to length perturbations, on the order of 10^{-18} m [25].

The signal-recycling mirror (SRM) at the gravitational readout port forms the signal recycling cavity and helps to lower the arm cavity finesse and maintain a broad detector frequency response. This cavity can also be selectively tuned to make

the detector more sensitive at a narrow band frequency with an associated loss of sensitivity at other frequencies. This could principally be used to study signal from specific sources. Finally the interferometer output signal is passed through the Output Mode Cleaner (OMC) that filters unwanted light read by the photodetectors at the anti-symmetric port [26].

The sensitivity of the LIGO detectors is determined by the noise floor of the interferometer as shown in Fig. 2.3. To make a detection, the gravitational wave strain signal needs to be above the noise floor of the detector. At frequencies below 20 Hz the noise floor is dominated by seismic noise, at frequencies between 20-200 Hz, the microscopic fluctuations of the individual atoms in the mirrors and their suspensions dominates the noise floor and at frequencies above 200 Hz it is dominated by the fluctuations of the number of photons in the laser light, referred to as *shot noise* [25].

For Advanced LIGO, the low frequency seismic noise floor has been reduced by active and passive isolation of the test mass from ground motion. The test mass and suspension thermal noise levels have been reduced by using a high purity fused silica for the test mass and by constructing the suspension fibers out of fused silica to create a monolithic suspension for the lower two stages [27]. This has improved the detection bandwidth of the Advanced LIGO detectors at lower frequencies. The high frequency noise level has been reduced by increasing the laser power at the input of the interferometer and adding a signal recycling cavity at the output of the interferometer [26]. The Advanced LIGO detector noise floor for the Hanford and Livingston detectors during the second observing run, along with the detector design noise floor, is shown in Fig. 2.3.
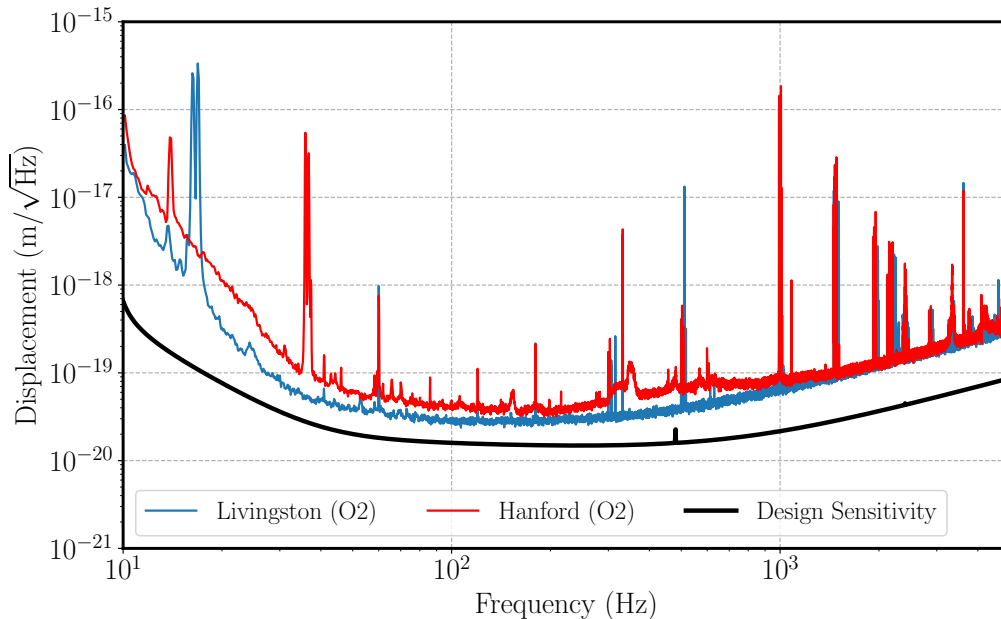
FIGURE 2.3. Representative displacement noise curve for Livingston and Hanford detectors during Advanced LIGO's O2 observing run. Expected noise curve for the Advanced LIGO design sensitivity is also shown.

2.3. Calibration Methods

Calibration of gravitational-wave detectors entails converting the electronic outputs of each detector into detector strain, the measured differential arm length variation divided by the length of the interferometer arm. Over the past twenty years a variety of techniques have been implemented to achieve improvements in the calibration of the LIGO detectors [28, 29, 30].

The calibration of the interferometer output signals is an essential element of data analysis. In order to fully exploit the astrophysical content of the gravitational-wave detections, continuous calibration with accuracy and precision approaching the 1% level is required [31]. This requirement includes amplitude and phase calibration of the Advanced LIGO detectors over the entire range of frequencies to which the Advanced LIGO detectors are sensitive.

Previously, the LIGO project relied on a calibration method that requires extrapolation from test mass displacements that are about 12 orders of magnitude larger than the displacements caused by gravitational waves [28]. This method is referred to as the free-swinging Michelson (FSM) technique. It relies on measurement of Michelson interference fringes when the suspended optics are swinging freely, i.e. not under servo control. It uses the wavelength of the interferometer laser light as a length reference, and calibrates the actuation function of the mirror at the end of the interferometer arms (ETM) via a series of measurements made with both the interferometer and the actuation path electronics in various configurations. As noted earlier, these configurations include the condition where the optics are swinging freely and thus changes in calibration due to the change in optic and control configuration cannot be captured by this method [28].

Another technique is a frequency modulation method which provides a force-free method of calibrating the actuators that are used to drive the test mass (no modulation of the test mass position). This method uses a single-arm configuration and by modulating the frequency of the laser light creates an effective modulation of the arm length given by the dynamic resonance for a Fabry-Perot resonator [32]. Another modulation, close in frequency to the laser frequency modulation, is injected using the test mass actuator that is to be calibrated. By comparing the signals from the two modulations as detected by the single-arm readout sensor, also called the Pound-Drever-Hall (PDH) sensor, the test mass actuator strength is calibrated. Unlike FSM, this technique does not require precise measurement of electronic paths because the actuator electronics are configured to be in run mode during these measurements. But it still will not be able to capture the changes in calibration

due to the change in configuration of the interferometer between the measurement time and the run time [29].

A radiation pressure based technique, referred to as the Photon calibrator (Pcal), has been used in several interferometers and has evolved significantly within LIGO during the past ten years. Pcals were used during initial LIGO to provide an independent check of the calibration. During the Enhanced LIGO era, Pcals were redesigned and installed on one arm of each interferometer with the goals of providing absolute calibration of the interferometer response at one frequency and assessing the long-term trends of actuator coefficients. Analysis of about 400 days of data recorded during Enhanced LIGO's final observing run showed that the long-term stability of the actuation coefficient of the Pcals were at the 1% level for both the H1 and L1 detectors [33]. The redesigned Pcals used a configuration with two diametrically-opposed laser beams in order to minimize the impact of local elastic deformation at the center of the the optic, the region sensed by the interferometer [30]. The Pcal beams are also positioned at the nodal circle of the low order natural vibrational mode of a right, circular cylinders, the *drumhead* mode, to minimize the impact of the elastic deformation of the test mass.

Photon calibrators are being used in Advanced LIGO as the primary calibration tool. Details of the Advanced LIGO Pcals and their use in detector calibration are discussed in Chapter 3 and Chapter 4.

2.4. Calibration Technique

In Advanced LIGO, several feedback control servos are used to keep the interferometer in "resonance" or "lock" to reduce the length variations, ΔL_{free}, due to the unwanted noise or passing gravitational waves. Most of the servo loops have

negligible impact on the gravitational wave strain data for the frequencies between 5 Hz-5 kHz however, the feedback control loop that operates on the differential arm (DARM) length degree of freedom suppresses the gravitational wave strain by significant amount. The suppressed length variation, ΔL_{res}, is determined by the open-loop gain, G, of the control loop and is given by

$$\Delta L_{res} = \frac{\Delta L_{free}}{(1+G)} \tag{2.9}$$

In order to estimate the gravitational wave strain sensed by the interferometer, the effect of DARM feedback control loop needs to be taken into account. As shown in Fig. 2.4, the DARM feedback control loop is characterized by a sensing function C, a set of digital filters D, and an actuation function A. The sensing function C relates the suppressed length variation, ΔL_{res}, to the loop error signal, d_{err}; the digital filters D converts the loop error signal to the control signal d_{ctrl} and the actuation function A relates how the control signal produces the differential displacement of the arm length, ΔL_{ctrl} and is given by the following three equations respectively.

$$\Delta L_{res} = \frac{1}{C} * d_{err} \tag{2.10a}$$

$$d_{ctrl} = D * d_{err} \tag{2.10b}$$

$$\Delta L_{ctrl} = A * d_{ctrl} \tag{2.10c}$$

The strain sensed by the interferometer can be written in terms of the interferometer output signals d_{err} and d_{ctrl} as

$$h = \frac{1}{L} \left(\frac{1}{C} * d_{err} + A * d_{ctrl} \right) \tag{2.11}$$

27
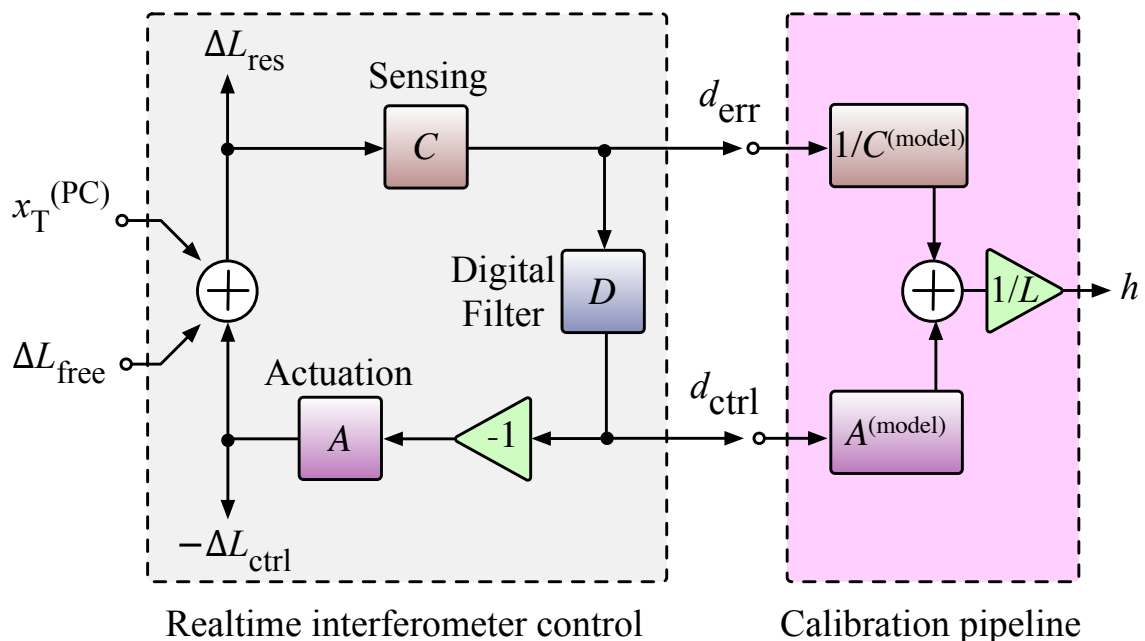
FIGURE 2.4. Left: Block diagram showing different components of Advanced LIGO Differential Arm (DARM) control loop. The external length variation, ΔL_{free} and the Pcal induced length variations, $x_T^{(PC)}$, are suppressed to maintain the interferometer at lock. Right: The two signals from the output of the interferometer, d_{err} and d_{ctrl}, are combined to reconstruct the strain sensed by the interferometer from any external length variation including the gravitational waves [34].

where C and A are the model of the sensing and actuation function respectively and
* denotes convolution in time domain and multiplication in the frequency domain. An accurate characterization and modeling of the sensing and the actuation function enables accurate calibration of the interferometer strain signal [35].

The sensing function C incorporates the laser power fluctuations at the GW port in response to the length variation and also includes the response of the photodiodes and the effects of the analog electronics and the digitization process. The sensing function of the Advanced LIGO interferometers is approximated fairly accurately by a single-pole low-pass filter with a gain (H_c), an additional time delay (τ_C) and a

term that accounts for a detuned signal-recycling cavity [35].

$$C(f,t) = \frac{\kappa_C(t)H_c}{(1+if/f_c)}C_R(f)e^{-2\pi if\tau_C} \times \frac{f^2}{f^2 + f_s^2 - iff_s/Q_s} \qquad (2.12)$$

$\kappa_C(t)$ is a correction factor that accounts for change in H_c over time. f_c is the characteristic cavity pole frequency that determines the attenuation of the interferometer response to length variations at high frequency. $C_R(f)$ describes the effect of electronics and the digital filters which are only relevant at frequencies above 1 kHz. f_s and Q_s parameterizes the detuned signal recycling cavity and are the pole frequency and the quality factor of the optical anti-spring.

The actuation function A describes the response of the Advanced LIGO quadruple suspended pendulum system to the control signal applied to the actuators (applied force). This response includes the mechanical dynamics of the test mass system, actuator strength, the effect of electronics and digital filtering and can be written as

$$A(f,t) = [\kappa_T(t)A_T(f) + \kappa_P(t)A_P(f) + \kappa_U A_U(f)]e^{-2\pi if\tau_A} \qquad (2.13)$$

where A_i denotes the frequency dependent actuation response of the different stages of the cascaded pendulum and κ_i are the correction factor that accounts for change in A_i over time. During O2 observing run, the penultimate and the upper-intermediate mass used a combined time-varying correction factor κ_{PU}. τ_A is the time-delay between digital to analog signal conversion.

A more detailed description of the calibration technique including the description of the sensing and actuation function can be found in [34, 35]. The measurement

technique used to determine the sensing and the actuation function using the Photon calibrator is described in Chapter 4.

2.5. Motivation for Accurate Calibration

The gravitational wave signals detected so far have already been used to test the general theory of relativity in the strong-field regime [36], to understand the physics of evolution of binary mergers [37, 38, 39, 40], to check the validity of the equation of state of the neutron stars [41], to estimate the values of cosmological parameters [42], and to measure the speed of gravitational wave propagation [43]. Accurate calibration of the gravitational-wave strain data has direct implications on the astrophysics we can extract from these detected signals.

2.5.1. Absolute Calibration

The absolute calibration refers to an accurate amplitude calibration of the gravitational-wave signal. There are numerous astrophysical implications of absolute calibration, but the most important identified so far is the measurement of Hubble constant. Independent measurement of the Hubble constant relies on measurement of the luminosity distance, which is directly dependent on the accurate calibration of the amplitude of the signal (see, for example, Eq. 1.24).

The most current measurement of the Hubble constant by the SHoES (Supernovae, HO, for the Equation of State of Dark energy) collaboration using the Hubble Space Telescope, which combines distance measurements from Cepheids and type Ia supernova, is $73.24 \pm 1.74 \, \mathrm{km \, s^{-1} Mpc^{-1}}$, which translates to an uncertainty of $2.4 \, \%$, 1-σ, and includes the systematic uncertainty in the measurement [44]. However, the measurement of the Hubble constant using the Planck satellite's measurement of

the Cosmic Microwave Background (CMB) combined with the effect of gravitational lensing on the CMB, results in a value of 67.8 ± 0.9 km s^{-1} Mpc $^{-1}$ [45]. These two values are in tension with each other at a level of 3σ. The determination of the Hubble constant using the standard siren sources detected by the gravitational wave detectors have the potential to resolve the tension between these two measurement. The signals from the gravitational-wave sources give us an independent direct measurement of the distance to the sources. Both the SHoES and CMB measurements are limited by systematic effects which are not controlled by the experimenters. It is not clear if the tension between the two current measuring techniques is due to lack of understanding of the systematic errors, or due to lack of understanding of fundamental physics. On the other hand, the GW technique is limited by event statistics and eventually by the absolute calibration of the detectors.

The first detection of gravitational-wave signal from two coalescing neutron-stars binary, GW170817, and the subsequent detection of electromagnetic counterparts enabled the measurement of both the distance to the source and the redshift. This allowed us to determine the Hubble constant which was measured to be $70^{+12.0}_{-8.0}$ km s^{-1} Mpc $^{-1}$. This value is consistent with the current measurements from both Planck and SHoES, while being completely independent of them. The 15 % uncertainty in the measurement, which might seem large, is due to the combination of noise in the detectors, calibration uncertainties and the degeneracy between the measurement distance and the inclination angle of the source. However, the uncertainty arising from noise in the detectors can be improved as the number of detections increases. The inclination angle of the binary can be inferred from measurements of both polarizations of the gravitational wave. This will be improved in the future as there will be multiple detectors enabling us to make the polarization measurements
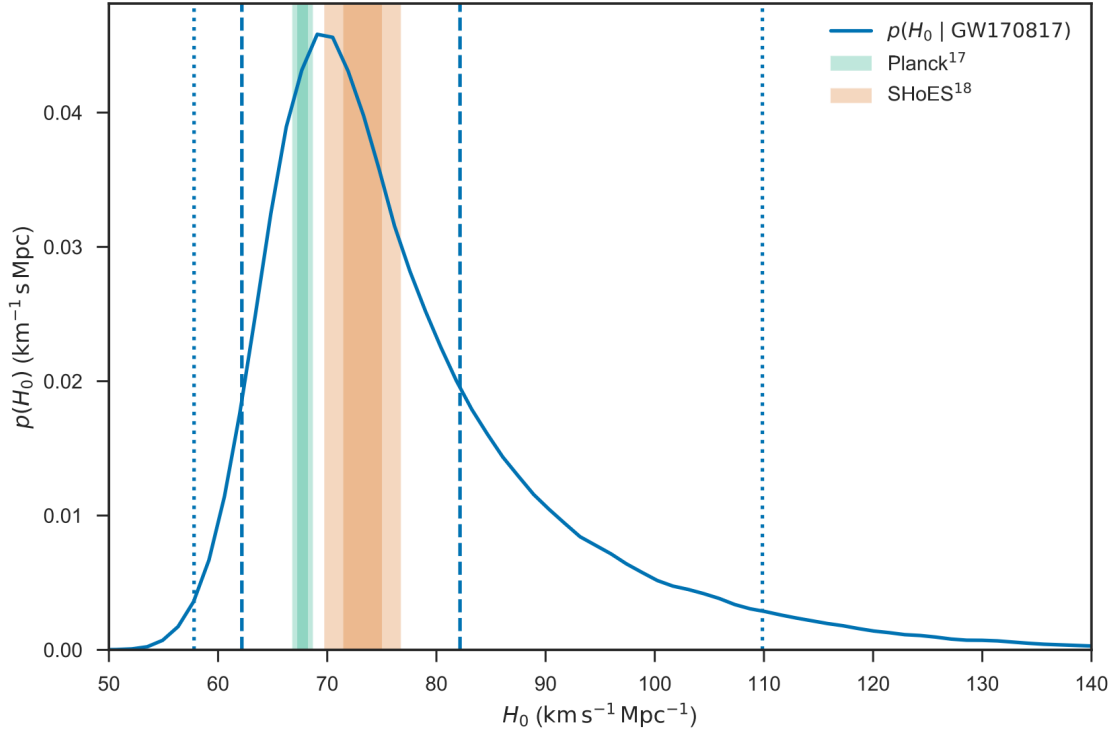
FIGURE 2.5. Posterior probability distribution on the measurement of Hubble constant using the gravitational-wave signal from the merger of binary neutron stars GW170817 [42]

more accurately. The polarization measurement for GW170817 was vastly improved because of the involvement of the Virgo detector compared to previous GW detections, which had large uncertainties in distance and inclination because the two LIGO detectors are co-aligned and thus prevents a more accurate polarization measurement [42]. With enough signals over the course of future runs and the involvement of multiple detectors, eventually the measurement of the Hubble constant will be limited by the calibration of the gravitational-wave data itself.

As outlined in the paper published by Hsin-Yu Chen et.al [46], 4% accuracy in the measurement of the Hubble constant will require about ten events such as GW170817, and to get to the 1% level will require 200 events. With the LIGO detectors operating at design sensitivity and additional detectors joining the network,

updated rate estimates predicts the 1% measurement can be achieved within the next decade. A 1% measurement of the Hubble parameter would resolve the current discrepancy between the measurement derived from the distance ladder and CMB temperature, perhaps pointing to some new understanding of fundamental physics. In addition, a 1% measurement will have a significant impact on the measurement of the dark energy equation of state [47]. Sub-1 % amplitude calibration of the gravitational-wave data will require a significant effort, but is within our reach. Chapter 3 of this thesis will outline and describe a scheme designed to achieve 1 % absolute amplitude calibration accuracy in the foreseeable future.

2.5.2. Relative detector calibration

In order to increase the astrophysical impact of the gravitational wave detections, relative calibration of the detectors is a also crucial. Here relative calibration refers to the calibration accuracy between the detectors that are involved in the search for a particular gravitational wave. If the calibration between the detectors has a relative systematic bias then the estimate of the SNR will also have the same bias resulting in an error in the estimate of sky position of the source. However, achieving accurate relative calibration is easier than getting an absolute calibration. We have designed a scheme in which the calibration tools used in most, if not all, detectors are calibrated against a single standard. As of now, LIGO-Hanford, LIGO-Livingston and Kagra are involved in this scheme and LIGO-India will join it when it goes into operation. We are working on bringing the Virgo calibration into this scheme as well.

2.5.3. Frequency Dependent Calibration

The gravitational waves emitted from compact binary coalescence detected by LIGO are in a wide frequency band, from 5 Hz to 5 kHz. Most of the signals from binary black-hole mergers enter the detector sensitivity at frequencies of a few tens of Hz and sweep all the way to a few hundreds of Hz. However for binary neutron star (BNS), low mass binary-black holes and black hole/neutron star systems the merger frequency may be as high as a few kHz. Additionally the post merger signal of BNS systems could be as high as 4 kHz, depending on which equation of state [EoS] models are valid. So accurate detector calibration over a range of frequencies is important.

Frequency-dependent amplitude errors do not affect parameter estimation for non-spinning sources because the parameters will mostly be determined by the average amplitude. Measurement of the spin of the system will be affected by the modulation of amplitude because the amplitude modulation will mimic the effects of orbital precession [48]. The frequency dependent amplitude calibration error will either overestimate or underestimate the amplitude of the detected signal as it sweeps through the frequency, thus producing an *apparent* amplitude modulation which might mimic the effects of source spin. The frequency-dependent amplitude error could become significantly large at frequencies above 1 kHz when photon calibrators are used to make calibration measurements at these frequencies. Chapter 5 of this thesis will discuss in detail how frequency dependent amplitude errors can be minimized by modeling the effect of bulk elastic deformation and compensating for it.

Frequency-dependent phase errors can mimic the effect of Post-Newtonian (PN) corrections thus biasing the measurement of intrinsic source parameters like masses and spin. However, Vitale et al. show that for Advanced LIGO, where frequency

34

dependent phase error are in the order of only few degrees at its worst, the impact of these error on most signals will be minimal [48].

CHAPTER 3

THE PHOTON CALIBRATOR

The content described in this chapter has been published before in the journal listed below:

S. Karki, D. Tuyenbayev, S. Kandhasamy, et al. "The Advanced LIGO photon calibrators." Review of Scientific Instruments, 87:114503, 2016.

Photon calibrators were first installed on the 10-m prototype detector in Glasgow [49] and later at GEO600 detector in Hannover, Germany [50]. Variations of these instruments have been tested and improved within LIGO over the past 16 years [51, 52]. During this time, the LIGO Pcals evolved from instruments intended as a sanity check on other calibration methods [30] to the primary absolute calibration tools for the Advanced LIGO interferometers. The earlier versions of Pcals used a single-beam configuration. In this configuration, where the force is applied at the center of the optic to minimize unwanted rotation, it deforms the mirror surface in the region sensed by the interferometer, introducing significant calibration errors. This effect, due to so-called *local elastic deformation*, was first predicted by Hild et. al. in 2007 [53]. Goetz et al., in 2009, demonstrated that the errors in calibration due to this effect could be as large as 50 % at few kHz [54]. Subsequent LIGO Pcal systems, beginning with Enhanced LIGO, were designed with two beam configurations with beams displaced from and diametrically opposed about the center of the face of the optic. This ensured that the local elastic deformations due to the Pcal beams were far from the center of the optic and minimized the unwanted rotation by effectively applying the Pcal force at the center of the optic. For Advanced LIGO, Pcals were upgraded with more powerful laser, better optics and electronics and added

36
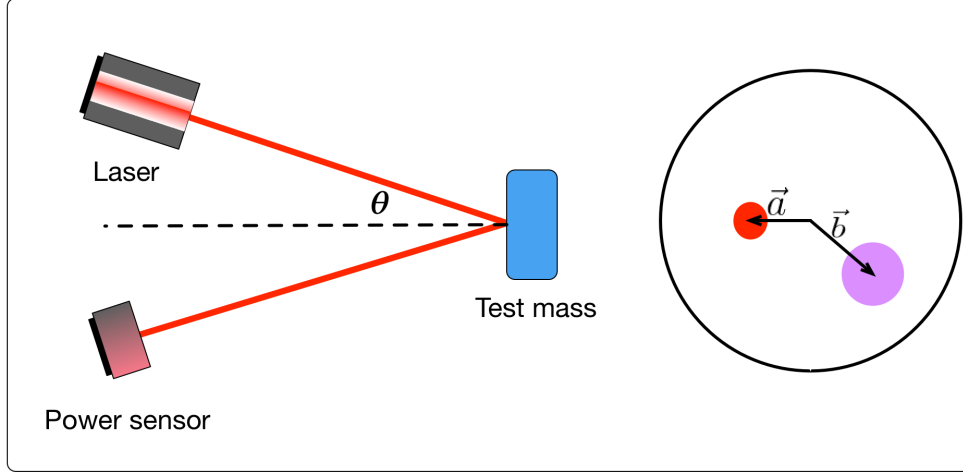
FIGURE 3.1. Schematic diagram showing the working principle of Photon calibrators. The right panel shows the position of Pcal beam and the interferometer beam on the test mass surface.

functionality. The design and performance of the Advanced LIGO Pcals are described in detail in [55] and they are the main subject of this chapter.

3.1. Principle of Operation

Photon Calibrators operate by applying periodic forces on suspended test masses (optics), via photon radiation pressure, using auxiliary power-modulated laser. The suspended test mass to which the force is applied has a pendulum resonance frequency of about 1 Hz. Thus, for frequencies far above the resonance frequency motion of the test mass can be approximated as a free mass. Thus, one can write the relation between the motion of the test mass, $x(t)$, and the force applied to it (F) as

$$F(t) = \frac{dp}{dt} \approx M\ddot{x}(t) \tag{3.1}$$

where p is the momentum of the photons that recoil from the test mass and M is the mass of the test mass.

Considering that the laser power reflected from the test mass is modulated sinusoidally with a modulation amplitude of P_m and angular frequency ω, we can write the power reflected from the test mass as

$$P(t) = P_0 + P_m \sin(\omega t) \tag{3.2}$$

where P_0 is the average power. A single photon carries momentum, $p = h/\lambda$, where h is Planck's constant and λ is the wavelength of the laser light. Since the photons reflect from the mirror surface, the momentum imparted to the optic is twice the normal component of the photon momentum. So for a laser beam that hits the test mass with an angle of incidence θ, the momentum imparted to the test mass is given by $p = 2\cos\theta(h/\lambda)$. If there are n photons per second hitting the test mass then

$$\frac{dp}{dt} = 2\cos\theta \left(\frac{h}{\lambda} \right) n = 2\cos\theta \left(\frac{h\nu}{c} \right) n \tag{3.3}$$

Each photon has energy $E = h\nu$ where ν is the frequency of the continuous wave (CW) laser. For n photons reflecting off the test mass per second, the power on the test mass surface is given by $P = nh\nu$. Using this, we can rewrite equation 3.3 as

$$\frac{dp}{dt} = \frac{2\cos\theta}{c} P \tag{3.4}$$

Using equations 3.1, 3.2 and 3.4, we can write

$$\ddot{x}(t) = \frac{2cos\theta}{Mc} \left(P_0 + P_m sin(\omega t) \right) \tag{3.5}$$

38

Taking the Fourier transform of this expression with respect to time, the amplitude of the motion induced due to the modulated laser power is given by

$$x(\omega) = -\frac{2P_m(\omega)cos\theta}{Mc\omega^2} \tag{3.6}$$

where $P_m(\omega)$ is the amplitude of the power modulation at frequency ω and the negative sign indicates that the test mass motion is 180^0 out of phase with the applied force.

Equation 3.6 is valid for the case where the Pcal's center of force is at the center of the test mass. However, E. Goetz, et al. [54] pointed out that if the Pcal's center of force is offset from the center of the test mass, with the displacement offset given by the vector $\vec{a}$, the test mass will rotate periodically. This induced rotation can be approximated as free rotation for modulation frequencies well above the rotational resonant frequency of about 1 Hz. Thus the equation of motion of the freely rotating test mass can be written as

$$I\ddot{\Omega}(\omega, t) = aF(\omega, t) \tag{3.7}$$

where I is the moment of inertia of the test mass about an axis through the center of the mass and parallel to the face of the test mass, $\ddot{\Omega}$ is the angular acceleration and $F(\omega, t)$ is the modulated Pcal force. For motion at frequencies well above the rotational resonance frequencies of the test mass, the modulated laser power induces rotation about the center of mass with amplitude given by

$$\Omega(\omega) \approx -\frac{2\vec{a}P_m\cos(\theta)}{Ic\omega^2} \tag{3.8}$$

39

For a perfectly centered interferometer beam the interferometer senses a net length change of zero over the entire beam and thus the rotation has no effect. However, if the interferometer beam is offset from the center of the test mass with the displacement, denoted by vector $\vec{b}$, the interferometer senses an effective length change that is given by [54]

$$x_{\text{rot}}(\omega) \approx -\frac{2P_m \cos(\theta) \, (\vec{a} \cdot \vec{b})}{Ic\omega^2} \tag{3.9}$$

Combining Eq. 3.6 and 3.9, we can write the effective length modulation due to the Pcal forces as

$$x_{\text{rigid}}(\omega) = -\frac{2P_m \cos(\theta)}{Mc\omega^2} \left[1 + \frac{M}{I}(\vec{a} \cdot \vec{b}) \right] \tag{3.10}$$

where x_{rigid} indicates that the test mass is assumed to be a rigid body.

Also, as discussed above, the Advanced LIGO Pcal use two beams with approximately equal powers diametrically opposed and displaced from the center of the test mass to avoid local elastic deformation. The location of Pcal center of force, $\vec{a}$, depends on the beam positions and the ratio of the powers in the two Pcal beams. It is given by

$$\vec{a} = \frac{\beta \vec{a_1} + \vec{a_2}}{\beta + 1} \tag{3.11}$$

where $\vec{a}_1$ and $\vec{a}_2$ are the displacement vectors of the two Pcal beams from the center of the test mass face and $\beta = P_1/P_2$ is the ratio of the laser powers in the two beams.

At higher frequencies the test mass motion does not behave as a rigid body. The Pcal forces excite the natural vibrational modes (*normal modes*) of the test mass introducing *bulk elastic deformation* and thus compromising the accuracy of the calibration. The contributions from *bulk elastic deformation* depend on the geometry

of the modes and can be written as a frequency dependent factor given by

$$\mathcal{G}_{(a_i,b)}(\omega) = \left[1 + \frac{\sum_m x_m(\omega)}{x_{\text{rigid}}(\omega)} \right] \tag{3.12}$$

and described in detail in Chapter 5.

Thus, the total displacement due to the Pcal forces sensed by interferometer can be written as

$$x_{\text{tot}}(\omega) = -\frac{2P_m \cos(\theta)}{Mc\omega^2} \left[1 + \frac{M}{I}(\vec{a} \cdot \vec{b}) \right] \mathcal{G}_{(a_i,b)}(\omega) \tag{3.13}$$

where $\mathcal{G}_{(a_i,b)}(\omega)$ is the effective weight due to *bulk elastic deformation*.

3.2. Instrument Description

For the Advanced LIGO detectors, Photon Calibrators have been used as the primary calibration tool. This increases the need for reliability and performance. The Advanced LIGO Pcals have more powerful 2-W lasers, four times the initial LIGO Pcal laser powers, better beam relay optics, and a feedback control loop to generate arbitrary power modulation. Each detector has two of these Pcal systems, one at the end of each arm of the detector. One Pcal system is adequate for the calibration of the detector. The second system is used as a backup in case of failure and for injecting simulated gravitational-wave signals in order to test the accuracy, efficiency and robustness of the detection pipelines [56]. The second Pcal system is also used to generate displacement modulations at higher frequencies, which require significant power (and integration time) to achieve an appreciable signal-to-noise ratio (SNR), in order to check the calibration at frequencies above 1 kHz. These high frequency modulations will be discussed in greater detail in Chapter 5.

A schematic diagram of the Advanced LIGO Pcals is shown in Fig. 3.2. The
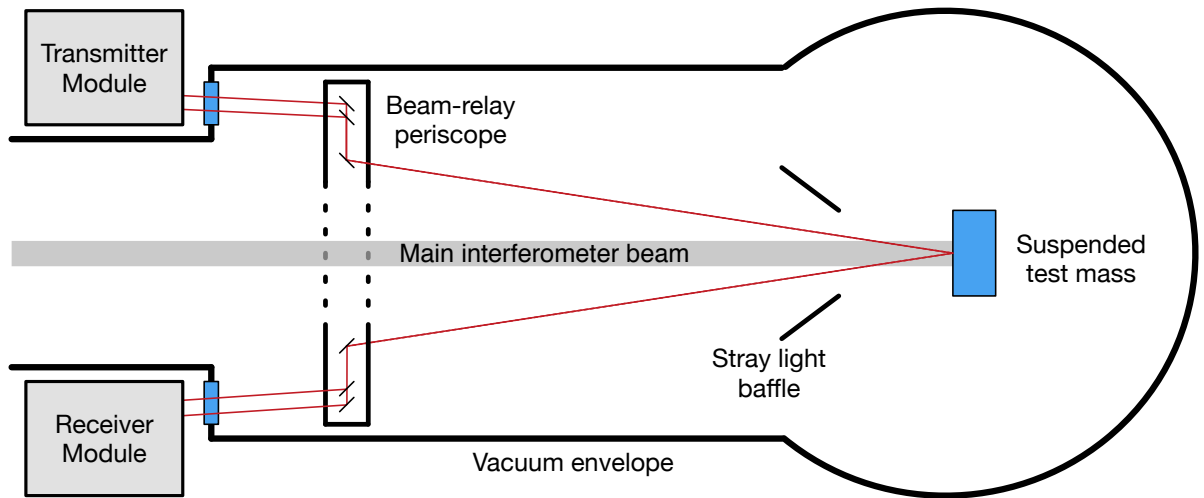
FIGURE 3.2. Schematic diagram of an Advanced LIGO photon calibrator in plan view.

Pcal system consists of out-of-vacuum and in-vacuum components. The transmitter module that houses the laser, signal conditioning optics and power sensors is on a pylon on one side of the beam-tube as shown in Fig. 3.3. The receiver module embedded in the Optical Lever pylon is on the other side of the beam tube and houses relay optics and the receiver module power sensor (RxPD). The two beams from the transmitter module enter the vacuum enclosure through optical-quality, super-polished windows with low-loss ion beam sputtered anti-reflection coatings. Inside the vacuum chamber there is a periscope structure with relay mirrors, that guide the beams to the appropriate positions on the test mass surface. The reflected beams are then directed out of the vacuum by a another set of mirrors on the same periscope structure to a power sensor in the receiver module.
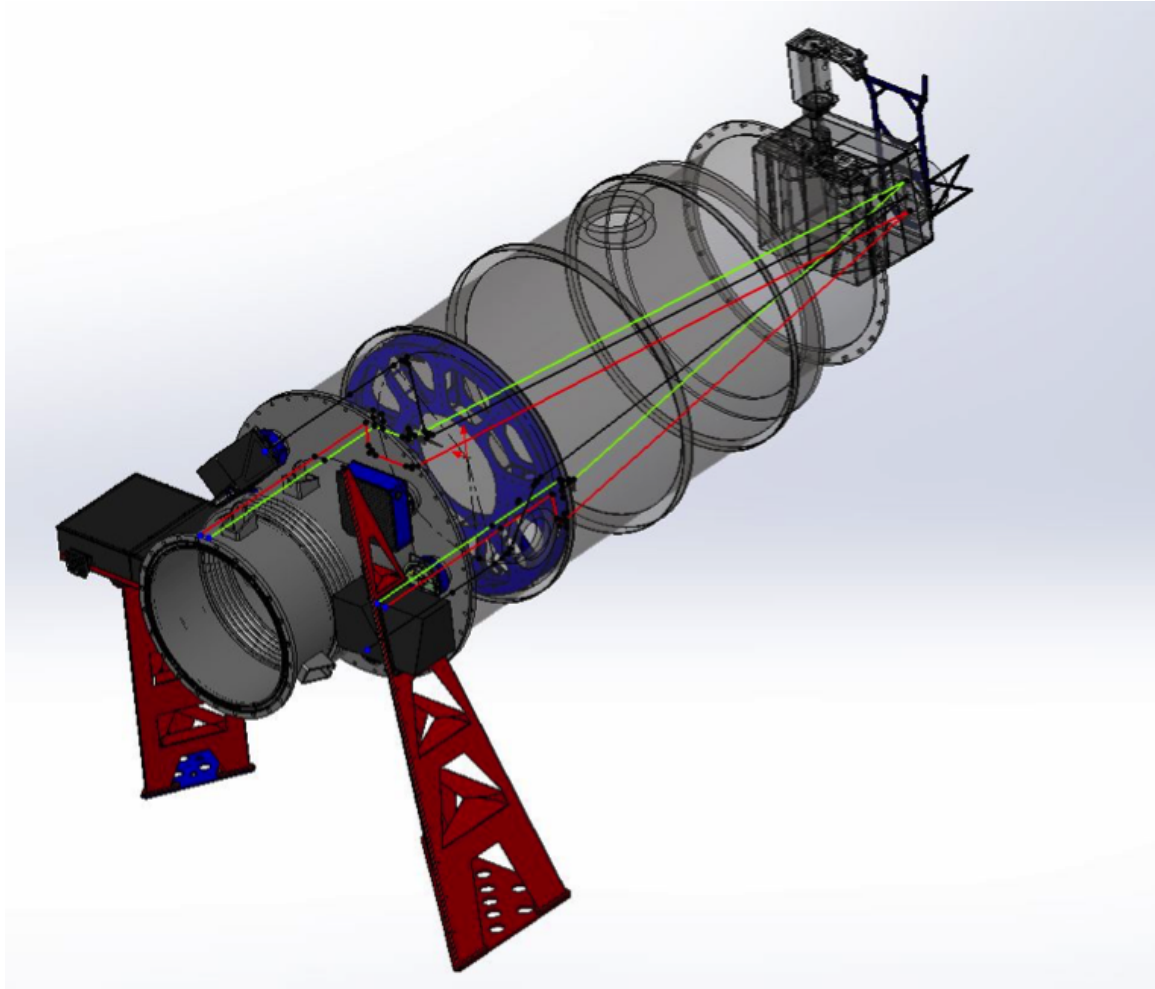
FIGURE 3.3. Bird-eye view of the layout of Advanced LIGO Pcal at the X-End Station. The Pcal transmitter module (square box to the left of the vacuum tube) is mounted in the Pcal pylon, and the Pcal receiver module (on the right side of the vacuum tube) is mounted in the Optical Lever pylon. The Pcal beam path through the periscope and to the ETM and back is shown in red (lower beam) and green (upper beam).
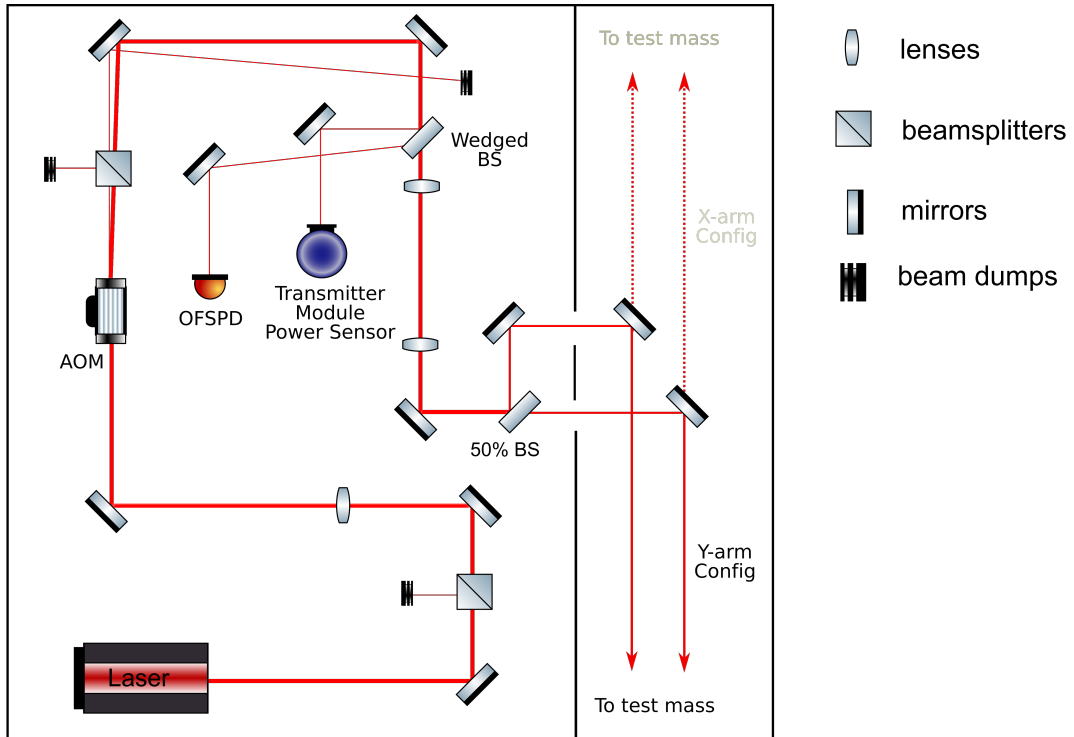
FIGURE 3.4. Schematic diagram of the optical layout of the transmitter module. Template credit: "ComponentLibrary" by A. Franzen.

3.2.1. Transmitter and Receiver Modules

The transmitter module includes a laser, an acousto-optic modulator (AOM), power sensors and optical components necessary to generate the two power-modulated beams. All components are mounted on a 2" thick bread board which in turn is mounted on a pylon, with a flexible bellows connecting its output aperture to the vacuum viewport flange. The optical layout of the transmitter module is shown in Fig. 3.4. The laser inside the module is a 2-watt, continuous-wave, Nd:YLF laser operating at 1047 nm. The laser wavelength is close enough to the 1064 nm wavelength of the interferometer laser to ensure high reflectivity from the test mass mirror coating. The Pcal laser frequency is sufficiently far from that of the interferometer light (approximately 5 THz higher) that the scattered Pcal light does

not compromise interferometer signals that are phase modulated and demodulated at tens of MHz. Furthermore, the relatively large incidence angles and extremely low bidirectional reflectance distribution function (BRDF) of the test mass surface ensure that scattered interferometer light does not impact the accuracy of the Pcal systems. This is confirmed by monitoring the light at the RxPD, which shows no change in measured laser power when the interferometer loses lock or powers up.

The beam originating from the laser is horizontally-polarized using a polarizing beam splitter, then focused into an acousto-optic modulator. The AOM diffracts a fraction of the light in response to a control signal that changes the amplitude of the 80 MHz RF drive signal. The maximum diffraction efficiency is approximately 80 %. The non-diffracted beam is dumped and the first-order diffracted beam is directed through an uncoated wedge beam splitter oriented near Brewster's angle that generates the sample beams used for two photodetectors. The first sample beam is directed into a 2 in. diameter integrating sphere with an InGaAs photodetector. This system monitors the power directed into the vacuum system and is referred to as the transmitter module power sensor (TxPD). The second sample beam is directed to a similar photodetector, but without an integrating sphere. This detector is the in-loop sensor for the *Optical Follower Servo* described in Sec. 3.2.3. The beam transmitted through the wedged beam splitter is collimated using two convex lenses such that it will have a beam waist of approximately 2 mm near the surface of the test mass. The laser beam is divided into two beams of equal power, with the beam-splitting ratio tuned by adjusting the angle of incidence on the beamsplitter. These power-balanced beams enter a separate section of the transmitter housing that is designed to accommodate the power sensor used for laser power calibration and left-
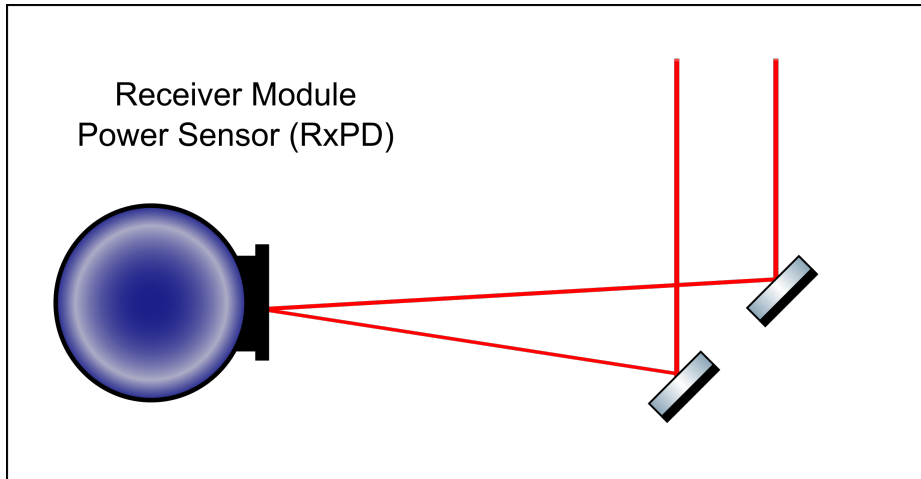
FIGURE 3.5. Schematic diagram of the optical layout of the receiver module. In the receiver module, both Pcal beams reflected from the test mass surface are combined and monitored using a calibrated power sensor. Template credit: "ComponentLibrary" by A. Franzen.

hand (Y-arm) or right-handed (X-arm) configurations for operation on either arm of the interferometer (see Fig 3.4).

The receiver module is shown schematically in Fig. 3.5. The Pcal beams reflected from the test mass are redirected by mirrors mounted to the in-vacuum periscope structure into the receiver module where a pair of mirrors direct both beams to a single receiver module power sensor (RxPD). This sensor is a 4 in. diameter integrating sphere with an InGaAs photodetector.

The ratio of the power measured at the receiver module to that measured at the transmitter module gives the overall optical efficiency. It is typically about 98.5 %. Using this optical efficiency, the power measured with either the transmitter or receiver power sensors can be used to estimate the laser power reflecting from the test mass. Sec. 3.3.1 describes the absolute calibration process for these power sensors.

46
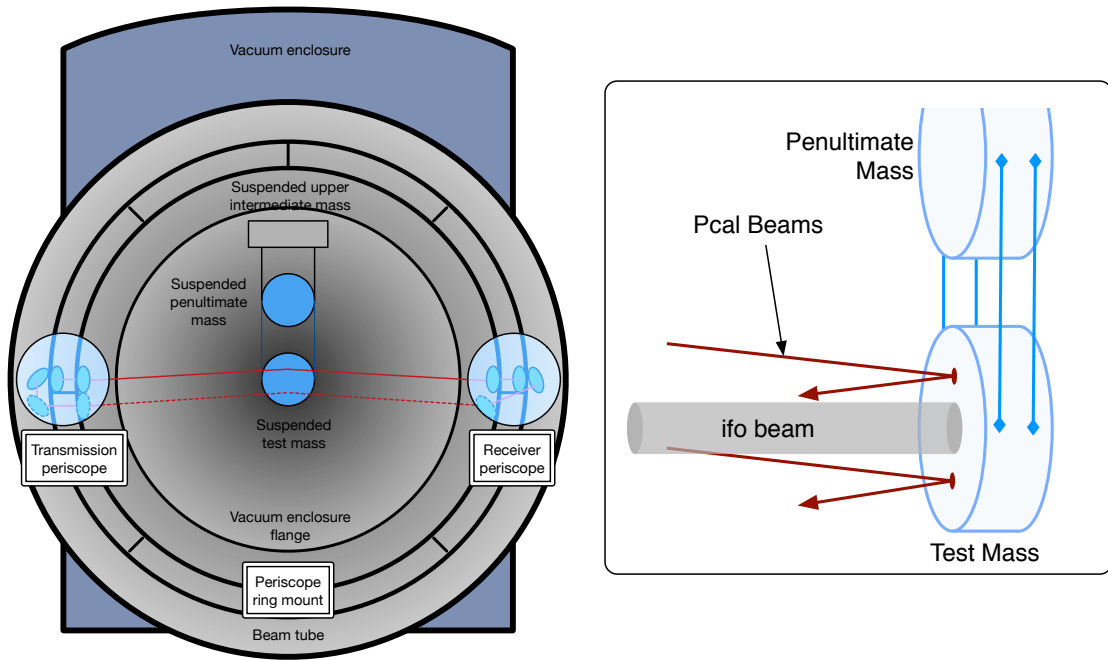
FIGURE 3.6. Schematic diagram showing the Pcal beam path inside the vacuum enclosure. The beams are guided by the mirrors mounted on the periscope on both the transmission and receiver side (left). Schematic diagram of Pcal beams relative to the interferometer beam (right). [Image Credit: Evan Goetz]

3.2.2. Periscope

In Advanced LIGO, folded Arm Cavity Baffles, with apertures just 4 mm in diameter larger than that of the ETM, are located in front of the ETMs. These baffles that are mounted into the persicope structure, preclude directing the Pcal beams directly onto the surfaces of the ETMs. The Advanced LIGO Pcals thus use mirrors attached to the periscope structure to direct the Pcal beam toward the axis of the beam tubes to decrease the angle of incidence on the ETMs and reduce interference with the Arm Cavity Baffles. In addition, for Advanced LIGO, the Pcal beams that reflect from the ETMs are collected by periscope output beam relay optics and directed out of the vacuum system for continuous monitoring. The upper beam

47

is aligned in such a way that it propagates horizontally from transmitter to receiver modules and has two mirrors on each side of the periscope structure. The lower beam, the one that starts farthest from the beam tube manifold axis, is directed down by an input periscope mirror, then propagates horizontally to the ETM and the receiving periscope which directs it back up to the level of the upper beam and out of the vacuum system. The lower beam path has one additional mirror, i.e. three mirrors, on the transmission side. These periscope support structures are held in place by flexures made from maraging steel.

3.2.3. Optical Follower Servo

In order to produce the required calibrated displacement of the test mass, the laser power is modulated such that it produces modulated test mass displacement with a signal-to-noise ratio (SNR) of about 100 in the most sensitive region of the interferometer, near 150 Hz. These modulations run at all times, providing continuous calibration of the detectors. In order to ensure that these calibrated displacements are of a single-tone and at a desired frequencies, a servo is used to improve the purity of the modulated waveform by feedback control. This servo is referred to as the Optical Follower Servo (OFS) [57].

The optical components of the OFS are within the Pcal transmitter module enclosure (see Fig. 3.4) and the electronic components are mounted in the transmitter module pylon. A fraction of the modulated light is sensed by an in-loop photodetector referred to as the optical follower servo PD (OFSPD). The OFSPD signal is subtracted from the reference waveform to form the error signal of the servo. The servo maintains the requested waveform by minimizing the error signal in the loop. The Optical Follower Servo feedback loop block diagram is shown in Fig. 3.7.
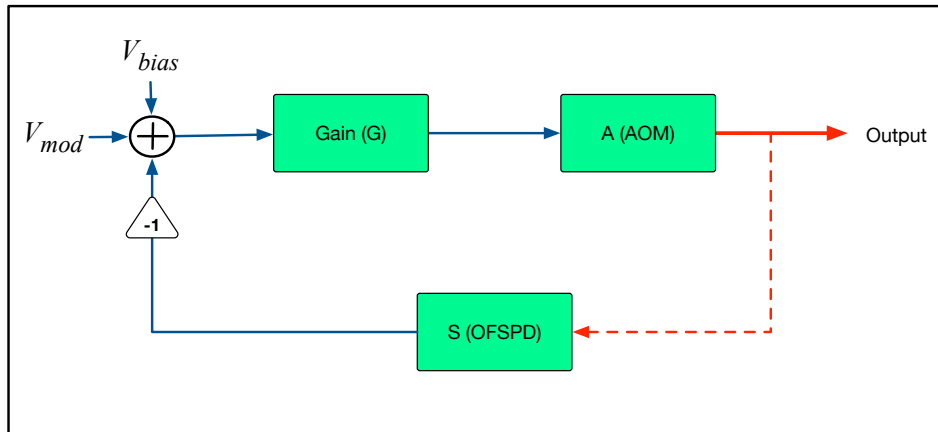
FIGURE 3.7. Optical Follower Servo (OFS) block diagram.

The open- and closed-loop transfer functions of the OFS are shown in Fig. 3.8. The unity gain frequency is approximately 100 kHz, with 62 deg. of phase margin. From DC upto 5 kHz, the discrepancy between the requested and delivered sinusoidal waveforms is less than 0.005 dB (0.06%) and the phase lag is less than 0.6 deg.

This feedback servo also enables operating with larger modulation depths without compromising performance, thus increasing actuation range and more effectively utilizing the available laser power. Fig. 3.9 shows the waveform from the OFS photodetector (red trace) with the servo operating and modulating the available diffracted laser power by 95% peak-to-peak. The black trace (under the red trace) is the requested waveform and the blue trace is the actuation signal, multiplied by a factor of 4 for better visualization, sent to the AOM driver.

Generating high SNR length modulations via the Pcal systems risks introducing unwanted displacement noise into the detectors either through broadband laser noise or through modulation harmonics. Broadband relative laser power noise is inherent to the laser and harmonics are produced by non-linearity in the modulation process.
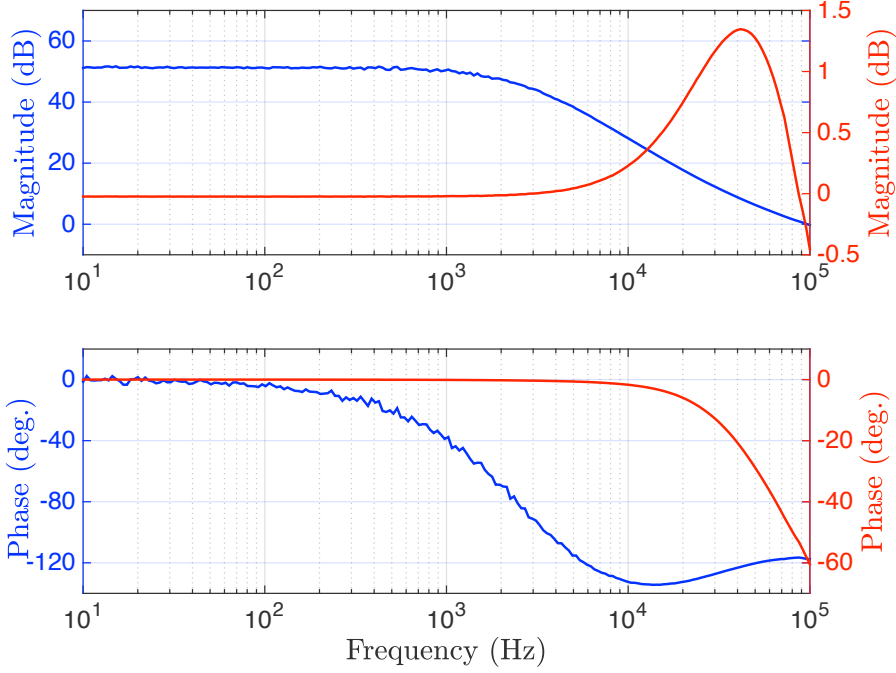
FIGURE 3.8. Measured open-loop (blue) and closed-loop (red) transfer functions of the Optical Follower Servo.

The displacement noise, x_n, caused by the power noise, P_n, is given by

$$x_n = \frac{2 \, P_n \cos(\theta)}{Mc\omega^2} \tag{3.14}$$

The Advanced LIGO requirement is that the noise and the harmonics be a factor of ten below the detector sensitivity [58], that is $x_n \leqslant Lh(f)/10$, where $h(f)$ is the strain sensitivity of the detector and L is the length of the interferometer. The maximum allowed relative power noise (P_n/P_{max}), where P_{max} is the total laser power incident on the test mass, is given by

$$\frac{P_n}{P_{max}} = \frac{Mc\omega^2 Lh(f)}{20P_{max}\cos(\theta)} \tag{3.15}$$

50
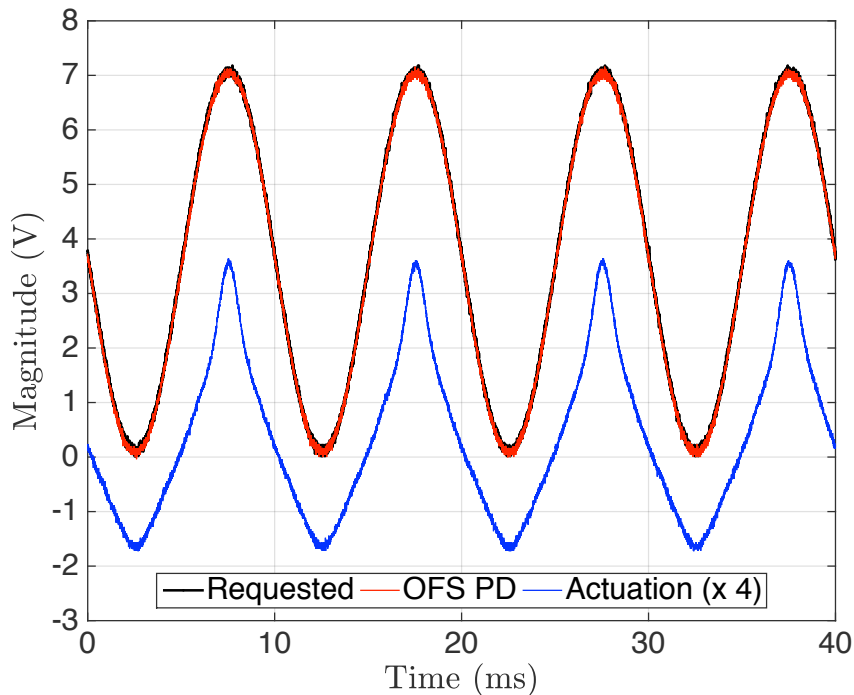
FIGURE 3.9. Optical Follower Servo signals with the loop closed and modulating at 95% of the maximum diffracted laser power. The black trace (under the red trace) is the requested waveform. The red trace is the delivered waveform measured by the OFS photodetector. The blue trace is the actuation signal (x 4) sent to the AOM driver.

Fig. 3.10 shows the free-running (in red) and OFS-suppressed (in blue) relative power noise (RPN) of the Pcal laser light. The suppressed power noise is well below the Advanced LIGO noise requirement, calculated using Eq. 3.15 with the assumption that all the available modulated laser power ($\approx$ 1 W) is incident on the test mass and plotted in black, in the LIGO detection band, from 10 Hz to 5 kHz. Fig. 3.11 shows the suppression of modulation harmonics relative to the carrier as detected by an outside-the-loop transmitted light power sensor, for a requested sinusoidal waveform at 100 Hz and 95% modulation depth. The harmonics are also well below the Advanced LIGO requirement. Furthermore, the modulated power required to achieve an SNR

51
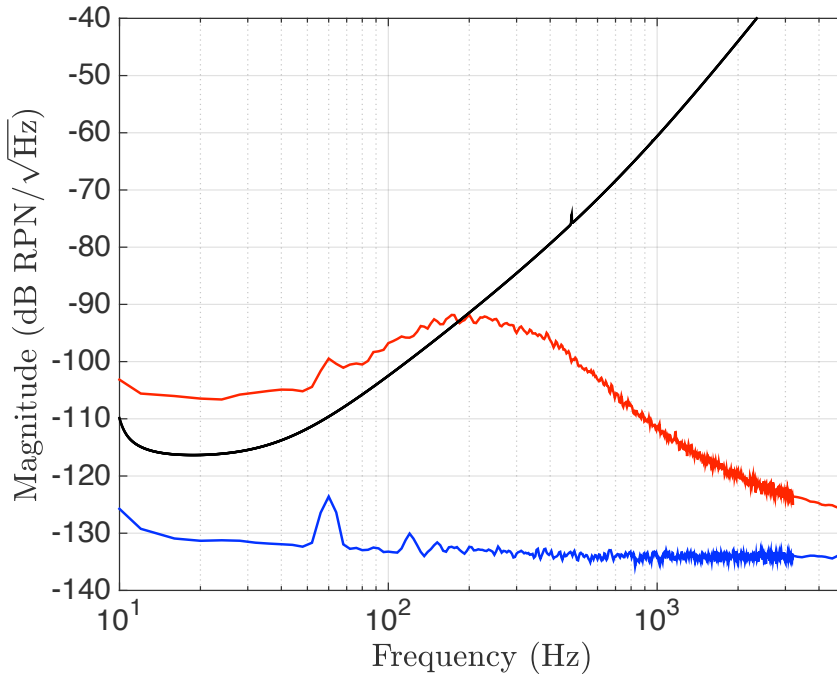
FIGURE 3.10. Free running Relative Power Noise (RPN) of the Pcal laser (in red) and the OFS suppressed RPN (in blue). The suppressed RPN is well below the Advanced LIGO requirement (in black) at frequencies above 10 Hz.

of 100 at 100 Hz is a factor of about 20 less than the maximum modulated power and the sideband amplitudes are lower for lower modulation depths.

The long term stability of the Pcal system can be evaluated by injecting sinusoidal modulations with constant amplitudes into the optical follower servo and measuring the amplitude of the laser power modulation recorded by the transmitter and receiver module power sensors. Since the transmitter module power sensor is insensitive to changes in Pcal performance due to beam misalignments or optical efficiency changes, the receiver module power sensor is used to monitor the state of calibration over time. The amplitude of the receiver module power sensor signal measured over a ninety day interval is plotted in Fig 3.12. The peak-to-peak variation is approximately 0.20 %. Using the RxPD to estimate the induced motion also eliminates errors caused by the induced waveform not exactly matching the requested

52
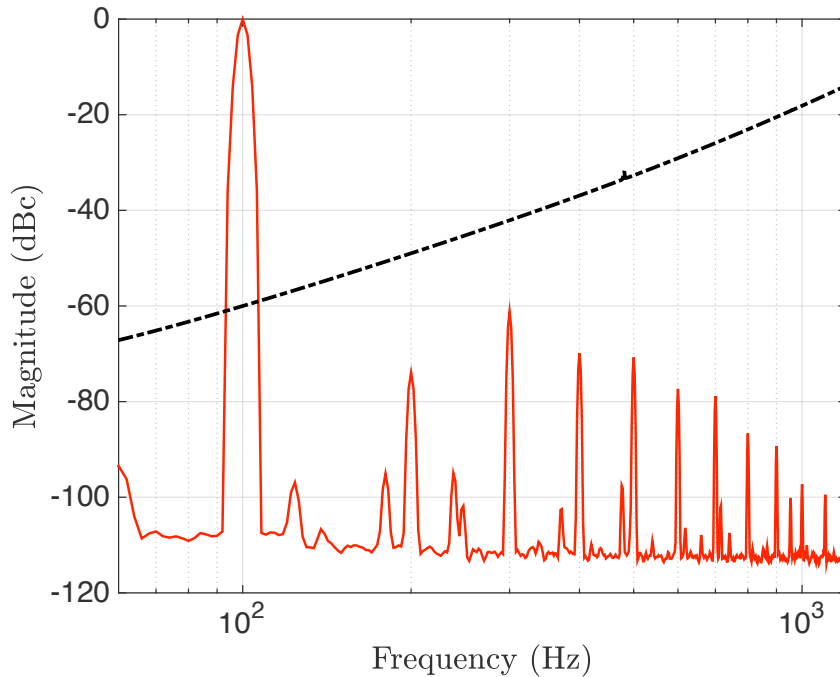
FIGURE 3.11. Suppressed modulation harmonics relative to the carrier. The 100 Hz modulation is at 95 % of the maximum diffracted power. All harmonics are well below the Advanced LIGO noise requirement (in black).

waveform. Thus the data in Fig. 3.12 represents an upper limit of the temporal variations in the Pcal calibration.

3.2.4. Beam Localization System

The accuracy and performance of the Pcal systems depend on the position of the Pcal beams on the test mass surface. There are two important consequences of Pcal beams being offset from the optimal locations: Pcal-induced rotation of the test mass and bulk elastic deformation of the test mass due to the applied calibration forces. [59]. Details of the impact of bulk elastic deformation will be discussed in Chapter 5.

Rotation-induced length variation, due to mis-positioning of the Pcal beams and when the interferometer beam is also off center, is given by the second term in
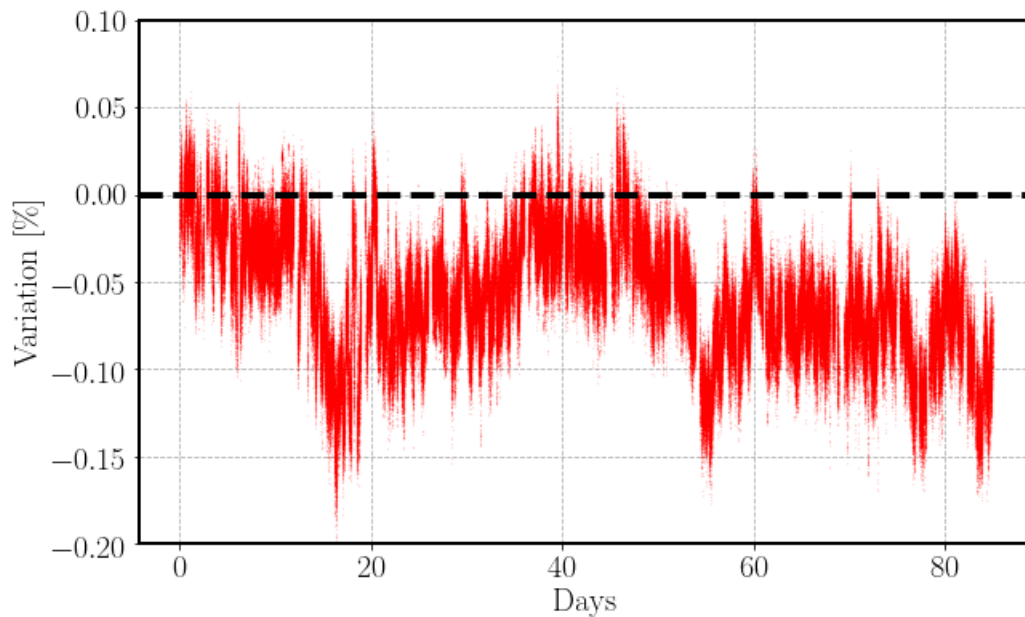
FIGURE 3.12. Trend of the normalized amplitude of the power modulation measured by the power sensor in the receiver module. The amplitudes are calculated using fourier transforms with 10 sec. integration intervals. The variations seen here are correlated with temperature fluctuations in the end-stations.

Eq. 3.10. The rotation can be reduced by optimizing the positions of the Pcal beams. The ideal locations of the Pcal beams and the modeled local deformations caused by them are shown in Fig. 3.13. At the center of the test mass, the effect of this local elastic deformation is minimal because the beams are placed far away from the center of the test mass.

During O1 and O2 a beam localization system consisting of a high-resolution, digital, single lens reflex camera (Nikon D7100; 6000 x 4000 pixels) with the internal infrared filter removed and a telephoto lens remotely controlled via an ethernet interface was used. The camera systems were mounted on separate vacuum view-ports, and used relay mirrors mounted to the same Pcal in-vacuum periscope structure to acquire images of the test mass surfaces such as the one shown in Fig. 3.14.
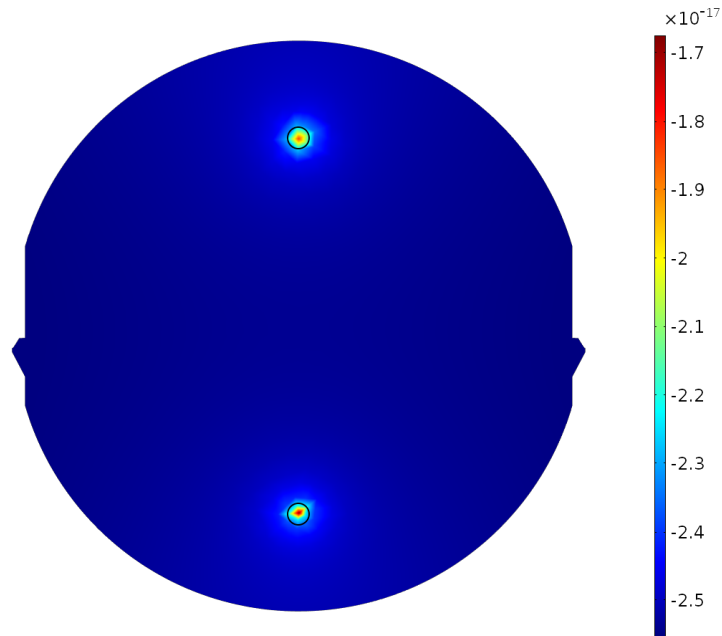
FIGURE 3.13. Plotted here is the surface deformation due to Pcal forces showing the local deformation at the Pcal beam positions. The legend denotes the surface deformation in metres. The two beam configuration is used to avoid the local deformation of the test mass at the center, the region of the test mass surface sensed by the interferometer.

ETM images were analyzed using a MATLAB script to determine the positions of the Pcal beams and to adjust them to their optimal locations, if necessary, using mirror mounts inside the transmitter modules. The algorithm used features of the electrostatic drive (ESD) pattern on the reaction mass surface. The viewing angle, refraction through optics, and the distance between the test mass and reaction mass were used to determine the coordinates of the center of the test mass. This technique enabled estimation of the position of the beams with an uncertainty of about ± 2 mm.

At the end of the second observing run, the beam localization systems were removed because of concerns over noise introduced by the in-vacuum image relay optics that coupled scattered light back into the interferometer. We now rely on measurements made inside the vacuum envelope using a target attached to the
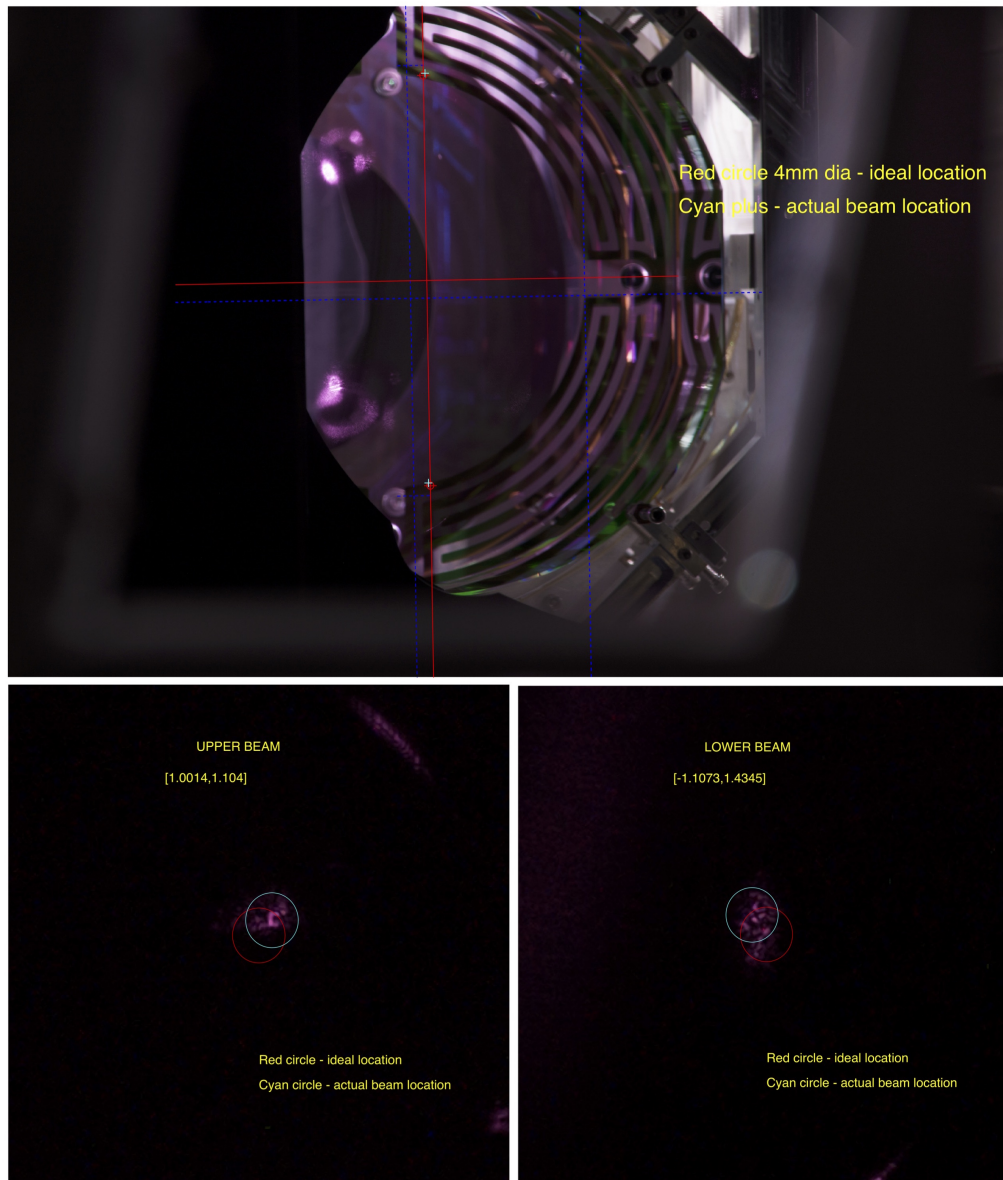
FIGURE 3.14. Image of an end test mass from a Pcal beam localization camera system (top). The left side of the optic is occluded by stray-light baffling. Zoomed versions showing the Pcal beams on the test mass surface (bottom). The beam positions are determined using the electrostatic drive (ESD) pattern on the reaction mass located ≈1 mm behind the test mass.

suspension cage and a fixed-aperture integrating sphere (RxPD) at the receiver side. The target is attached temporarily for beam alignment and later removed. The position of the beams within the aperture of RxPD are used as monitors of the beam positions on the test mass surface. Since the laser travels twice the distance to the test mass before it reaches the RxPD, it will approximately move 0.5 mm on the test mass for every 1 mm movement on the RxPD aperture.

3.3. Absolute Displacement Calibration

The absolute calibration of the relative length response of the interferometer using the Photon calibrator relies on our ability to accurately measure the Pcal laser power, measure the mass of the Advanced LIGO test mass optic in order to determine the force to length transfer function of the quadruple suspension system, and locate the Pcal beam positions to reduce errors due to rotation and elastic deformation of the test mass.

Absolute laser power measurement is realized by calibrating the Pcal power sensors in the transmitter and receiver module of each Pcal system against a standard traceable to SI units and calibrated at the National Institute of Standards and Technology (NIST). This calibration process is described in detail in Sec. 3.3.1. The force to length transfer functions of the Advanced LIGO suspension systems are imported from suspension models. These transfer functions are well approximated by those of a free mass at frequencies above 10 Hz as described in detail in Sec. 3.3.3. The estimate of length variation due to rotation is treated as an additional uncertainty in our estimate of displacement errors as described in Sec. 3.4.5. The impact of the *bulk elastic deformation* of the test mass due to Pcal forces is small at lower frequencies,

but becomes significant at frequencies above a few kHz and is described in greater detail in Chapter 5.

Equation 3.10 can be rewritten in terms of the signals from the Pcal transmitter and receiver module power sensors, TxPD (V_T) and RxPD (V_R), (in volts) [1] to give the induced test mass displacement (in meters) as

$$x_T(f) = V_T \, \Gamma_T \, S(f) \, \mathcal{R}_{(a,b)} \, \mathcal{G}_{(a_i,b)}(f) \tag{3.16a}$$

$$x_R(f) = V_R \, \Gamma_R \, S(f) \, \mathcal{R}_{(a,b)} \, \mathcal{G}_{(a_i,b)}(f) \tag{3.16b}$$

where Γ_T and Γ_R are the force coefficients for the transmitter and receiver module power sensors in newtons per volt (see Eq. 3.30) and $S(f)$ is the force to length transfer function of the Advanced LIGO quadruple suspension system. $\mathcal{R}_{(a,b)}$ is a frequency independent factor that accounts for the apparent length variation caused by rotation of the test mass given by

$$\mathcal{R}_{(a,b)} = \left[1 + \frac{M}{I}(\vec{a} \cdot \vec{b}) \right] \tag{3.17}$$

and $\mathcal{G}_{(a_i,b)}(f)$ is a frequency dependent factor that accounts for the elastic deformation of the test mass due to Pcal forces.

3.3.1. Absolute Laser Power Calibration

Measuring the modulated laser power reflecting from the mirror with the required accuracy is one of the principal challenges for Pcal systems. An integrating sphere based power sensor called the Gold Standard (GS) is maintained in one of the optics

---

[1]The output signals from the digital system are in counts. The counts are converted into volts by using a constant conversion factor of 2^{16} counts for $\pm$ 20 volts or 1638.4 counts per volt. For Advanced LIGO DAQ system these conversions are calibrated within ± 5 counts/V.
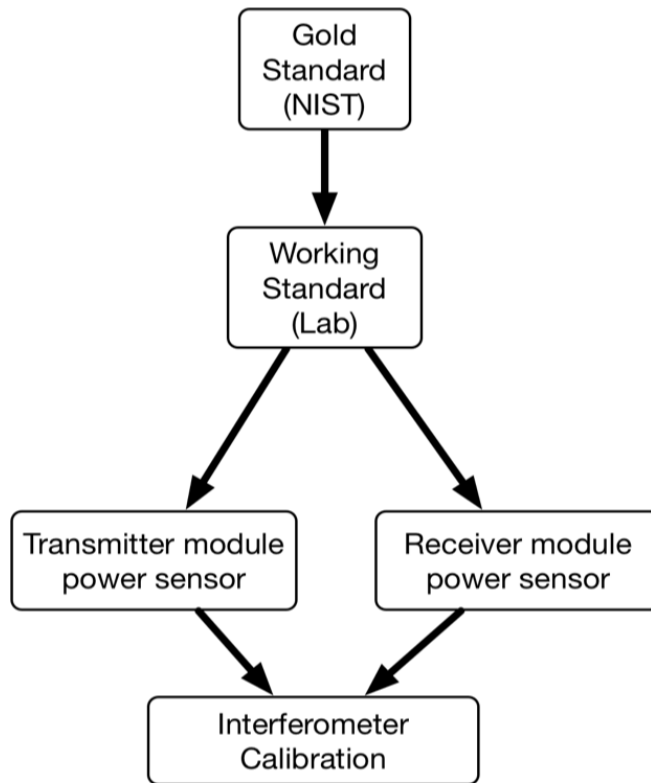
FIGURE 3.15. A block-diagram showing the calibration transfer process

laboratories at the LIGO Hanford Observatory (LHO). The GS is calibrated annually at NIST, which provides traceability to SI units. The calibration of the Gold standard is then transferred to similar power sensors called Working Standards (WS). Each observatory has a Working Standard. The Working Standards are then used to calibrate the power sensors in the Pcal transmitter and receiver modules. This calibration transfer process is shown schematically in Fig. 3.15. The calibrated power sensors in the Pcal modules are then used to estimate the power leaving the transmitter module and the power entering the receiver module using the following

relations:

$$P_T(t) = \frac{V_T}{\rho_T} \qquad (3.18a)$$

$$P_R(t) = \frac{V_R}{\rho_R} \qquad (3.18b)$$

where, ρ_T and ρ_R are the responsivity of the transmitter and receiver module power sensors in units of V/W and V_T and V_R are the voltages reported by these power sensors. The responsivities are determined from three sets of measurements: the Gold Standard calibration at NIST, Gold Standard to Working Standard relative responsivity measurement in the LIGO Hanford Observatory laboratory, and finally the Working Standard to Pcal power sensors relative responsivity measurements at the interferometer end stations. The responsivities, ρ_T and ρ_R, are given by

$$\rho_T = \alpha_{TW} \ \alpha_{WG} \ \rho_G \qquad (3.19a)$$

$$\rho_R = \alpha_{RW} \ \alpha_{WG} \ \rho_G \qquad (3.19b)$$

where ρ_G is the responsivity of the GS, α_{WG} is the responsivity ratio between the GS and the WS and α_{TW} and α_{RW} are the responsivity ratios between the WS and the transmitter module power sensor and the receiver module power sensor respectively. Each step in this power calibration process is described in detail below.

Gold Standard Calibration(ρ_G):

The Gold Standard is a power sensor based on a 4 inch diameter integrating sphere manufactured by Labsphere (Model:3P-040-LPM-SL) with a Spectralon interior, a 1" diameter entrance aperture, and two 1/2"diameter detector apertures.

FIGURE 3.16. Gold Standard setup showing the power sensor mounted on an integrating sphere with Keithley Model 428 programmable current amplifier and Keithely Model 2100 digital multimeter.

An unbiased InGaAs photodetector is mounted to one of the sphere's detector apertures. The GS setup, shown in Fig. 3.16, includes a Keithley Model 428 programmable current amplifier and a Keithley Model 2100 digital multimeter.

This setup is sent to NIST for calibration annually. NIST provides the calibration of the Gold Standard that is traceable to Systéme International (SI) units in volts per watt of laser power. Four such calibration measurement result for the Gold Standard are plotted in Fig. 3.17.

To estimate ρ_G, we calculate the mean of all valid and relevant measurements. Each NIST measurement has a 2-σ (expanded) relative uncertainty of approximately 0.88 % [60]. The source of uncertainties in Gold Standard calibration and how they are incorporated into the overall laser power calibration uncertainty is discussed in Sec. 3.4.
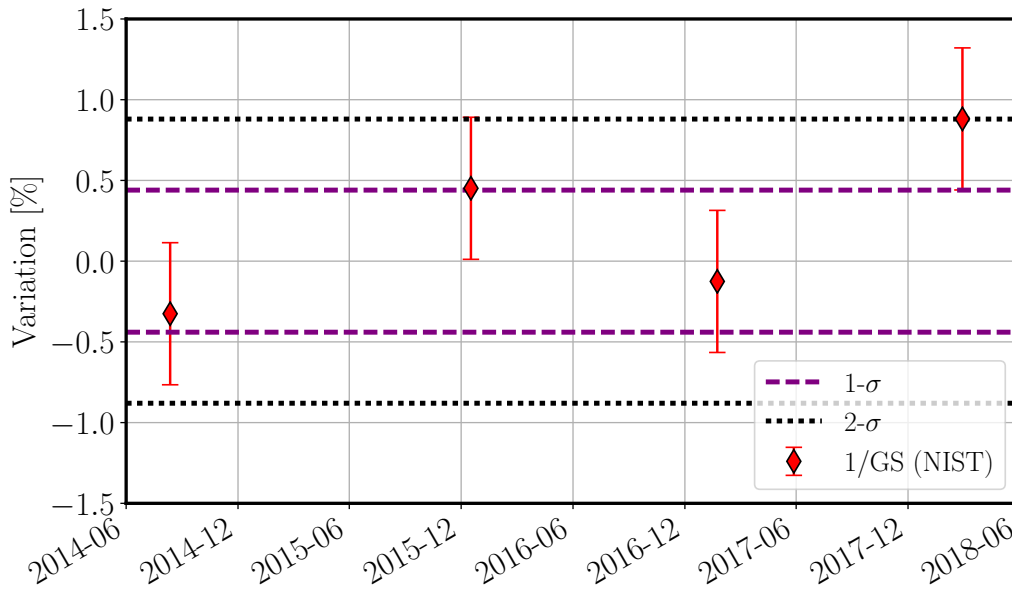
FIGURE 3.17. Variation in the value of Gold Standard responsivity measurement.

<u>Relative responsivity of Gold Standard to Working Standard (α_{WG})</u>

The calibration of the Gold Standard is transferred to similar integrating sphere based power sensors called Working Standards (WS). Each interferometer has its own Working Standard labeled "WSX" where 'X' denotes the first letter of the detector (H for Hanford and L for Livingston). The calibration transfer is made by taking ratio measurements between the Gold Standard and the Working Standard using the setup shown schematically in Fig. 3.18.

For the first measurement the two power sensors are placed in the transmitted and reflected beam paths as shown in Fig.3.18(a) and the time series of the photodetector outputs are recorded. The output of each detector can be written as

$$V_{W_X}(t_{1,i}) = T_{BS}P_l(t_{1,i})\rho_{W_X} \tag{3.20a}$$

62
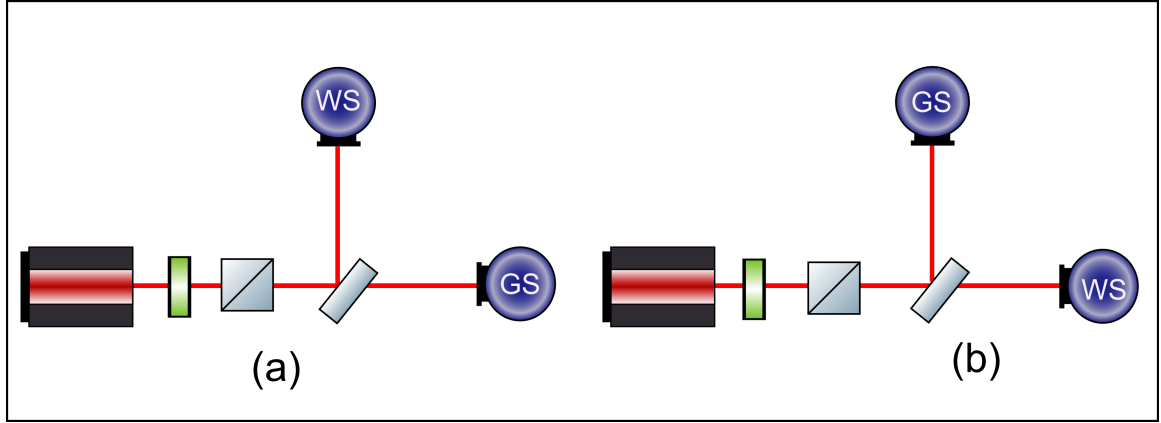
FIGURE 3.18. Schematic of the setup used to transfer the Gold Standard calibration to a Working Standard. The two measurements are made in order to factor out potential variations in the laser power and the beam splitter ratio.

$$V_{\mathrm{G}}(t_{1,i}) = R_{BS}P_l(t_{1,i})\rho_{\mathrm{G}} \tag{3.20b}$$

where, P_l is the output power of the laser source, ρ_G and ρ_{W_X} are the responsivities of the Gold Standard and the Working Standard respectively and T_{BS} and R_{BS} are the transmission and reflection coefficients of the beam splitter.

Then, a second measurement is made after switching the power sensor positions as shown in Fig.3.18(b). The output of each detector can then be written as

$$V_{\mathrm{W}_X}(t_{2,i}) = R_{BS}P_l(t_{2,i})\rho_{\mathrm{W}_X} \tag{3.21a}$$

$$V_{\mathrm{G}}(t_{2,i}) = T_{BS}P_l(t_{2,i})\rho_{\mathrm{G}} \tag{3.21b}$$

We can divide out laser power variations by taking ratios of the simultaneously measured voltages $V_{\mathrm{W}_X}(t,i)$ and $V_{\mathrm{G}}(t,i)$ for each set of measurement.

$$R_1 = \frac{1}{N_1}\sum_{i=1}^{N_1}\frac{V_{\mathrm{W}_X}(t_1,i)}{V_{\mathrm{G}}(t_1,i)} = \frac{T_{BS}\rho_{\mathrm{W}_X}}{R_{BS}\rho_{\mathrm{G}}} \tag{3.22a}$$

$$R_2 = \frac{1}{N_2} \sum_{i=1}^{N_2} \frac{V_{\mathrm{W}_X}(t_2, i)}{V_{\mathrm{G}}(t_2, i)} = \frac{R_{BS}\rho_{\mathrm{W}_X}}{T_{BS}\rho_{\mathrm{G}}} \qquad (3.22\mathrm{b})$$

We can eliminate the beam splitter transmission and reflection coefficients, assuming they have not changed between first and second measurements, by taking the product of R_1 and R_2. The resultant ratio between the Working Standard and Gold Standard responsivities, α_{WG}, can thus be written as

$$\alpha_{WG} = \sqrt{R_1 \, R_2} \equiv \frac{\rho_{W_X}}{\rho_G} \qquad (3.23)$$

One can see that α_{WG}, by definition, is obtained from the measurements alone without explicitly knowing the responsivity of either the Gold Standard or the Working Standard. These responsivity measurements are performed periodically in the optics laboratory at LHO where the Gold Standard is maintained. The Hanford Working Standard (WSH) was measured more frequently, whereas the WSL is shipped from LIGO Livingston Observatory (LLO) at the beginning and the end of each observing run and every 6 months after. Fig 3.19 shows the long-term trends of the responsivity ratios of WSH and WSL to GS respectively. The standard deviation in these measurements over a period of four years is about $\pm$ 0.2 %.

During these measurements, slow variations in the detector signals on the order of 1% peak-peak with periods of tens of seconds are observed as shown in Fig. 3.20. These variations are attributed to laser speckle in the integrating spheres due to the coherent combination of multiple scatterings inside the integrating sphere [61]. The impact of laser speckle is minimized by taking the average of the ratios of the data collected for a period of several minutes.

The Gold Standard and the Working Standards have the same design features and operate on the same principle. If there are common mode changes in the

64
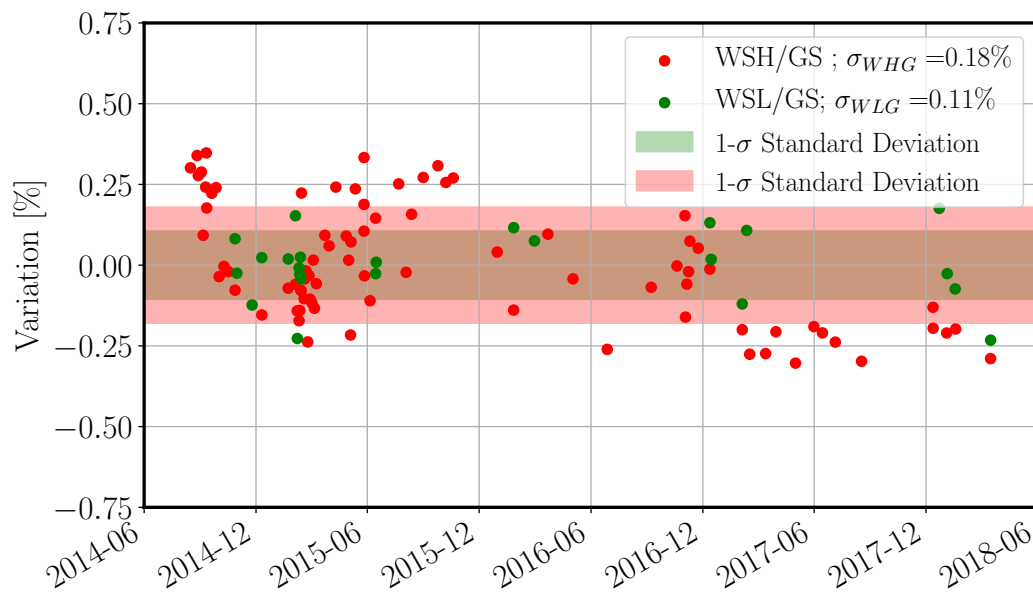
FIGURE 3.19. Working Standard to Gold Standard Ratio trend for the Hanford and Livingston Working Standards.

responsivities, those changes would not be captured in the ratio measurements. In order to have an independent measurement of the stability of these standards, the responsivity of the Gold Standard is also compared to a thermopile-based power sensor referred to as the Checking Standard (CS). The trend of the relative responsivity ratios between the Gold Standard and the Checking Standard (α_{CG}) is plotted in Fig. 3.21. Although these measurements show larger variations compared to the integrating sphere based power sensor measurements; fairly normal distribution of the data indicates that there is no common-mode systematic error in the Gold Standard and the Working Standard calibrations.
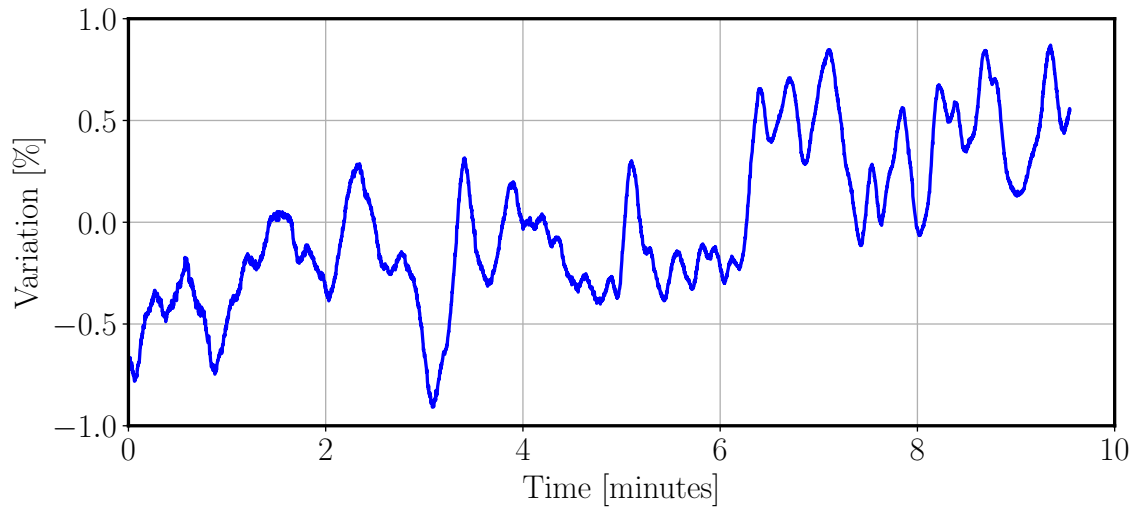
FIGURE 3.20. Output of a calibration standard showing correlated output variations due to laser speckle.

Relative responsivity of Working Standard to end station power sensors (α_{TW} and α_{RW})

The next step is the measurement of the relative responsivities of the Pcal power sensors inside the Pcal transmitter and receiver modules with respect to a Working Standard. This will eventually provide absolute calibration of Pcal power sensors traceable to SI units. A Working Standard is used to measure the power of each of the two Pcal beams before it leaves the transmitter module and after it reflects from the test mass surface and propagates to the receiver module. The appropriate ratios between these measurements give us the relative responsivity between the Working Standard and the Pcal power sensors. Here assumption is made that the wedged beam splitter ratio that samples the light that goes to the transmitter module power sensor and the light that goes towards the vacuum enclosure remains constant. These measurements also give additional information about the laser power ratio between the two Pcal beams and the optical efficiency of the system for each beam. Using a technique similar to that used for relative responsivity of the Gold Standard to

66
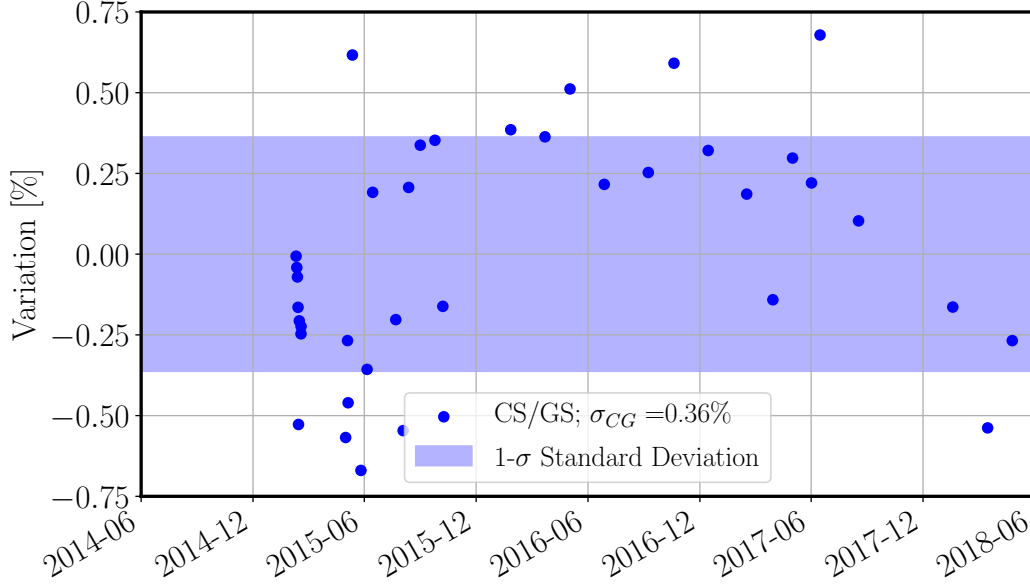
FIGURE 3.21. Checking Standard to Gold Standard responsivity ratio trend.

Working Standard, we can define the relative responsivities of Pcal power sensors and the Working Standard, (α_{TW} and α_{RW}), as

$$\alpha_{TW} = \frac{1}{m_1 + m_2} \equiv \frac{\rho_T}{\rho_{W_X}} \tag{3.24a}$$

$$\alpha_{RW} = \frac{1}{2}\left(\frac{m_5}{m_3} + \frac{m_6}{m_4}\right) \equiv \frac{\rho_R}{\rho_{W_X}} \tag{3.24b}$$

where ρ_T and ρ_R are the responsivity of transmitter module and receiver module power sensor respectively and m_1 to m_6 are the set of six ratio measurements taken between the working Standard and Pcal power sensors. The detailed measurement procedure and the derivation of Eq. 3.24 are described in Appendix A.

Corrections for Optical Efficiencies

During normal operation of a Pcal system, the laser power leaving the transmitter module, $P_T(t)$, is monitored by the transmitter module power sensor and the laser power reflected from the ETM and reaching the receiver module, $P_R(t)$, is measured by the power sensor in the receiver module. The combined power in the beams incident on the ETM surface is between $P_T(t)$ and $P_R(t)$, depending on the optical losses between the transmitter and receiver modules. Assuming that the power loss is evenly distributed between the incident and the reflected beam we can write the power incident on the test mass as the mean of the power measured by the transmitter module power sensor and the receiver module power sensor [2]. Thus, the power incident on the test mass surface, $P_M(t)$ is given by

$$P_M(t) = \frac{1}{2}(P_T(t) + P_R(t)) \tag{3.25}$$

Given that the optical efficiency of the system can be written as, e $= P_R(t)/P_T(t)$, we can write $P_T(t)$ and $P_R(t)$ as

$$P_T(t) = \frac{2}{1+e}P_M(t) \equiv \mathcal{E}_T \ P_M(t) \tag{3.26a}$$

$$P_R(t) = \frac{2e}{1+e}P_M(t) \equiv \mathcal{E}_R \ P_M(t) \tag{3.26b}$$

[2]In vacuum optical efficiency measurements were made after the O2 observing run to improve the uncertainty in power estimated at the test mass and is described in Appendix B

where $\mathcal{E}_T$ and $\mathcal{E}_R$ are correction factors for optical efficiency. Using the definitions of responsivity in Eq. 3.18, we can write the voltages measured by the power sensors as

$$V_{\mathrm{T}}(t) = P_T(t)\rho_{\mathrm{T}} = P_M(t) \underbrace{[\mathcal{E}_T \ \rho_{\mathrm{T}}]}_{\rho'_T} \tag{3.27a}$$

$$V_R(t) = P_R(t)\rho_R = P_M(t) \underbrace{[\mathcal{E}_R \ \rho_R]}_{\rho'_R} \tag{3.27b}$$

Here ρ'_T and ρ'_R are responsivities of the transmitter and receiver module power sensors corrected for optical efficiency. They can be written in an expanded form using Eq. 3.19 as

$$\rho'_T = \mathcal{E}_T \ \alpha_{TW} \ \alpha_{WG} \ \rho_G \tag{3.28a}$$

$$\rho'_R = \mathcal{E}_R \ \alpha_{RW} \ \alpha_{WG} \ \rho_G \tag{3.28b}$$

These responsivity factors provide estimates of the laser power at the test mass surface given by

$$P_M(t) = \frac{V_T(t)}{\rho'_T} = \frac{V_R(t)}{\rho'_R} \tag{3.29}$$

This shows that the estimate of the power measured by either of the Pcal power sensors is theoretically the same, but the RxPD is more reliable and thus the preferred choice because it receives all the power and is thus not subject to changes in the wedged beam splitter (WBS) reflectivity which is the pick-off point for TxPD.

During the upgrade between second and third observing run and when this dissertation was already in its mature state, in-vacuum optical efficiency measurements were made thus providing an ability to determine the amount of power loss between the transmitter side and the receiver side. This led to a new scheme

69

where the overall power loss inside the vacuum enclosure measured during future calibration measurement can be partitioned between the transmitter and receiver module to estimate the actual power at the test mass surface. The procedure, along with the uncertainty calculation associated with this scheme, is described in detail in Appendix B.

3.3.2. Pcal Force Coefficient: Γ_T and Γ_R

The modulated laser power that reflects from the test mass exerts a force that is directly proportional to the laser power. The Pcal force coefficient, Γ, (in N/V) can be defined as

$$\Gamma_T = \frac{2\cos(\theta)}{c}\frac{1}{\rho_{T_e}} \tag{3.30a}$$

$$\Gamma_R = \frac{2\cos(\theta)}{c}\frac{1}{\rho_{R_e}} \tag{3.30b}$$

where ρ'_T and ρ'_R (in watts per volts) are the calibration coefficient of the power sensors such that each power sensors provide an estimate of the laser power reflecting from the surface of the test mass (mirror). The angle of incidence at which the Pcal beams impinge on the test mass surface, θ, determined from design drawings for the interferometer hardware, is 8.75 deg and c is the speed of light, 299792458 m/s.

The calibration, up to this point where we determine the Pcal force coefficient is carried out in steady state (no modulation). The parameters that were used to calculate the LHO Y-end force coefficients that were used during the Advanced LIGO second observing run, and their associated uncertainties, are shown in Table 3.1.

Parameter	Symbol	Value
Angle of incidence	$\cos\theta$	$\cos(8.75) \pm 0.07\%$
GS responsivity	ρ_G	$-1.7001 \pm 0.51\%$
WS/GS responsivity ratio	α_{WG}	$0.9266 \pm 0.003\%$
OE correction factor	$\mathcal{E}_T$ ($\mathcal{E}_R$)	1.0058 (0.9941) $\pm 0.37\%$
WS/Tx,Rx responsivity ratio	α_{TW} (α_{RW})	-2.7447 (-4.0193) $\pm 0.05\%$
Speed of light	c	$299792458 \pm 0.0\%$
Force coefficient	Γ_T (Γ_R)	$1.5160e\text{-}09$ ($1.0475e\text{-}09$) $\pm 0.64\%$

TABLE 3.1. Parameters used to calculate the LHO Y-end Pcal power sensor force coefficient, along with their associated uncertainties, during the O2 observing run.

3.3.3. Suspension Transfer Function: [$\mathbf{S}(f)$]

The suspension transfer function, $S(f)$, describes the dynamics of the test mass in response to applied forces. For a simple pendulum, at frequencies well above the resonance frequency, $S(f)$ can be approximated by free mass motion and is given by $1/M\omega^2$. For Advanced LIGO test mass, which are suspended cascaded quadruple pendulums, this transfer function is valid for frequencies well above the resonance frequencies of ~ 1 Hz. However, for frequencies close to resonance, the transfer function is complicated, as shown in Fig. 3.22. To consider frequencies close to pendulum resonances, we use the measured transfer functions of the Advanced LIGO suspension systems to calibrate the Pcal power sensors. The suspension force-to-displacement transfer function is imported from a MATLAB model and is separated
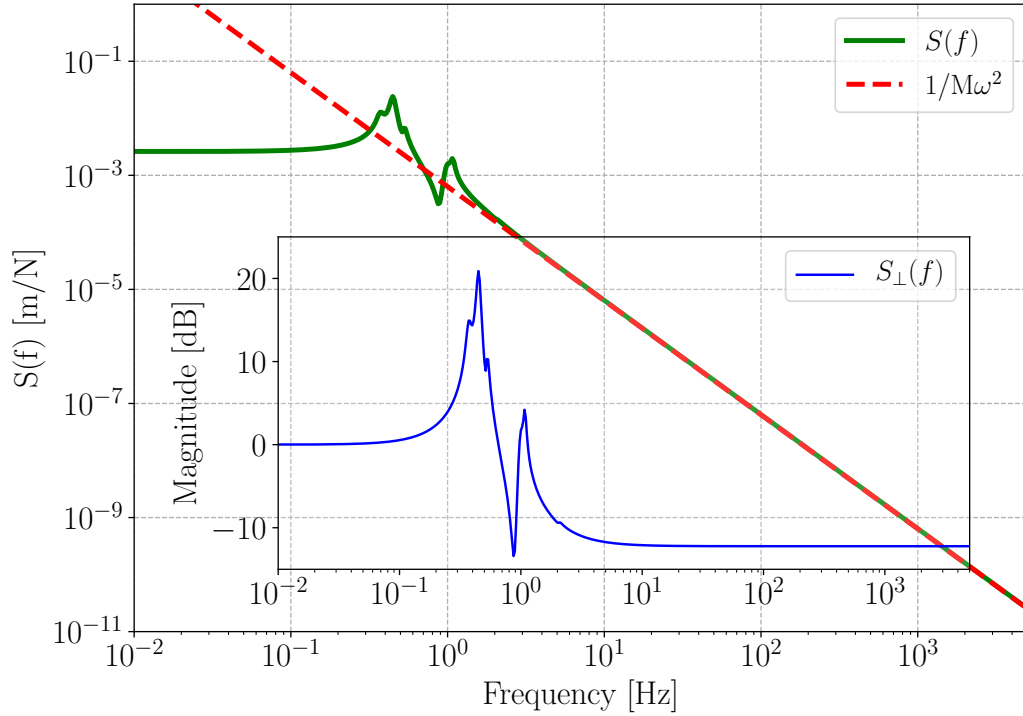
FIGURE 3.22. True force to displacement transfer function of the Advanced LIGO test mass plotted in green and the same transfer function approximated using the free-mass motion plotted in red. Inset: Normalized suspension transfer function, 'susnorm'.

into three components such that:

$$S(f) = k_{\mathrm{mpN}} \times S_{\perp}(f) \times H_{\perp}(f) \tag{3.31}$$

where

- k_{mpN} (m_per_N) is a constant factor that normalizes the suspension transfer function at DC. This is realized by simply picking the value of $S(f)$ at a few mHz.
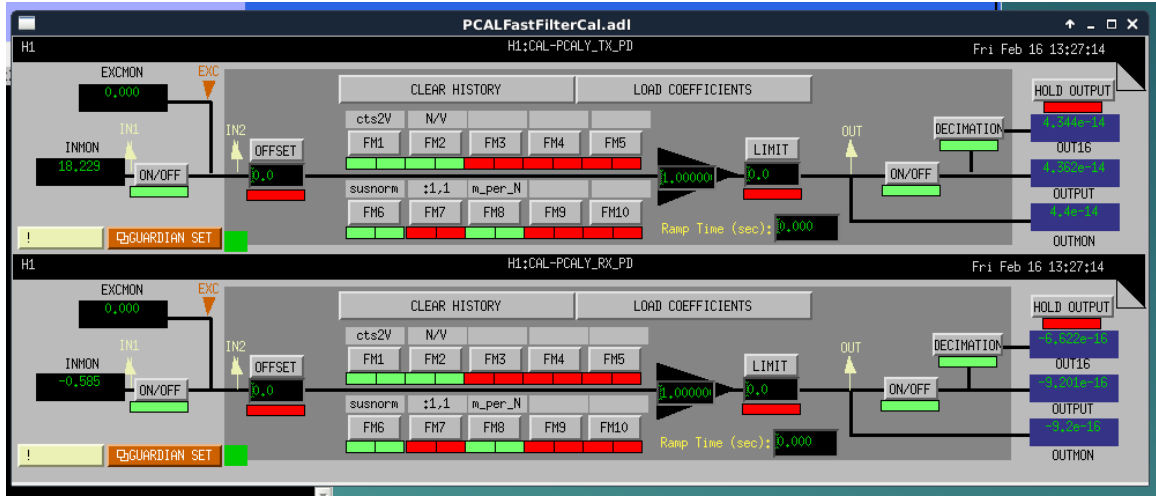
FIGURE 3.23. MEDM screen showing the filter modules for the Photon Calibrator channels from the transmitter and receiver module power sensors. The input to these modules are digitized signals of the power sensors, which are appropriately and the ouput is the

– $S_\perp(f)$ (`susnorm`) is the residual frequency response that has been normalized at DC and divided by two normalized poles at 1 Hz. The resultant transfer function is shown in the inset of Fig. 3.22.

– $H_\perp(f)$ (`:1,1`) is the transfer function of two normalized poles at 1 Hz that compensate the two poles removed from normalized frequency response.

As part of the interferometer calibration process the Pcal force coefficient (N/V) from Sec. 3.3.2 and the three components of the suspension transfer function are entered into a filter bank that conditions the signals from the power sensors at the end station as shown in Fig. 3.23. The second component (the two normalized poles at 1 Hz) from the suspension transfer function is not applied to the signals. This is left out in order to whiten the signals at high frequency and thus reduce the range of the signal that is recorded. To obtain the output signals in units of meters, the Pcal signals recorded in the front-end system are de-whitened by reapplying the two normalized poles at 1 Hz that were omitted to whiten the signals. Additionally, the
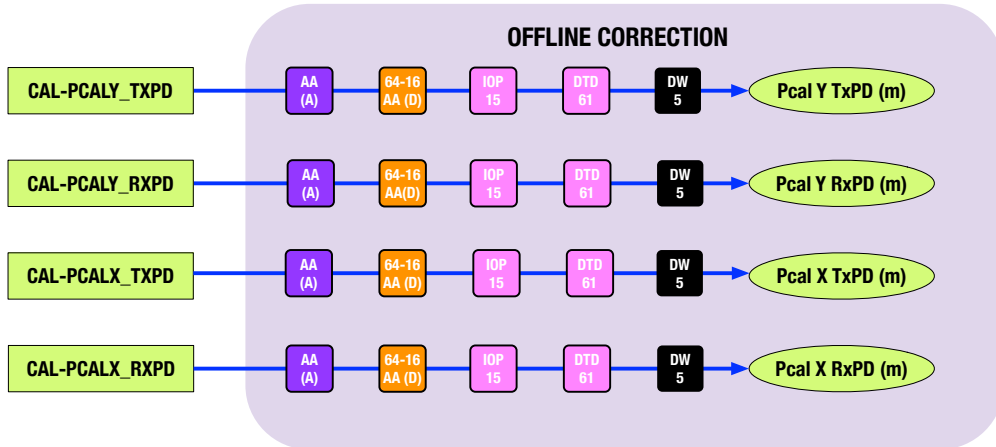
FIGURE 3.24. Block diagram showing the components that must be applied to the Pcal signals recorded in the frames to covert the signals to meters of displacement. The AA(A) and AA(D) are corrections for distortions due to anti-aliasing filters, IOP and DTD are delays in the digital system and the DW5 contains the two normalized poles at 1 Hz.

signals must be corrected for the frequency-dependent distortion created by the anti-aliasing filters and phase delays incurred within LIGO's data acquisition system. This process is shown in the block diagram in Fig. 3.24.

3.4. Uncertainty Analysis

Estimating the uncertainty in displacement calibration using the Photon calibrator relies on uncertainty estimates for the parameters used to calculate displacement from the Pcal power sensor signals. The main sources of uncertainty are described in detail below.

3.4.1. Uncertainty in Gold Standard (GS) Calibration

Each Gold Standard calibration measurement from NIST comes with an approximately 0.44 % 1-σ uncertainty. This uncertainty is determined from various

components of the NIST calibration process and contains two types of uncertainty, Type-A and Type-B [62].

For statistical, type A, uncertainties the components are assumed to be independent and normally distributed and hence the relative standard uncertainty is determined using the following relation [62]:

$$u_{rel,A} = \frac{1}{\bar{x}\sqrt{N}}\sqrt{\frac{1}{N-1}\sum_{i=1}^{N}(x_i - \bar{x})^2} \tag{3.32}$$

where x_i are the individual measurements, $\bar{x}$ is the average of the measured values, and N is the number of measurements.

For type B uncertainties, the uncertainties are assumed to be independent and have a uniform or rectangular distribution such that the probability of a a value being anywhere within the region, $\pm\delta_{rel}$, is equal and the probability of the value being outside this range is zero. The relative standard uncertainty for such components is given by [62]:

$$u_{rel,B} = \frac{\delta_{rel}}{\sqrt{3}} \tag{3.33}$$

The overall uncertainty is estimated by adding the relative uncertainties of all type A and B components in quadrature,

$$u_{rel} = \sqrt{\sum u_{rel,A}^2 + \sum u_{rel,B}^2} \tag{3.34}$$

The $0.44\,\%$ 1-σ uncertainty on each Gold Standard calibration measurement is calculated using Eq. 3.34. Type B components remain unchanged each time the standard is sent for calibration because the uncertainty in these components are drawn from the knowledge of past measurements and device history. Type A components

Date	Calibration factor	Std. Deviation	Uncertainty
	(V/W)	(%)	(1-σ)
2014/08/12	-1.6935	0.13	$\pm$ 0.44
2015/10/17	-1.7067	0.25	$\pm$ 0.43

TABLE 3.2. Gold Standard calibration Measurements carried out at NIST with their associated uncertainty.

will change between measurements but provide a smaller contribution to the overall uncertainty.

At the beginning of the O2 observing run, there were two Gold Standard calibration measurements, shown in Table 3.2, each with approximately 0.44 % relative standard uncertainty. Using these two measurements, relative standard uncertainty on the Gold Standard was estimated using the following relation

$$u_{rel}, \rho_G = \frac{1}{\sqrt{n}} \left(\frac{\sigma_{\rho_G}}{|\rho_G|} \right) \times \mathcal{S}(n) \tag{3.35}$$

where $|\rho_G|$ and σ_{ρ_G} are the weighted mean and the weighted standard deviation of the Gold Standard calibration measurements and $\mathcal{S}(n)$ is the students-T correction for small sample size.

The estimated relative standard uncertainty on ρ_{GS}, using Eq. 3.35, was 0.51 %.

Working Standard	# Meas	$\overline{\alpha}_{W_X G}$	$\sigma_{\alpha_{W_X G}}$	$u_{rel}, \overline{\alpha}_{W_X G}$
WSH	34	0.9268	0.0003	0.0003
WSL	13	0.8896	0.0003	0.0003

TABLE 3.3. Weighted mean values and their associated uncertainties for Hanford and Livingston Working Standard to Gold Standard ratio measurements.

3.4.2. Uncertainty in WS to GS relative responsivity measurements

The mean of the Working Standard to Gold Standard relative responsivity, $\alpha_{W_X G}$, is estimated using the following relation

$$\overline{\alpha}_{W_X G} = \frac{1}{N} \sum \alpha_{W_X G(i)} \qquad (3.36)$$

and the uncertainty on the mean is calculated using

$$u_{rel}, \overline{\alpha}_{W_X G} = \frac{1}{\sqrt{n}} \left(\frac{\sigma_{\alpha_{W_X G}}}{\overline{\alpha}_{W_X G}} \right) \times \mathcal{S}(n) \qquad (3.37)$$

where $\sigma_{\alpha_{W_X G}}$ is the standard deviation of the n ratio measurements. The students-T correction, $\mathcal{S}(n)$, is applied if the sample size is small. The weighted mean values and their associated uncertainties for the Hanford and Livingston Working Standard relative responsivity measurements used during O2 observing run are shown in Table. 3.3.

3.4.3. Uncertainty in End-station ratio measurements

The end station relative responsivity measurements produce two quantities, the optical efficiency of the system (incorporated into $\mathcal{E}_T$ and $\mathcal{E}_R$) and the relative

responsivities of the Pcal power senors with respect to the Working Standard (α_{TW} and α_{RW}). Since, $\mathcal{E}_T$ and α_{TW} ($\mathcal{E}_R$ and α_{RW}) in equation 3.28 come from same set of measurements, for uncertainty calculation we define *effective* relative responsivities, α'_{TW} and α'_{RW}, as follows

$$\alpha'_{TW} = \mathcal{E}_T \cdot \alpha_{TW} \tag{3.38a}$$

$$\alpha'_{RW} = \mathcal{E}_R \cdot \alpha_{RW} \tag{3.38b}$$

Contributions to the uncertainty in the *effective* relative responsivities include three components: statistical uncertainties associated with a single set of measurements, uncertainty associated with the variations in the relative responsivity values between measurements, and the uncertainty associated with optical efficiency.

Statistical uncertainty from a single set of measurements

The statistical uncertainty associated with each end station measurement is mostly attributed to laser speckle. We use six minutes of data acquired at 16 kHz, calculate ratios point-by-point, then calculate the mean and the standard deviation of the ratios for each measurement (m_1 to m_6). The effective relative responsivities, α'_{TW} and α'_{RW}, can be written in terms of these six ratios as

$$\alpha'_{TW} = \frac{2}{(m_1 + m_2 + m_3 + m_4)} \tag{3.39}$$

$$\alpha'_{RW} = \underbrace{\frac{1}{(m_1 + m_2 + m_3 + m_4)}}_{a} \cdot \underbrace{\left[m_5 + \frac{m_3 m_6}{m_4} + \frac{m_4 m_5}{m_3} + m_6 \right]}_{A} = \frac{A}{a} \tag{3.40}$$

Differentiating with respect to each ratio, the relative uncertainty in α'_{TW} and α'_{RW} can be written as

$$\left(u_{rel}, \alpha'_{TW}\right)_{stat} = \frac{\left[(\sigma_{m_1})^2 + (\sigma_{m_2})^2 + (\sigma_{m_3})^2 + (\sigma_{m_4})^2\right]^{\frac{1}{2}}}{|(m_1 + m_2 + m_3 + m_4)|} \tag{3.41}$$

$$\left(u_{rel}, \alpha'_{RW}\right)_{stat} = \frac{1}{A} \cdot \left\{ \left(\frac{A}{a}\right)^2 \sigma_{m_1}^2 + \left(\frac{A}{a}\right)^2 \sigma_{m_2}^2 + \left(1 + \frac{m_4}{m_3}\right)^2 \sigma_{m_5}^2 \cdots \right.$$
$$+ \left(\frac{m_6}{m_4} - \frac{m_4 m_5}{m_3^2} - \frac{A}{a}\right)^2 \sigma_{m_3}^2 + \left(1 + \frac{m_3}{m_4}\right)^2 \sigma_{m_6}^2 \cdots \tag{3.42}$$
$$\left. + \left(\frac{m_5}{m_3} - \frac{m_3 m_6}{m_4^2} - \frac{A}{a}\right)^2 \sigma_{m_4}^2 \right\}^{\frac{1}{2}}$$

where σ_{m_i} are the standard deviations of the corresponding ratios. These statistical uncertainties are plotted as error bars in Fig. 3.25 and are used as weighting factors to estimate the mean and standard uncertainty from multiple measurements.[3]

Standard uncertainty on the mean of multiple measurements

The weighted mean, α'_{TW} and α'_{RW}, of these *effective* relative responsivities is given by:

$$\overline{\alpha'}_{TW(RW)} = \frac{\sum(\alpha'_{TW(RW)}(i) \times w_i)}{\sum w_i} \tag{3.43}$$

where the weighting factor, w_i, is calculated from the statistical variance for each measurement and is given by

$$w_i = \frac{1}{\left(u_{rel}, \alpha'_{TW(RW)}(i)_{stat}\right)^2} \tag{3.44}$$

---

[3]Refer to Appendix A for the derivation of Eqs. 3.39 -3.42.
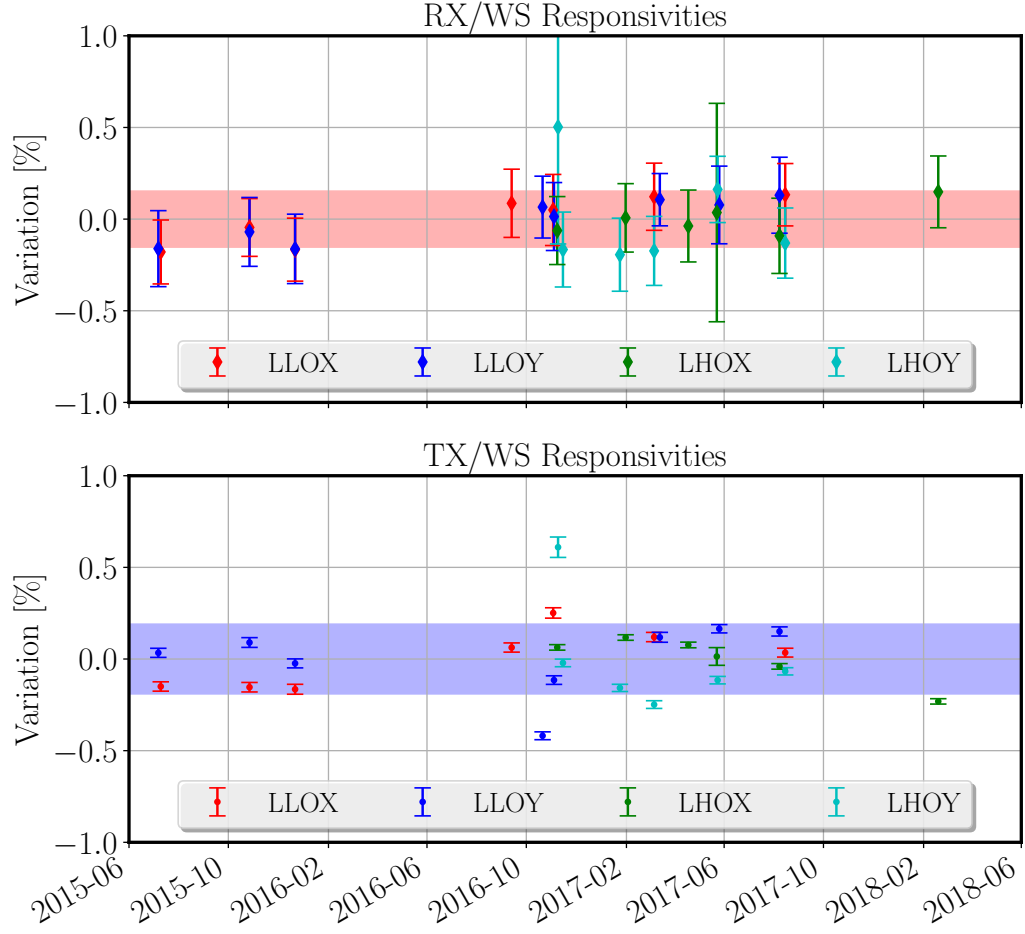
FIGURE 3.25. Ratio of Pcal power sensors (TxPD and RxPD) to Working Standard (WS) measurements from all four end stations over a period of three years. The ± 1-σ standard deviation shown as horizontal bands is 0.15% for α_{RW} and 0.19% for α_{TW}.

The relative standard uncertainty on the mean is given by

$$u_{rel}, \overline{\alpha'}_{TW(RW)} = \frac{1}{\sqrt{n}} \left(\frac{\sigma_{\alpha'_{TW(RW)}}}{\overline{\alpha'}_{TW(RW)}} \right) \times \mathcal{S}(n) \tag{3.45}$$

where $\sigma_{\alpha'_{TW(RW)}}$ is the weighted standard deviation of the *effective* relative responsivity of Pcal power sensors to the Working Standard and $\mathcal{S}(n)$ is the correction prescribed by the Student's t-distribution for small sample numbers.

Parameter	LHO		LLO	
	Y-End[63]	X-End[64]	Y-End[65]	X-End[66]
$\overline{\alpha'}_{TW}$	-2.7608	-3.5467	-2.7392	-2.5902
$\overline{\alpha'}_{RW}$	-3.9957	-4.4511	-4.1603	-4.0881

TABLE 3.4. *Effective* relative responsivities of Pcal power sensors to Working Standards for Hanford (LHO) and Livingston (LLO) observatories used during O2 observing run.

The weighted mean values of α'_{TW} and α'_{RW} for the Hanford and the Livingston observatories used during the O2 observing run are listed in Table. 3.4. The relative uncertainty on these mean values, calculated using Eq. 3.45, is typically about 0.05%; it varies between 0.03% and 0.06%. We used the typical value for calculating the overall uncertainties in the effective relative responsivities.

Type B uncertainty from optical efficiency

The *effective* relative responsivities are calculated with the assumption that the optical losses are equally divided between the input and output paths (and that the ETM reflectivity is 1.0) as shown in Eqs. 3.38a and 3.38b. Lacking measurements that allow us to divide the optical losses between the input and output paths, we use a rectangular distribution (Type-B uncertainty) with full-width equal to the optical efficiency deficit and estimate the uncertainty using the following relation [62]

$$u_{rel}, \mathcal{E}_T = u_{rel}, \mathcal{E}_R = \frac{1}{\sqrt{3}} \left(\frac{1-e}{2} \right). \quad (3.46)$$

Given that the optical losses between the transmitter module and the receiver module are about 1.3% in general, the associated 1-σ uncertainty is about 0.37% ($1.3\%/2\sqrt{3}$).

3.4.4. Uncertainty estimate in Pcal Force Coefficient

The estimate of the overall uncertainty in Pcal Force coefficient Γ_T and Γ_R is calculated by adding the relative uncertainties in all (uncorrelated) terms in Eqs. 3.28 and 3.30 in quadrature. The overall uncertainty is thus given by

$$
u_{rel}, \Gamma_{T/R} = \left\{ \left(u_{rel}, \cos\theta\right)^2 + \left(u_{rel}, \rho_{GS}\right)^2 + \left(u_{rel}, \alpha_{WG}\right)^2 + \left(u_{rel}, \mathcal{E}_{T/R}\right)^2 + \left(u_{rel}, \overline{\alpha'}_{TW/RW}\right)^2 \right\}^{\frac{1}{2}}
\tag{3.47}
$$

The maximum deviation in the cosine of the incidence angle in Eq. 3.47 is bounded by the size of the periscope optics (2 in. diameter) and their incidence angles that relay the beams to the end test mass. The 1-σ (Type B) relative uncertainty in the cosine of the angle is 0.07 %. The relative uncertainty in the components described above that contributed to the uncertainty in Pcal Force coefficients, calculated for the O2 observing run, are shown as an example in Table 3.5.

3.4.5. Uncertainty due to Pcal beam spot misplacements

The misplacements of the Pcal and the interferometer beams introduce error in calibration either by introducing a unwanted rotation of the test mass or through the excitation of the normal modes of the test mass. The impact of the excitation of the test mass normal modes, also referred to as *bulk elastic deformation*, will be discussed in detail in Chapter 5. Here the impact of rotation is discussed. Using Eq. 3.17 to

82

Parameter	Relative Uncertainty
NIST -> GS [ρ_{GS}]	0.51 %
WS/GS [α_{WG}]	0.03 %
Rx/WS [α'_{RW}]	0.05 %
Optical efficiency [$\mathcal{E}_T$]	0.37 %
Angle of incidence [$\cos\theta$]	0.07 %
Force Coefficient (Γ_R)	**0.64 %**

TABLE 3.5. Uncertainty estimate for the receiver module power sensor force coefficient. The NIST calibration and the optical efficiency are the most significant contributors to the uncertainty budget.

account for the apparent length variation caused by rotation, we define $\Delta\mathcal{R}_{(a,b)}$ as

$$\Delta\mathcal{R}_{(a,b)} \equiv |\vec{a}||\vec{b}|\frac{M}{I} \tag{3.48}$$

Considering that the angle between the Pcal force displacement vector and the interferometer beam centroid displacement vector could be between 0 and 360 degrees, the value of the rotation induced apparent displacement factor, $\mathcal{R}_{(a,b)}$, is between 1-$\Delta\mathcal{R}_{(a,b)}$ and 1+$\Delta\mathcal{R}_{(a,b)}$. Because the probability that the value being anywhere between these extremes is equally likely and probability of being outside this range is zero, we treat the uncertainty on this quantity as of Type B. It is given by

$$u_{rel}, \mathcal{R}_{(a,b)} = \frac{\Delta\mathcal{R}_{(a,b)}}{\sqrt{3}} \tag{3.49}$$

<u>Estimates of Pcal beam offsets ($\vec{a}$)</u>

Including the impact of imbalance of the powers in the two Pcal beams, the location of the Pcal center of force is given by:

$$\vec{a} = \frac{\beta \vec{a_1} + \vec{a_2}}{\beta + 1} \tag{3.50}$$

where $\vec{a}_1$ and $\vec{a}_2$ are the displacement vectors of the two Pcal beams about the center of the mirror face and β is the ratio of beam powers, P_1/P_2 [54].

To consider the case where the effects of Pcal beam offset and power imbalance are determined separately, Eq. 3.50 can be re-written by expanding the Pcal beam displacement vectors as

$$\vec{a_1} = \vec{a_0} + \vec{\Delta a_1} \tag{3.51a}$$

$$\vec{a_2} = -\vec{a_0} + \vec{\Delta a_2} \tag{3.51b}$$

where $|\vec{a_0}| = 111.6$ mm (in $\pm y$-direction) is the nominal pcal beam displacement from the center of the optic as shown in Fig. 3.26

Rewriting Eq. 3.50 using Eqs. 3.51a and 3.51b yields,

$$\vec{a} = \vec{a_0} \frac{(\beta - 1)}{(\beta + 1)} + \frac{(\beta \vec{\Delta a_1} + \vec{\Delta a_2})}{\beta + 1} \tag{3.52}$$
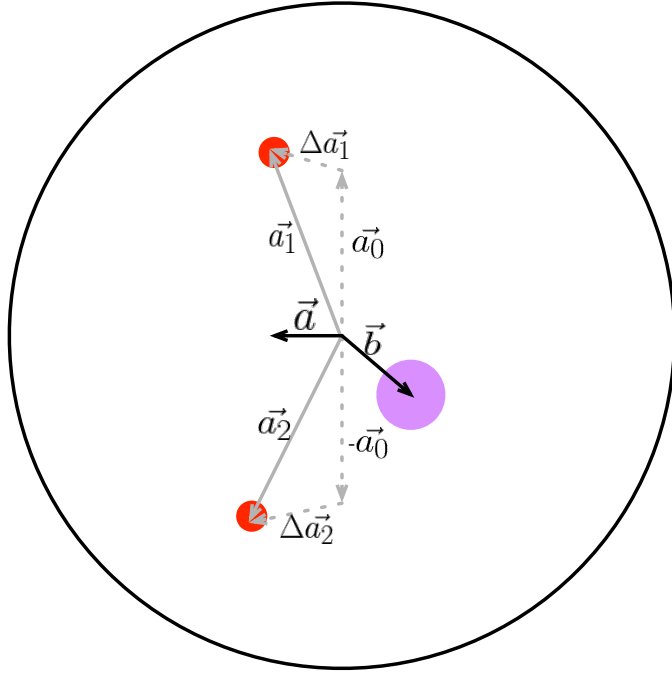
FIGURE 3.26. Schematic showing the positions of the Pcal and interferometer beams on the surface of the test mass. The beam positions and beam sizes are exaggerated for better visualization.

To decouple beam offsets from the power imbalance, the second term in Eq. 3.52 can be rewritten using $\beta = 1 + \delta\beta$. Here, $\delta\beta$ is small because β is within 1-2% of 1.

$$\vec{a} = \vec{a_0}\frac{(\beta - 1)}{(\beta + 1)} + \left(\frac{(1 + \delta\beta)\Delta\vec{a_1} + \Delta\vec{a_2}}{1 + \delta\beta + 1}\right)$$

$$\vec{a} = \vec{a_0}\frac{(\beta - 1)}{(\beta + 1)} + \left(\frac{\Delta\vec{a_1} + \Delta\vec{a_2} + \delta\beta\Delta\vec{a_1}}{2 + \delta\beta}\right) \tag{3.53}$$

Ignoring terms to first order in $\delta\beta$,

$$\vec{a} \approx \underbrace{\vec{a_0}\frac{(\beta - 1)}{(\beta + 1)}}_{\vec{m}} + \underbrace{\frac{(\Delta\vec{a_1} + \Delta\vec{a_2})}{2}}_{\vec{n}} \tag{3.54}$$

85

To estimate the worst-case scenario, we assume that the offset induced by power imbalance is in the same direction as the center of force offset induced by beam position offsets. Thus the maximum magnitude of $\vec{a}$ is $|\vec{m}| + |\vec{n}|$. The offset in the Pcal beam position, $\vec{n}$, can be determined using the Pcal beam localization system described in detail in Sec. 3.2.4. The "effective" beam offset ($\vec{m}$) induced by power imbalance can be determined from the end-station calibration measurement, where

$$\vec{m} = 111.6 \times \left(\frac{\beta - 1}{\beta + 1} \right) \tag{3.55}$$

Estimates of Main Interferometer Beam offsets ($\vec{b}$)

For each ETM, we take the largest observed excursion in the horizontal direction and add it in quadrature with the largest observed excursion in the vertical direction. This gives an upper bound on the expected displacement of the interferometer beams from the center of the ETM.

Uncertainty estimate in $\mathcal{R}_{(a,b)}$ for O2

In order to estimate the rotation-induced uncertainty, we used the maximum value of 0.98 for power ratios between the two Pcal beams (β) observed during O2 observing run to get an effective center of force position offset of 1.1 mm, i.e. $\vec{m} = 1.1$ mm using Eq. 3.55. The moment of inertia, I, was determined from test mass fabrication drawings and the value that produced the maximum rotation of the test mass (in this case, the lowest value) was used. For Pcal beam positions offsets, the displacements estimated using the Pcal beam localization systems were used. For the interferometer beam offsets the worst-case scenario for each ETM was considered from interferometer beam position studies carried out by colleagues at the observatories.

End Station	$\vec{n}$	$\vec{a}$	$\vec{b}$	Mass (M)	$\Delta\mathcal{R}_{(a,b)}$	$u_{rel}, \mathcal{R}_{(a,b)}$
LLOX	3.65	4.75	13	39664	0.0060	0.35 %
LLOY	3.84	4.94	3.6	39608	0.0017	0.01 %
LHOX	7.63	8.73	7.3	39647	0.0062	0.36 %
LHOY	0.70	1.80	5	39641	0.0009	0.05 %

TABLE 3.6. Rotation induced uncertainty for each end test mass (ETM) and the components that were used to calculate them during the O2 observing run.

The values for both the Pcal and interferometer beam position offsets are listed in Table 3.6. Using these values and the mass of each test mass, the rotation-induced uncertainty for each test mass was estimated using Eq. 3.49. They are listed in Table. 3.6. During the O2 observing run, for convenience, the single value (largest from the table) of 0.36 % was used for Pcal error estimation for all test masses.

3.4.6. Uncertainty in Suspension transfer function

The only uncertainty associated with the suspension transfer functions considered during the O1 and O2 observing runs was the uncertainty in the determination of the ETM masses. This relative uncertainty is less than 0.005 %. The comparison between the actual ETM force-to-length transfer function, $S(f)$, to that estimated using the "free mass" approximation is shown in Fig. 3.27. The residual is well below 0.1% for frequencies above 30 Hz, where most of the calibration lines are placed.
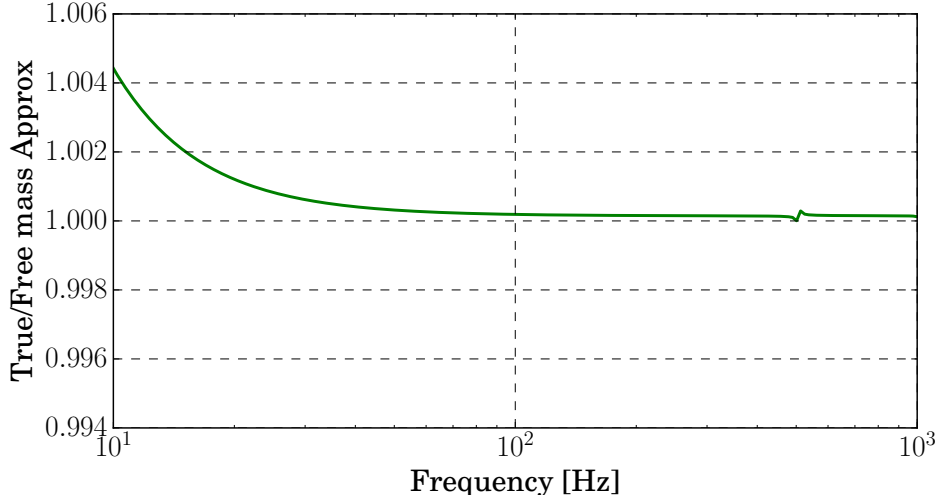
FIGURE 3.27.   Ratio between the actual Advanced LIGO test mass suspension transfer function to the one approximated as a free mass.

3.4.7. Uncertainty in Pcal-induced displacement

The overall uncertainties in the calibration of the Pcal power sensor channels can be estimated by adding, in quadrature, the uncertainties associated with the three major components of Eq. 3.16: the Pcal force coefficient ($\Gamma_{T/R}$), the unintended rotation factor, and the suspension transfer function as

$$u_{rel}, x_{T/R} = \left[\left(u_{rel}, \Gamma_{T/R} \right)^2 + \left(u_{rel}, \mathcal{R}_{(a,b)} \right)^2 + \left(u_{rel}, S(f) \right)^2 \right]^{\frac{1}{2}} \qquad (3.56)$$

The overall calibration uncertainty in Pcal induced length modulation and the factors contributing to it are listed in Table 3.7. Thus for the O2 observing run, the total calibration uncertainty associated with Pcal was less than one percent at 0.75%.

Parameter	Relative Uncertainty
Force Coefficient $[\Gamma_R]$	0.64 %
Mass of test mass $[M]$	0.005 %
Rotation $[\mathcal{R}_{(a,b)}]$	0.40 %
Overall	**0.75 %**

TABLE 3.7. Uncertainty in the Pcal induced length modulation, $x(f)$, in Eq. 3.10. The power calibration and the rotational effect introduce the most significant uncertainty. The rotational effect can be minimized by precise location of the Pcal beams.

3.5. Potential Sources of Systematic Errors

3.5.1. NIST Absolute Power Calibration Accuracy

As mentioned earlier in this chapter, the calibration accuracy of the Pcals relies on our ability to measure laser power accurately. For LIGO, laser power calibration traceable to SI units is provided by NIST, so if there is any systematic error in the NIST calibration, it will manifest as an error in absolute displacement calibration.

Between 2005 and 2007, national metrology institutes from nine countries, five in Europe (France, Germany, Great Britain, Romania, Sweden) and four outside Europe (Australia, Japan, South Africa, United States of America), measured two different radiant laser power sensors (Ophir and Molectron) at various laser wavelengths and power levels. Relevant for LIGO are measurements made at 1064 nm at power levels of 1 W (Note that the Pcal wavelength is 1047 nm, close to the measured 1064 nm wavelength).

The comparisons are summarized in the report, *Final report on EUROMET comparison EUROMET.PR-S2 (Project No. 156): Responsivity of detectors for radiant power of lasers* [67]. Discrepancies between the values reported by NIST and those reported by other national metrology institutes are as large as 3.5%.

Discussion with representatives at NIST revealed that NIST was the only participant in the EUROMET study with a 100 mW-level power standard; all others extrapolated from microwatt cryogenic radiometers. Additionally, transfer standards data collected by NIST over periods as long as 30-40 years provide added confidence that the calibration provided by NIST are accurately traced to the fundamental SI units and the uncertainties stated are accurate.

Currently, NIST is working to initiate a new comparative study at 1-W level among different metrology institutes, using LIGO-style power sensors.

3.5.2. 808 nm Laser Pump Light in Output Beam

The Pcal lasers are optically-pumped Nd:YLF solid-state lasers. The pump light wavelength is 808 nm. Due to the different reflectivity of the optics for 808 nm wavelength light, as well as the different responsivities of the power sensors, 808 nm light in the Pcal laser beams could cause systematic calibration errors. To minimize this potential source of error, the Pcal lasers incorporate a second internal filter to reduce 808 nm light in the output to below the 1 mW level making this a negligible source of error.

3.5.3. Beam Polarization Effects

The reflectivity of the non-normal-incidence optical components in the Pcal beam paths (periscope relay mirrors, ETM, etc.) have different reflectivities for s-polarized

and p-polarized light. The periscope relay mirrors have nominal angles of incidence of 45 deg. They have high reflectivity for p-polarized light and even higher reflectivity for s-polarized light. For reflection from the ETM, the upper (inner) Pcal beam is p-polarized and the lower (outer) beam is s-polarized. However, the angle of incidence on the ETM is only 8.75 degrees and recent measurements performed at all four LIGO end stations show that the reflectivity is at the level of 99.9%.

3.5.4. Frequency Response of Power Sensors

The Pcal power sensor photodetectors are designed to have frequency responses that are flat within 0.01 dB (0.1%) for frequencies from DC to 10 kHz. Measurements made during the assembly and testing of the photodetectors confirmed that they meet this requirement. A similar measurement, comparing Livingston Y-end receiver module photo detector (RxPD) to a Newport M2033 Germanium photodetector is plotted in Fig. 3.28 [68]. It shows that the frequency response is flat at the level of one-tenth of a percent up to 5 kHz.

3.5.5. Amplitude Response of Power Sensors

Non-linear amplitude response of the power sensors could cause systematic errors. During fabrication and testing of the sensors, saturation in the photodetectors was observed if the photocurrents were above 1 mA. The aperture diameter in the photodiode adapters are designed to keep the photocurrents at a level of tens of microamps.
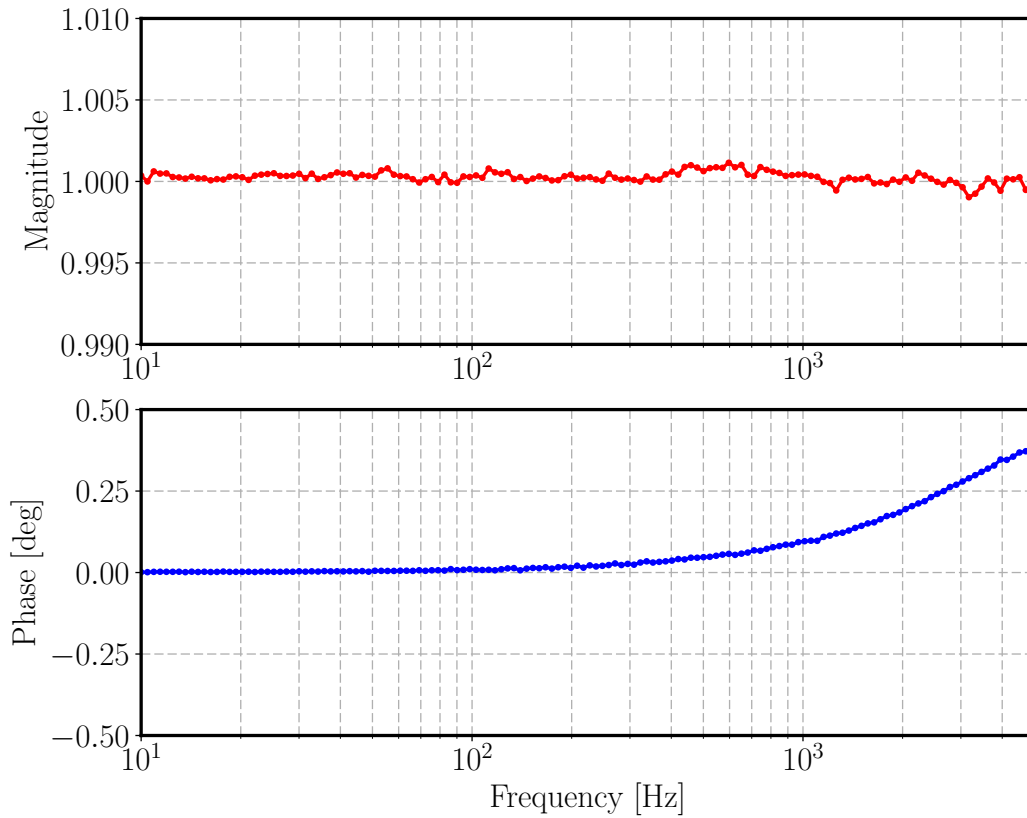
FIGURE 3.28. Frequency Response of the receiver module photodetector (RxPD) compared to a Newport M2033 Germanium photodetector [68].

3.5.6. Laser Beam Diffraction

Laser light that diffracts out of the beams while they propagate from the transmitter module to the receiver module, could impact the Pcal uncertainty. The Pcal laser output beam was propagated over a path length of ~12 m in the lab during the assembly and the power as measured both at the laser output and at the distant location. Differences in power was shown to be within measurement uncertainty.

3.5.7. Temperature Dependence of Power Sensor Responsivity

The temperature coefficient of the InGaAs photodiodes that are used in our power sensors is $\leq \pm 0.1\%/\deg$. The temperature of the measurement laboratory at NIST is controlled to keep temperature variations to below $\sim 1 \deg$ level. The temperatures in the optics laboratory where the Working Standard to Gold Standard responsivity measurements are made varies by several deg C, but this is a common mode variation, i.e. the responsivities of both photodetectors are expected to vary in the same way, so the ratio of responsivities is not expected to vary with temperature.

CHAPTER 4

APPLICATIONS OF PHOTON CALIBRATORS IN ADVANCED LIGO

Some of the contents described in this chapter has been published before in the journal listed below:

S. Karki, D. Tuyenbayev, S. Kandhasamy, et al. "The Advanced LIGO photon calibrators." Review of Scientific Instruments, 87:114503, 2016.

In Advanced LIGO, Photon calibrators operate continuously, during normal interferometer operations, to provide and monitor the calibration of the interferometer output signals. These functions are realized by injecting Pcal excitations at discrete frequencies. They are also used periodically to measure detector parameters– sensing function, actuation function, signs and time delays– that impact the calibrated output signals. These measurements are used to improve the calibration accuracy. Pcals are also used to inject simulated gravitational wave displacements, both continuous and transient, to test the efficiency, accuracy and robustness of the detection pipelines. Furthermore Pcals have been used as low-noise displacement actuators to maintain the resonant lengths of the interferometer arm cavities. Various functions and measurements associated with Photon calibrator are described below in detail. Measurements from only one detector (either LHO or LLO) are chosen to avoid repetition.

4.1. Calibration Lines

The single-frequency length modulations induced using the Pcals are also referred to as *Calibration Lines*. These calibration lines are run at multiple frequencies simultaneously to provide continuous calibration of the interferometer signals and

94

Freq. (Hz)	DFT Length (sec)	Cal Params	Required Pcal Power	
			O2 Sensitivity	Design Sensitivity
36.7	10	Actuation	0.2 %	0.1 %
331.9	10	Sensing	8.0 %	4.0 %
1083.7	60	HF cal. check	75 %	24 %

TABLE 4.1. Photon Calibrator excitation frequencies during normal interferometer operations. DFT intervals and percentage of available laser power required to generate the excitations with SNR of 100, for O2 sensitivity and the Advanced LIGO design sensitivity.

to track changes in the calibration. The nominal frequencies and amplitudes of these Pcal excitations for LHO during O2 observing run are listed in Table 4.1.

Each calibration line frequency is chosen to most effectively inform various interferometer parameters pertaining to the calibration, while avoiding the most sensitive region of the detection band. The line near 37 Hz is used to measure the actuation strength at that frequency and thus tracks temporal changes in the strength of the test mass actuators. The excitation near 332 Hz measures the sensing function at that frequency and tracks temporal change in the optical gain and the *coupled-cavity pole frequency* of the interferometer response. For these lines, SNRs of approximately 100 are required to enable calibration at the one percent level with 10-second integration intervals. The line near 1.1 kHz is used to get an independent check of the calibration far from the cavity-pole frequency. This line utilizes approximately three quarter of the Pcal laser power and requires longer integration time to get an appreciable SNR. These excitation frequencies are also chosen to avoid known potential sources of gravitational wave signals, most of which are rapidly-rotating neutron stars observed electromagnetically as pulsars. A Fisher-

matrix-based approach towards the selection of these calibration line frequencies was also explored and is described in [69, 70].

The amplitude of the laser power modulation required to induce a length modulation with a desired SNR at a given frequency is given by

$$P(f_i) = \left(\frac{c}{2 \cos \theta \cdot S(f_i)} \right) \frac{\Delta L(f_i) \, \text{SNR}(f_i)}{\sqrt{T}} \tag{4.1}$$

where f_i is the modulation frequency, $\Delta L(f_i)$ is the amplitude spectral density of the interferometer sensitivity noise floor, and T is the measurement integration time.

Table 4.1 also lists the percentage of available Pcal modulated laser power required to achieve an SNR of 100 with the listed discrete Fourier transform (DFT) time for each excitation. All the calibration lines listed in table 4.1 are generated using the Pcal system at one of the end station.

During the observing run O2, using the Pcal system at the other end station, the one not being used for primary interferometer calibration, calibration lines were injected at frequencies between 1 kHz and 5 kHz, one frequency at a time, to enable more accurate calibration of the interferometer response at these frequencies. The motivation for and results of these measurements are discussed in detail in Chapter 5.

For the Advanced LIGO Pcals the amplitude spectral density of the maximum modulated displacement that can be achieved using all of the available Pcal laser power is plotted in Fig. 4.1 for a 10-second integration interval. It falls as $1/f^2$ due to the force-to-displacement response of the test mass, from 1×10^{-14} m/$\sqrt{\text{Hz}}$ at 20 Hz to below 2×10^{-19} m/$\sqrt{\text{Hz}}$ at 5 kHz. Fig. 4.1 also shows the displacements induced by the Pcal excitations during normal operation and the interferometer noise floor in Sept 2015. Finally, the requirement for the maximum unwanted Pcal-induced displacement noise, one tenth of the design sensitivity noise floor, is plotted. As the
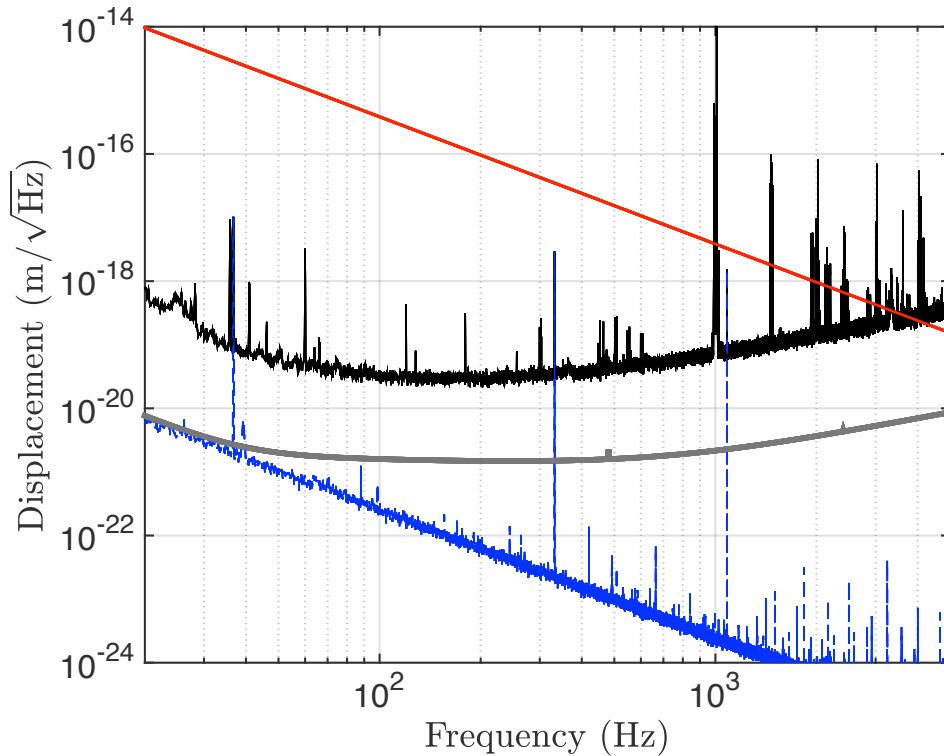
FIGURE 4.1. Maximum modulated displacement using all of the available Photon Calibrator power at one frequency (red). Pcal-induced displacements in Sept. 2015 (blue) along with the Sept 2015 sensitivity noise floor (black) with a 10 second integration time. The gray curve is the maximum allowed unintended displacement noise, one tenth of the design sensitivity noise floor [55].

interferometer sensitivity improves and the noise floor approaches design levels, the amplitude of the Pcal excitations can be reduced proportionately, reducing the laser power required and therefore also the level of unwanted displacement noise.

4.2. Frequency Response Measurements

In order to measure the frequency dependent sensing and actuation functions of the interferometer, a series of swept-sine measurements are made. A sensing function measurement is made by comparing the interferometer response to differential length variation, $d_{err}(f)$, to the excitation induced using a Pcal system, $x_T(f)$ and

compensating for the suppression caused by the differential arm length (DARM) feedback control loop shown in Fig 2.4. The measured interferometer sensing function, $C^{(meas)}(f)$, is thus given by

$$C^{(meas)}(f) = \frac{d_{err}(f)}{x_T(f)}[1 + G(f)] \qquad (4.2)$$

where the open-loop transfer function, $G(f) = A(f)C(f)D(f)$, is measured separately using in-loop suspension actuators over the same range of frequencies as above. For frequencies above 1 kHz, the open-loop gain is negligible and thus the sensing function is approximated by

$$C^{(meas)}(f) \approx \frac{d_{err}(f)}{x_T(f)} \qquad (4.3)$$

A comparison between a sensing function "model", determined using Eq. 2.12, and the measurement made using Pcal and estimated using Eq. 4.2 is shown in Fig 4.2 as an example.

An actuation function measurement for each stage in the cascaded pendulum is achieved by first measuring the interferometer response to differential length variation, $d_{err}(f)$, to excitations induced using the actuators on each stage, $x_i(f)$ which is given by

$$\frac{d_{err}(f)}{x_i(f)} = \frac{A_i(f)C(f)}{1 + G(f)} \qquad (4.4)$$

A second measurement is made by comparing the interferometer response to differential length variation, $d_{err}(f)$, to an excitation induced using the Pcal system, $x_T(f)$, at the same frequencies as the cascaded pendulum stage transfer function measurements.

$$\frac{d_{err}(f)}{x_T(f)} = \frac{C(f)}{1 + G(f)} \qquad (4.5)$$
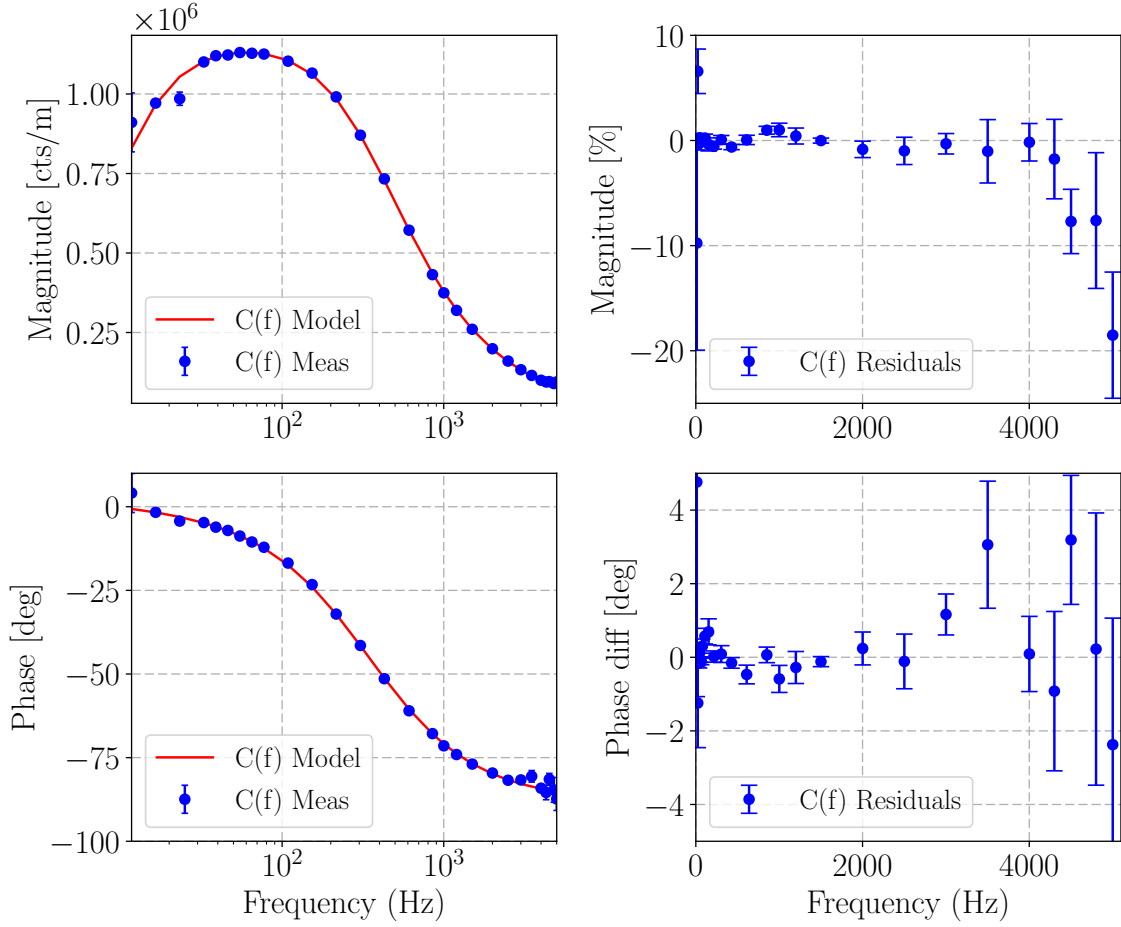
FIGURE 4.2. Comparison between a model of the interferometer sensing function and measurement made using the Pcal system. The plot on the right shows the residuals between the measurement and the model.

In order to make sure there is no change in the detector response between the first and second swept-sine measurements, the second measurement is started just a few minutes after the first so that it does not corrupt the first measurement but still follows closely in time with the first sweep. Combining the two set of measurements described by Eqs. 4.4 and 4.5, the measured actuation function, $A_i^{(meas)}(f)$, can be calculated using the following relation

$$A_i^{(meas)}(f) = \frac{d_{err}(f)}{x_i(f)} \frac{x_T(f)}{d_{err}(f)} \tag{4.6}$$

99

A comparison between an actuation function "model", determined using Eq. 2.13, and the measured transfer function of different stages of the pendulum, estimated using Eq. 4.6 is shown in Fig. 4.3.
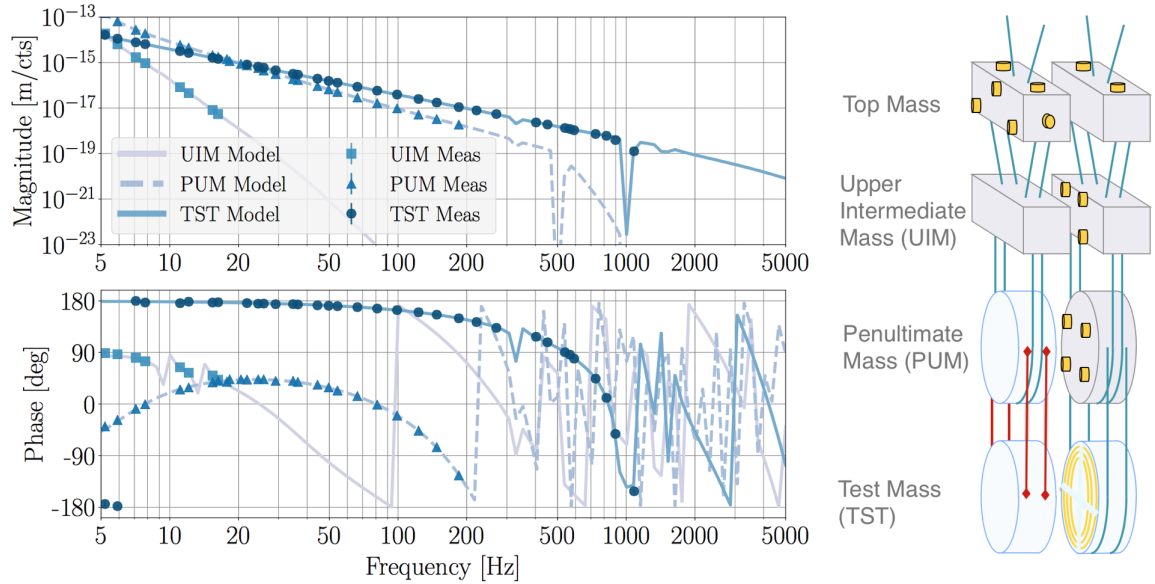
FIGURE 4.3. Left: Comparison between actuation function models, determined primarily from the mechanical response, for different stages of the pendulum and measurement made using the Pcal system. Right:Cascaded quadruple pendulum showing the top mass, PUM, UIM and the test mass (TST) [34]

During the course of observation runs, although the calibration is tracked by the time-varying parameters calculated using the calibration lines, to assess the accuracy of the calibration over a wide range of frequencies, these swept-sine measurements are made during dedicated calibration interludes, the length of which are minimized in order to maximize observing time. Thus, the Pcal displacement amplitudes must be sufficiently large to complete the measurements in a relatively short time. Fig. 4.4 shows a typical transfer function from 20 Hz to 1.2 kHz, with approximately 60 points. The measurement was made in approximately one hour; the measurement statistical uncertainties, calculated from the coherence of the measurements, are approximately 1% in amplitude and 1 deg. in phase for frequencies between 20 Hz and 1.2 kHz .
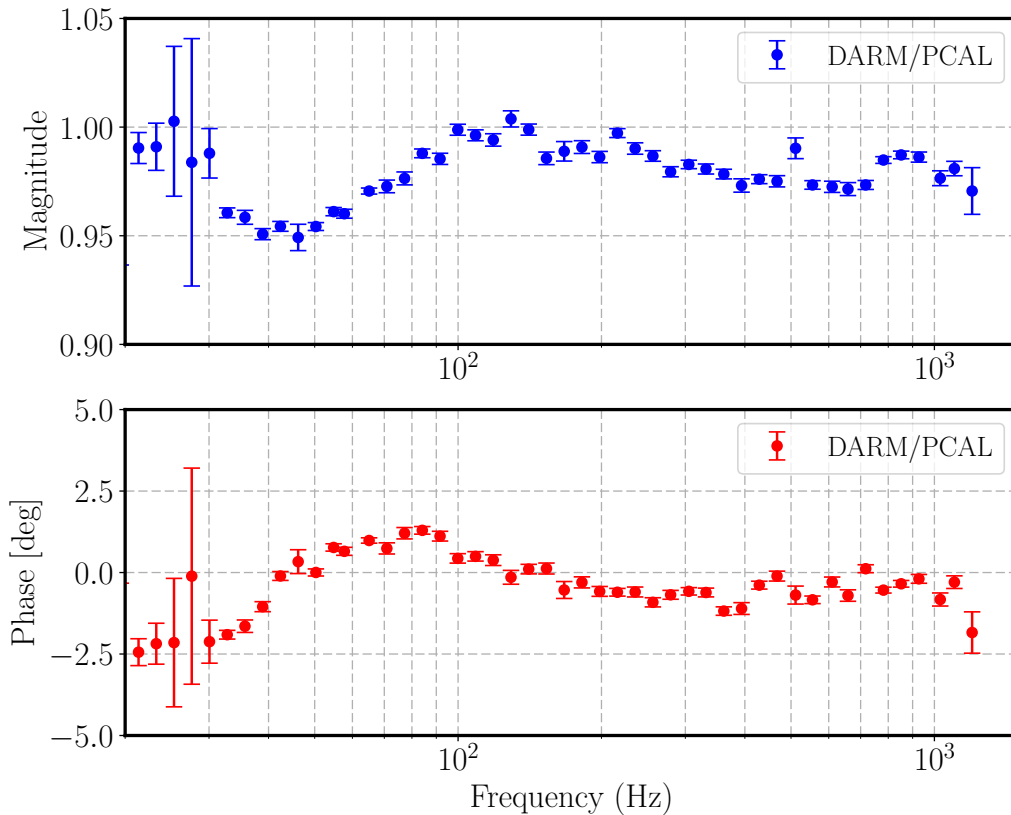
FIGURE 4.4. Magnitude and phase of a typical swept-sine measurement of the transfer function between displacement induced (and calibrated) by the Pcal and the calibrated output of the interferometer [55].

The statistical variation are higher in the band from 20 to 30 Hz due to resonances in the suspension systems of ancillary interferometer optics.

Rather than injecting Pcal excitations at discrete frequencies, the transfer function can also be measured simultaneously by injecting a broadband signal. This can potentially make the calibration comparison process faster and more accurate. It also has the potential of revealing features in the transfer function that might be missed in measurements made only at discrete frequencies. However, this type of measurement is also limited by the available Pcal laser power. To assess the
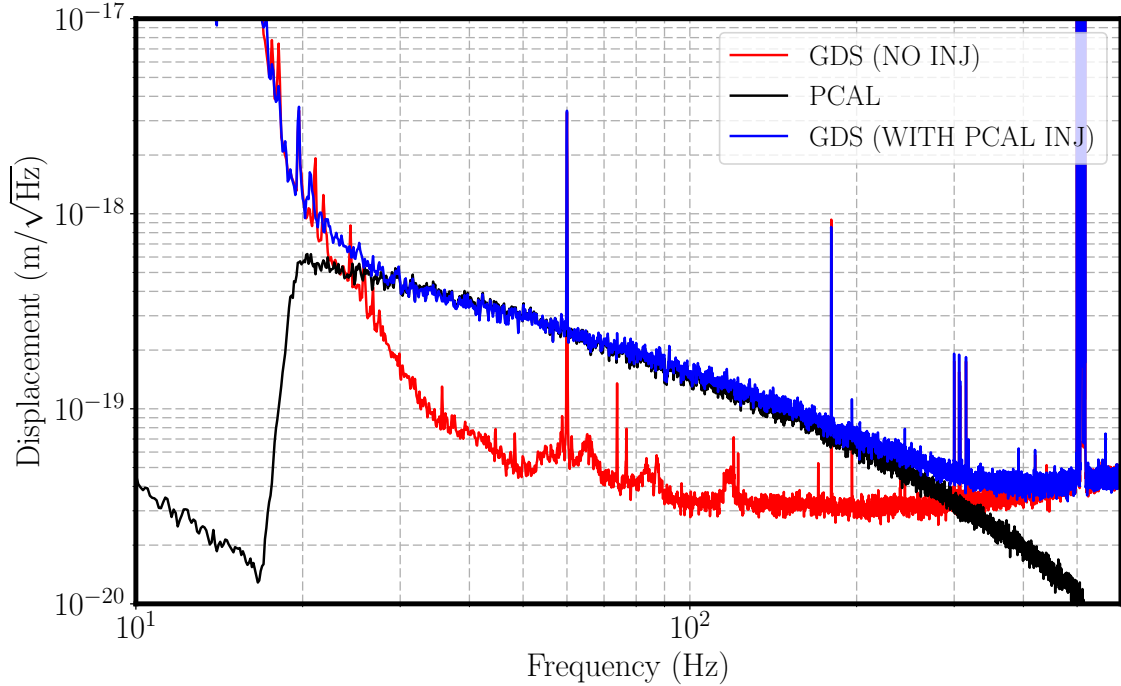
FIGURE 4.5. Pcal broadband displacement excitation (black) and calibrated interferometer output signal with (blue) and without (red) the Pcal excitation [55].

feasibility of this method, a broadband signal covering the 30-300 Hz frequency band, band-pass filtered to attenuate it at higher and lower frequencies, was injected into the Pcal Optical Follower Servo. Fig. 4.5 shows the displacement injected by the Pcal together with the calibrated interferometer output signal both with and without the Pcal excitation. No unexpected discrepancies that might have been missed by the discrete-frequency transfer function measurement were identified. As the sensitivity of the interferometers improves, the band over which this method is useful will increase. These measurements have not been used extensively thus far, but will potentially be a part of routine calibration measurements during future observing runs.

4.3. Differential-mode and Common-mode Actuation

Normally, the differential length response of the detector is calibrated using one Pcal system varying the length of only one interferometer arm. The Advanced LIGO interferometers, however, have Pcal systems installed at both end stations. They can be used simultaneously to produce either pure differential arm length variations, where the two arms of the interferometer stretch and contract out of phase or pure common arm length variations, where the arms stretch and contract in phase. Comparing differential and common excitations, enables diagnosing systematic differences between the two arms and quantifying the coupling between common-arm motion and differential-arm motion.

A comparison of differential-and common-mode actuation of the interferometer using the Pcals is shown in Fig. 4.6. Both Pcal systems induced modulated displacements of equal amplitudes, as determined by the calibration of the Pcal receiver module power sensors. The relative phases of the excitations was changed from 0 deg. (in phase) to 180 deg. (out of phase) to transition between common and differential-mode actuation. Less than 0.2 % of the common-mode motion is sensed as differential-mode motion by the interferometer.

The ability to precisely vary the amplitude and phase of the injected length modulations enables high-precision calibration measurements without inducing large amplitude lines in the output signal. This can be realized by canceling length excitations injected by other actuators with Pcal lines injected at the same frequency but 180 deg. out of phase.

103
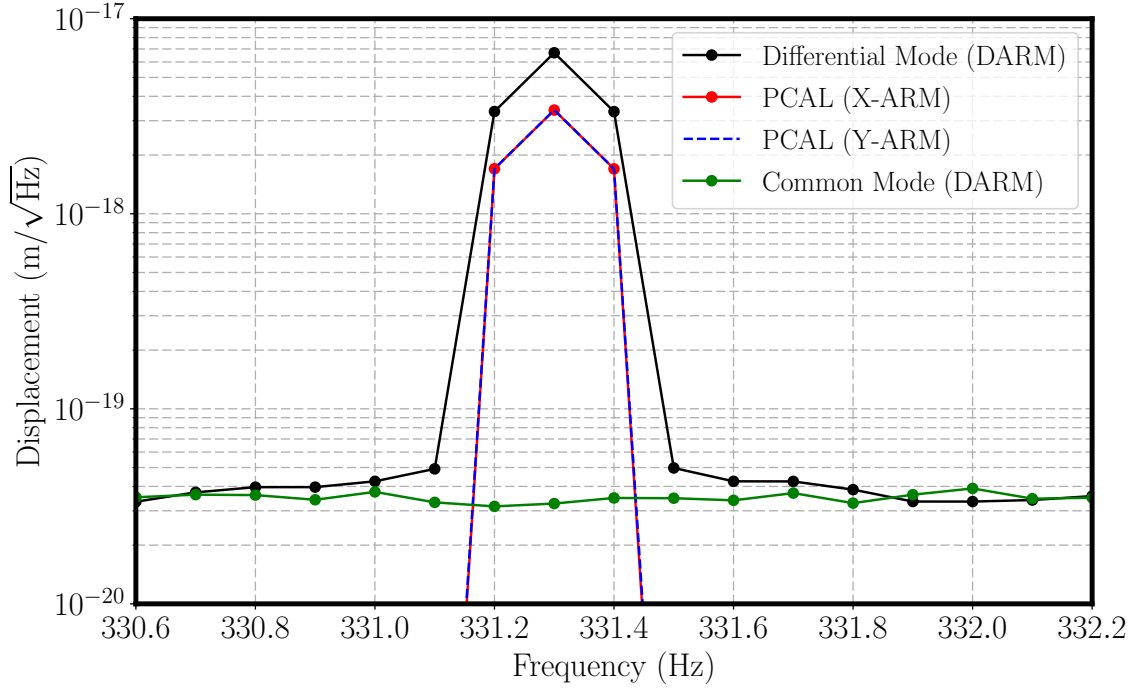
FIGURE 4.6. Measurement using the Pcal modules at both end stations to induce equal-amplitude modulation of the positions of the test masses (overlapping red and blue) in *common mode* (green), 0 deg. relative phase, and *differential mode* (black), 180 deg. relative phase [55].

4.4. Measuring Time Delays and Signs

Radiation pressure actuation via the Pcals has a simple phase relationship between the length excitation (modulated laser power detected by the receiver module power sensor) and the induced motion of the test mass. For a sinusoidal length excitation introduced using Pcal, the Pcal readback signals, $x_p(t)$, and the interferometer output signal, $x_d(t)$, can be written as

$$x_p(t) = A_p \sin(2\pi f t_p + \phi_p) \tag{4.7a}$$

$$x_d(t) = A_d \sin(2\pi f t_d + \phi_d) \tag{4.7b}$$

104

The total phase difference between these two signals is given by

$$\theta = 2\pi f(t_p - t_d) + (\phi_p - \phi_d) \tag{4.8}$$

where $\Delta t = (t_p - t_d)$ gives the time delay between the length excitation and the induced motion and $\Delta\phi = (\phi_p - \phi_d)$ gives the frequency independent phase change between these two signals [71].

Using multiple Pcal excitations we can measure the time delays (Δt) in the response of the detectors to motion of the test masses (and consequently gravitational waves). Understanding these delays is crucial for localizing the source of the detected gravitational waves on the sky using two or more detectors. Previously in LIGO, two frequencies were used to measure the delays yielding timing uncertainties on the order of 10 μs [72]. With the upgraded Advanced LIGO Pcal data acquisition and better timing standards, similar measurements are easily performed at many frequencies, or even broadband, achieving measurement uncertainties on the order of a few μs. Fig. 4.7 shows the results of such measurements made at frequencies between 100 and 1400 Hz during the first Advanced LIGO observing run. The straight line fit to the data shows a time delay of 103.2 ± 2.4 μs (105.3 ± 2.0 μs). These delays arise from several sources-, the digital data acquisition (76 μs), analog electronics (20 μs) and light travel times in the arms (13 μs).

For frequencies much larger than the 1 Hz resonances of the test mass suspension system, the induced motion of the test mass is 180 deg. out of phase with respect to the excitation signal. This property of Pcal excitations was exploited for the initial LIGO detectors to investigate the sign of the calibrated interferometer output signals [72]. Confirming the relative signs of the interferometer outputs also impacts the sky localization of gravitational wave sources for a network of detectors.
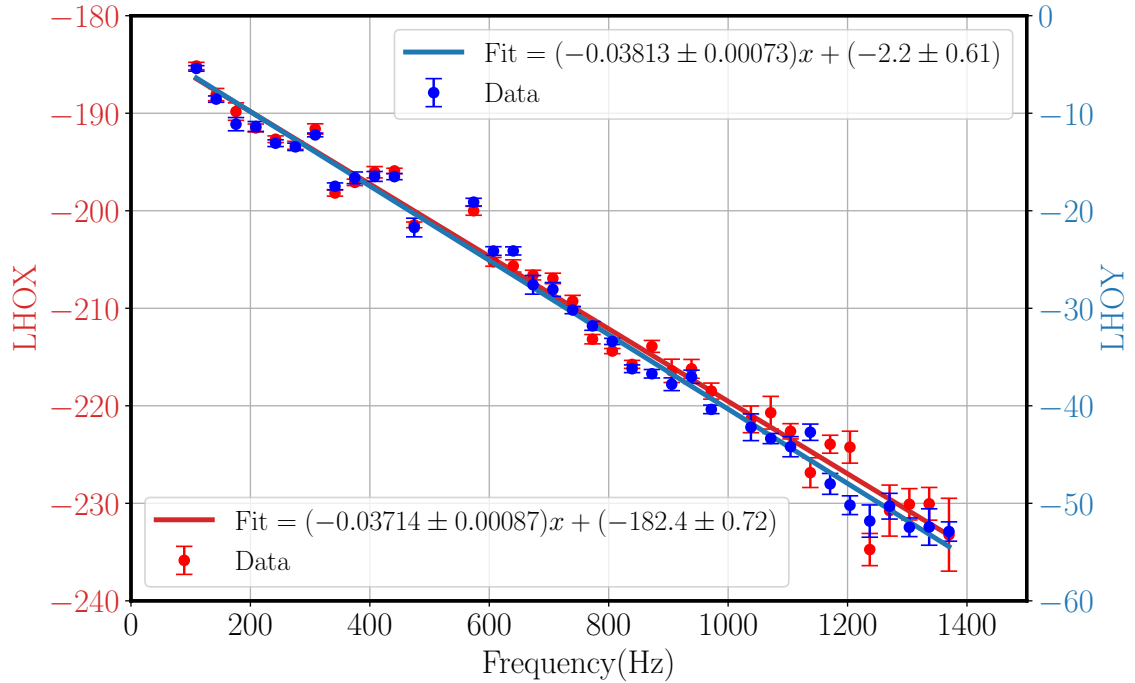
FIGURE 4.7. Interferometer output signal timing measured using Pcal excitations. The least squares fit to the data shows the expected phase shift at low frequency and a delay of 103.2 ± 2.4 μs for the X-arm and 105.3 ± 2.0 μs for the Y-arm.

In order to confirm the sign of signals, we take that the strain of the interferometer to be defined as

$$h = \frac{\Delta L}{L} = \pm \frac{L_x - L_y}{L} \tag{4.9}$$

with the freedom to choose the sign as per our convention which is chosen to be '+' for Advanced LIGO. The results, plotted in Fig. 4.7, show that the relative phase ($\Delta\phi$) between the Pcal signal and the interferometer output signal is $\sim$180 deg. for the Pcal on the X-arm and $\sim$0 deg. for the Pcal on the Y-arm. This shows that the interferometer output is maximum when the X-arm gets longer and is minimum when the Y-arm gets longer. This confirms that the interferometer strain has the '+' sign

as defined by Eq. 4.9. The results of measurements like these are used to model the response of the interferometers to gravitational waves [34].

4.5. Time Varying Parameters
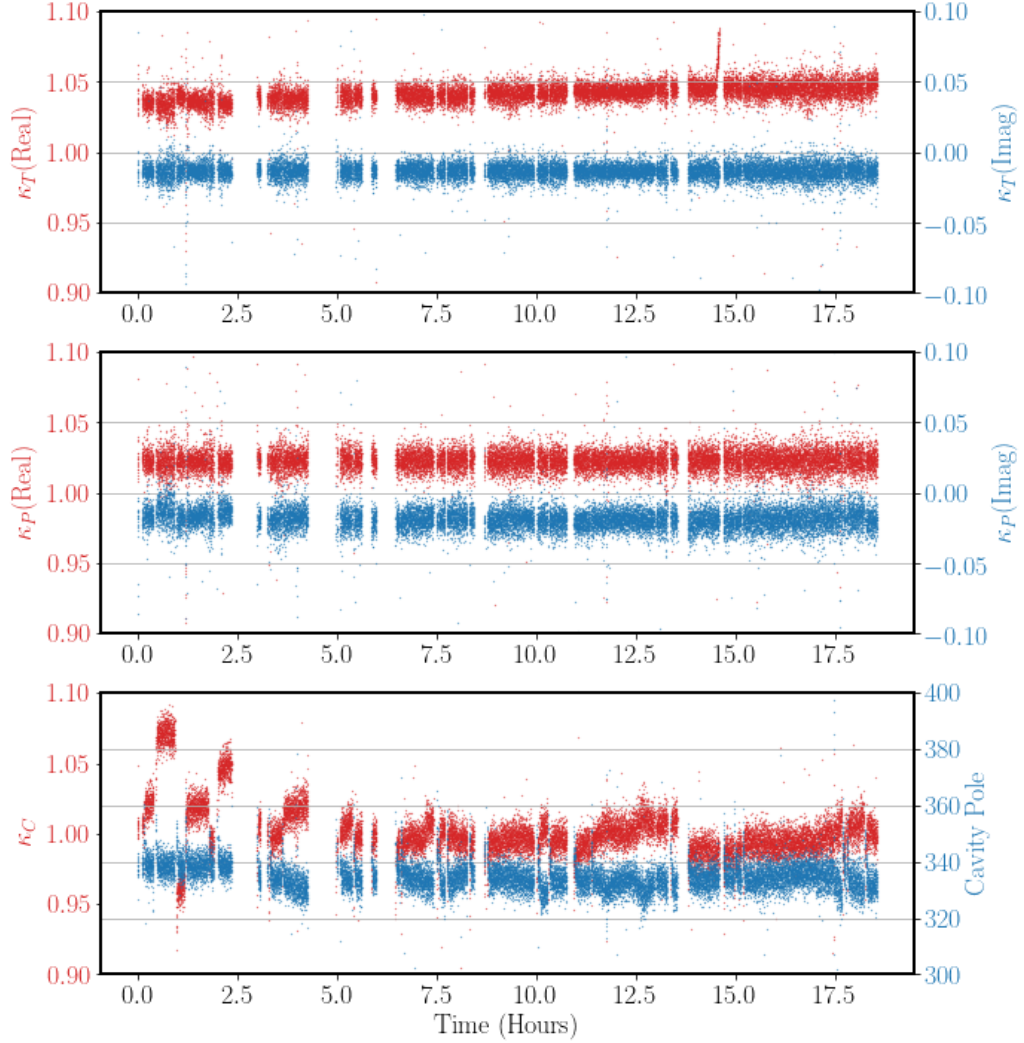
FIGURE 4.8. Calibration parameters that track changes in the calibration of the interferometer. κ_T, κ_P and κ_C track frequency-independent scalar parameters and Cavity-pole tracks changes in the pole frequency of the interferometer response.

The response of the interferometer to differential length variations changes slowly over time due to the changes in various interferometer parameters. These include

the actuation strength of the test mass actuators and the alignment of the optical cavities. The parameters used to track these temporal changes are incorporated into the sensing and actuation functions given by Eq. 2.12 and 2.13 respectively. These slow temporal changes are monitored using the calibration lines listed in table 4.1 and produced using the photon calibrator system. The frequency of these calibration lines are selected to optimize the calculation of these time-varying parameters. As an example, some of these parameters that were calculated over a period of 24 hours are plotted in Fig. 4.8 [73].

Since the calibrated interferometer signal is directly dependent on the accuracy of the sensing and actuation functions, these changes need to be compensated for to improve calibration accuracy. During the first and second observing runs some of these time-varying calibration parameters were used to correct the interferometer output data in low latency (less than 10 seconds), while others were tracked and corrected later. The application of these time-varying parameters improved uncertainty in the calibration from approximately 10% in magnitude and 10 deg. in phase to 3% in magnitude and 2 deg in phase [74].

For the upcoming (2019) O3 observing run, the infrastructure is in place to correct these time-varying calibration parameters within the LIGO's real-time data acquisition (front-end) system which will provide the most accurate calibration in real-time. These real-time corrections will enable the production of calibrated gravitational wave data with calibration uncertainty at the level of 3-4% in magnitude and about 5 degrees in phase. However, there are some high frequency effects that cannot be corrected within the front-end model that will be corrected in the offline strain generation pipeline (GDS), improving the overall uncertainty to less than 3% in magnitude and 2 degrees in phase.
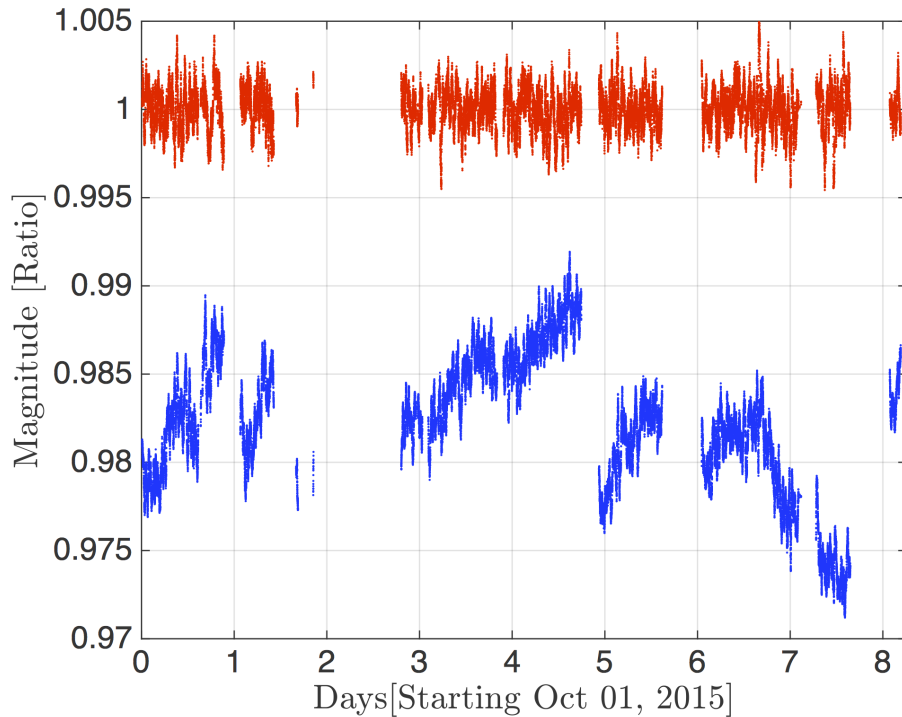
FIGURE 4.9. Trends of the ratio between the displacement reported by the interferometer output signal and the displacement calculated from the Pcal power sensor in the receiver module using the excitation at 332 kHz. Blue: uncorrected data showing the slow temporal variations in the interferometer parameters. Red: corrected data after applying the calculated time-varying correction factors.

The slow variations in the interferometer calibration, measured using a Pcal line near 332 Hz, over an eight day period in Sept. 2015 are shown in Fig. 4.9. The slow variations in the calibrated output signal are as large as 3%. Also shown in Fig. 4.9 are the calibration data that were corrected for the observed slow variations using calibration parameters calculated using the Pcal excitations. The technique used to calculate these time-varying calibration parameters and its application to the data in order to improve the calibration accuracy is described in detail in [73] and [75].
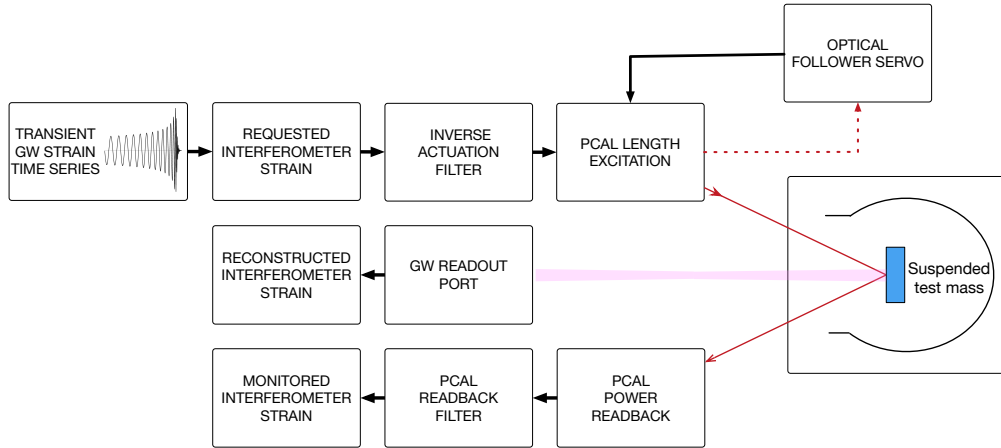
FIGURE 4.10. Block overview of the Advanced LIGO hardware injection system [56].

4.6. Hardware Injections

Hardware injections are simulated gravitational-wave displacements injected into the interferometer to understand the response of the interferometer to gravitational wave signals and to test the robustness and efficiency of the detection pipelines. In Advanced LIGO, hardware injections are made via the Pcals. The simulated gravitational wave time series are sent to the Pcals which actuate (displace) the end test mass of the interferometer via laser power modulation to mimic a gravitational wave passing through the detector as shown schematically in Fig. 4.10. The high-bandwidth Optical Follower Servo ensures that the Pcal power modulation closely matches the analog signal injected at the input of the servo. A set of digital infinite impulse response (IIR) filters, referred to as "inverse actuation filters," convert the requested interferometer strain signal into an Optical Follower Servo input signal that produces an equivalent modulation of the differential arm lengths.

These inverse actuation filters are designed by making a transfer function measurement between the excitation channel and the readback photodetectors and

incorporating the measured transfer function into the Pcal actuation path using a set of zeros and poles. These inverse actuation filters provide calibration accuracy on the order of a few percent in magnitude but have significant phase distortion. The phase distortion is due to phase delays of anti-imaging filters and the physical time delays of the digital control system which cannot be compensated by the inverse actuation filters because the digital IIR filters allowed by the Advanced LIGO control system must be casual. These phase delays can be compensated later during analysis. One can compare the recovered signal to the signal measured by the readback photodetector for a more accurate comparison. Detail description of the use of the Pcals as hardware injection tools can be found in [56].

4.7. Differential Arm Actuator

Photon Calibrators have also been used as actuators for the differential length degree of freedom (DARM) to keep the interferometer in lock during observing runs [76]. This is achieved by feeding the part of the control signal in the DARM loop that drives the test mass to the Pcal Optical Follower Servo input and thus driving the lowest test mass stage using the Pcal system. The advantage of Pcals over the electrostatic drives (ESD) that is currently used as the actuator, is that it is not sensitive to charge that accumulates on the optic. This charge accumulation has caused the electrostatic drive actuation function to drift over time.

CHAPTER 5

CALIBRATION IN THE HIGH FREQUENCY REGIME

5.1. Astrophysical Motivation

As mentioned in Chapter 2, gravitational-wave astrophysicists have great interest in gravitational waves originating from neutron star mergers, knowing that these signals will help to understand the physics of the densest matter in the universe. There are numerous models that predict different outcomes for the merger of binary neutron stars. The merger results in one of the following four possible outcomes: (i) formation of a black hole, (ii) formation of a stable neutron star, (iii) formation of a supramassive neutron star, or (iv) formation of a hypermassive neutron star.

If the component mass of the merging neutron stars are large enough and the resultant merger does not have a mechanism to resist gravitational collapse, the merger results in a black hole. If the remnant mass is smaller than the maximum mass allowed for a neutron star, the merger will result in a stable neutron star.

However, if the remnant is a uniformly rotating neutron star the maximum allowed mass could be 15-20 % larger than the one for non-rotating neutron star. Neutron stars with these large masses, called supramassive neutron stars, will eventually collapse into a black hole if there is process to dissipate the angular momentum. The most likely dissipation processes are EM and GW emission. Some resultant merger remnants could have mass greater than a uniformly rotating star, but are prevented from collapsing through support from differential rotation and thermal gradients. This type of remnant called a hypermassive neutron star, eventually
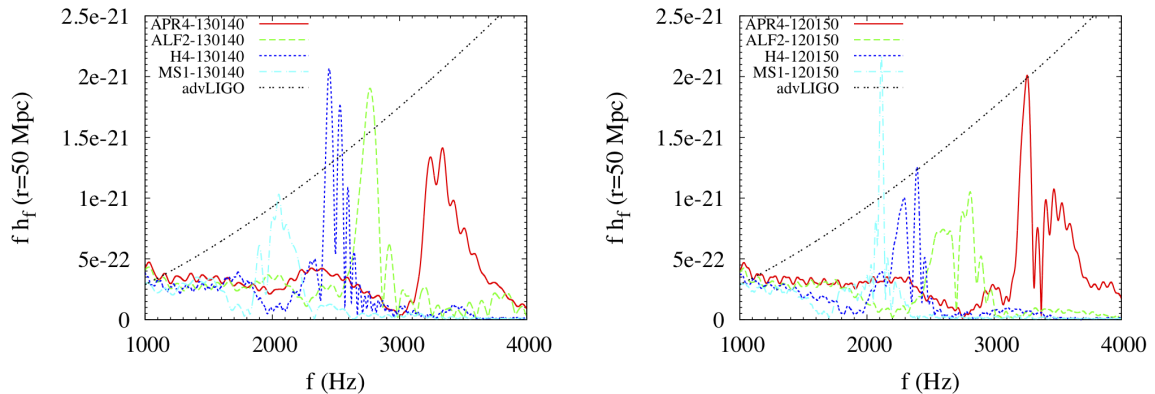
FIGURE 5.1. Fourier spectra of gravitational waves for different models of BNS mergers. The amplitude is shown for the hypothetical event at a distance of 50 Mpc along the direction perpendicular to the orbital plane (the most optimistic direction). The black dash curve is the noise spectrum of the Advanced LIGO optimized for the detection of gravitational waves at higher frequencies [78].

collapse to a black hole through neutrino emission and magnetic braking of the differential rotation [77].

The post merger GW emission from these systems is dominated by broad secondary and tertiary peaks in the 1.8 to 4 kHz range as shown in Fig. 5.1 [78]. The post merger frequency is model-dependent and the post-merger peak frequency depends on the stellar radius as shown in Fig. 5.2 [79]. The mass of the system can be determined from the low frequency inspiral signals. The simultaneous measurement of mass and the radius of these neutron stars system using the inspiral and the post-merger signal will enable determination of the Equation of States (EOS) of these systems. The detection of the post-merger signal from these systems is possible with the Advanced LIGO operating at full design sensitivity and probable with the next generation of gravitational wave detectors [80]. Thus, in order to accurately estimate the astrophysical parameters and maximize the science impact, accurate calibration of the gravitational wave data in the frequency regime of these signals will be crucial.
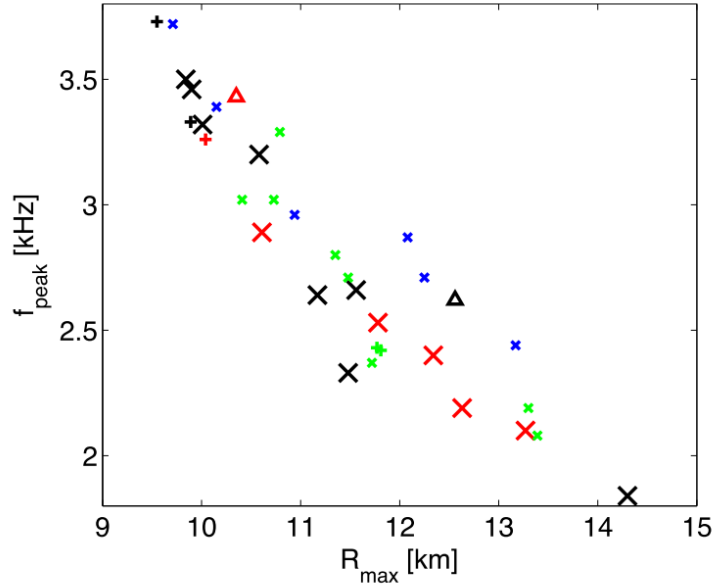
FIGURE 5.2. Peak frequency of the postmerger GW emission versus the radius of the maximum-mass configuration of non-rotating neutron stars for different equations of state [79].

Calibration of the Advanced LIGO detectors in this high frequency regime requires careful consideration of various factors. They include accurate compensation of signal distortion caused by analog electronics and digital systems and taking into account the error introduced by using an approximated single-pole model of the interferometer response. Furthermore, using forces to measure the calibration in this regime will cause the test mass to deform, introducing significant errors. This chapter discusses various aspects of interferometer calibration at higher frequencies and prescribes a method to obtain better calibration at higher frequencies by correcting the errors due to test mass deformations.

5.2. Single-pole Approximation

The response of the interferometer output signal to length variations depends on the reflectivity of the arm cavity mirrors and the light travel time between the mirrors in the cavity. It is given by

$$H_L(i\omega) = \frac{1 - r_a r_b}{1 - r_a r_b e^{-2i\omega T}} \tag{5.1}$$

where r_a and r_b are the reflectivity of the input and end test mass mirrors of the Fabry-Perot cavities and $T = L/c$ is the time that light takes to travel between these mirrors [81].

In the current Advanced LIGO configuration, the interferometer response to length variation can be approximated by a single-pole low pass filter with a characteristic pole frequency called the 'cavity-pole' and an appropriate gain factor. The approximate normalized transfer function is given by

$$C(f) = \frac{1}{1 + if/f_0} \tag{5.2}$$

This approximation is often made in order to reduce the parameters needed to describe the response and thus simplify the interferometer model. Comparison between the exact response and an approximated single-pole response is plotted in Fig. 5.3. As seen from the plot, the single-pole approximation is valid, in magnitude, within well-below 1% for frequencies below 1 kHz, but becomes as large as 3% at 5 kHz. The error in phase is larger even at lower frequencies, but it can be compensated using an appropriate time delay in the interferometer model. Thus, in order to get the calibration of the detector within a few percent at frequencies above one kilohertz,
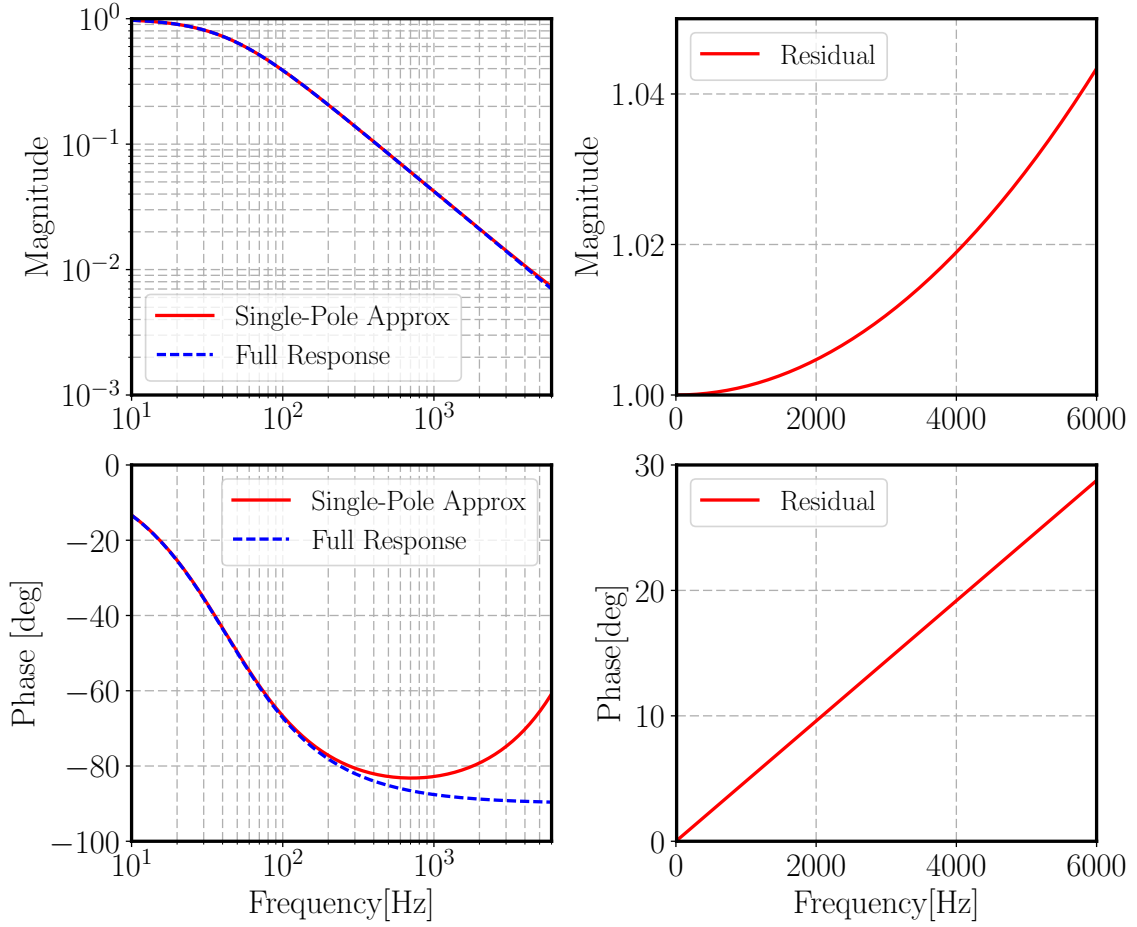
FIGURE 5.3. Comparison between the exact and an approximated single-pole response of the interferometer to the length variations. The discrepancy between the two is as large as 3% at 5 kHz. the large discrepancy in the phase can be corrected by adding an appropriate time-delay.

one must either implement the full response or correct for the errors arising from using the single-pole approximation.

5.3. Digital and Analog Filters

The displacement induced by the gravitational waves in the interferometer arms is not measured as a displacement of the test masses, rather as the force required to keep the test mass in position when the passing gravitational waves produce relative

116
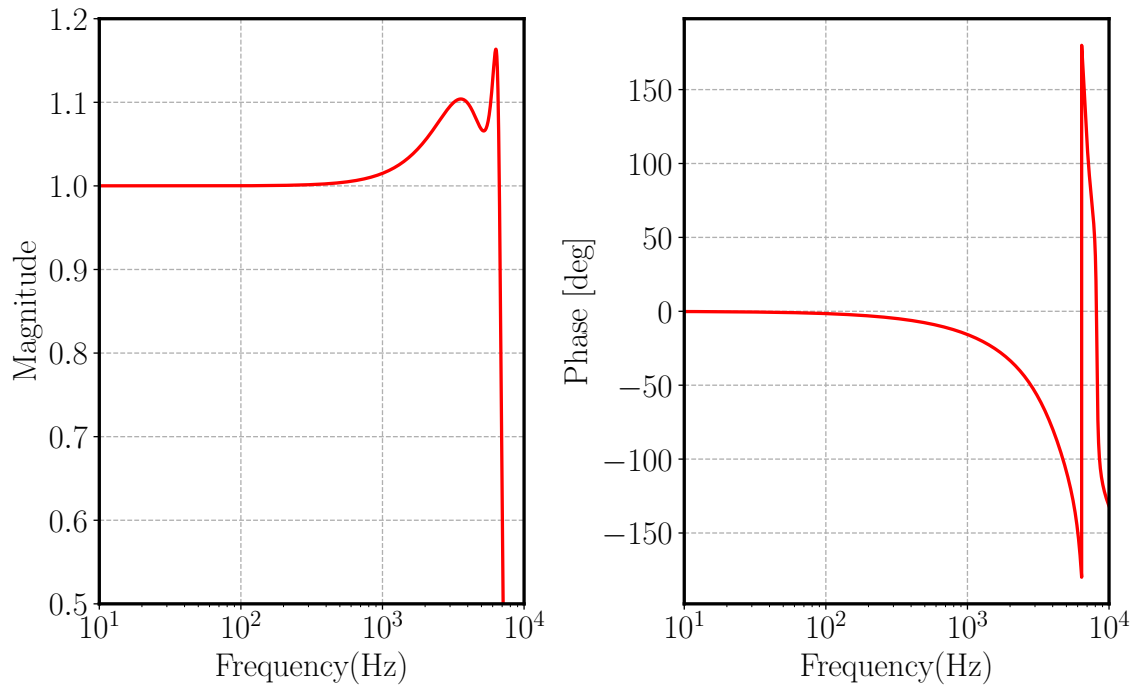
FIGURE 5.4. Transfer function of a decimation filter that down-samples signals from 64 kHz to 16 kHz.

strain variations. When they are operating at their most optimal configuration, the interferometer arms are kept at resonance using a control loop that is referred to as the Differential Arm (DARM) length control servo. The equivalent displacement from an external force is thus reconstructed from interferometer output signals that involve the DARM servo.

The impact of analog electronics and digital systems on these signals during signal conditioning are severe at higher frequencies as shown in Fig. 5.4, as an example, for a 64 kHz to 16 kHz down-sampling digital filter. The transfer functions of the analog electronics can be measured very accurately and those of the digital systems are known to arbitrary precision and thus are compensated to get an accurate and precise response. But there are several components in each signal path that need to be correctly accounted for, and thus a careful consideration of each component is

necessary to realize an accurate interferometer calibration. The block diagram C.1 in Appendix D gives a detailed representation of the different signal paths and the associated components required for interferometer calibration.

5.4. Bulk Elastic Deformation: Modeling

Possible errors in calibration due to the impact of *bulk elastic deformation* of the test masses caused by the applied calibration and actuation forces was first studied by Afrin Badhan, et al. [82] and later by P. Daveloza, et al. [59] and Nicola De Lillo [83]. It was shown that the deformations due to these forces can be represented by a linear combination of the normal modes of the test mass. For Advanced LIGO's frequency band, the contribution from the lower-order *butterfly* and *drumhead* mode is significant. So, in order to reduce the error in calibration due to this effect, the Pcal beams are placed at the nodal circle of the *drumhead* mode. This reduces the deformation of the mirror in the *drumhead* mode shape, it efficiently deforms the mirror in the lower-resonant-frequency *butterfly* mode. However, when the interferometer beam is centered on the test mass surface, the error due to *butterfly* mode integrates out to zero over the central circular region for .

In cases where the Pcal beams are not at their optimal positions and/or the interferometer beam is not at the center of the optic, the displacement sensed by the interferometer can be written as

$$
\begin{aligned}
x_{\text{tot}}(f) &= x_{\text{rigid}}(f) + \sum_m x_m(f) \\
&= x_{\text{rigid}}(f) \left[1 + \frac{\sum_m x_m(f)}{x_{\text{rigid}}(f)} \right]
\end{aligned}
\tag{5.3}
$$

118

where $x_{\text{rigid}}(f)$ is the free mass motion of the test mass, considering the test mass as a rigid body and calculated using Eq. 3.10 and $\sum_m x_m(f)$ is the apparent test mass motion due to the deformation of the test mass and includes contributions from all of the natural vibrational (normal) modes of the test mass [84]. The term inside the square brackets is a frequency dependent factor, $\mathcal{G}_{(a_i,b)}(f)$, that can be estimated using finite element analysis (FEA) as

$$\mathcal{G}_{(a_i,b)}(f) = \left[1 + \frac{\sum_m x_m(f)}{x_{\text{rigid}}(f)}\right] = \left[\frac{x_{\text{total}}}{x_{\text{rigid}}}\right]_{\text{FEA}} \tag{5.4}$$

where the a_i's are the positions of the Pcal beams and b is the position of the interferometer beam relative to the center of the face of the optic.

5.4.1. COMSOL Modeling

The sensed displacement of the test mass can be estimated using the finite element analysis tool COMSOL Multiphysics, referred to as COMSOL hereafter. For simulation purposes two models of the test mass were used: the actual Advanced LIGO ETM 3D model imported into COMSOL from a SolidWorks drawing which has flat cuts on the sides of the optics and ears glued on each flat that are used as anchor points for suspension fibers as shown in Fig. 5.5, and a perfect cylinder without the flats but with the diameter and the thickness same as that of the Advanced LIGO test mass. Since it is easier to, at least qualitatively, understand the dynamics of a symmetric cylinder, it provides a good consistency check to the results of an actual Advanced LIGO test mass.

For all these COMSOL simulations, we assume that the test mass obeys the dynamics of free mass motion. This assumption is fairly accurate for a test mass

119
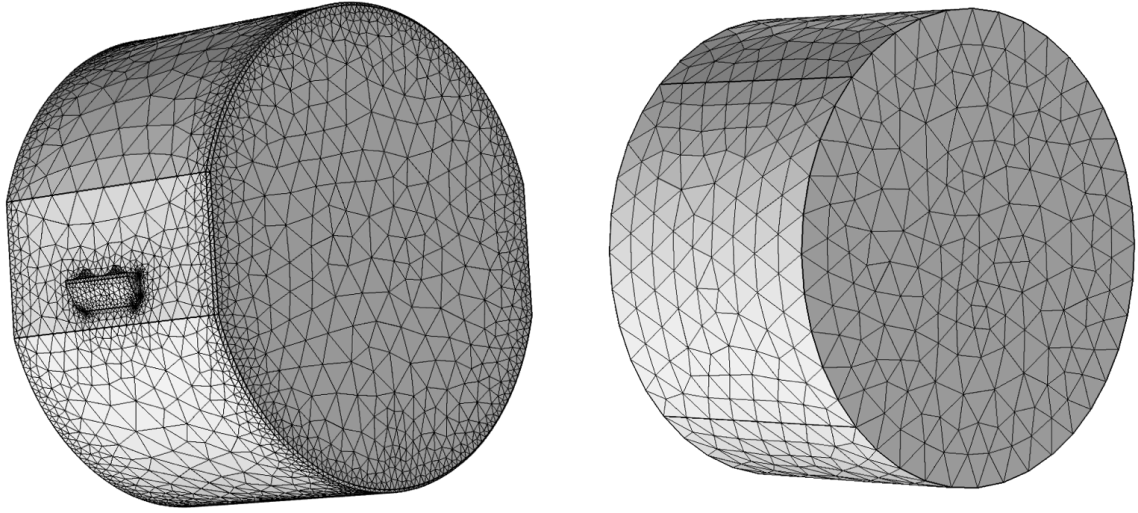
FIGURE 5.5. 3D model of the Advanced LIGO ETM and an equivalent right circular cylinder used for COMSOL simulation.

Parameter	Thickness [mm]	Diameter [mm]	Mass [kg]
aLIGO ETM	199.85	340	39.618
Ideal Cylinder	200	340	40.003

TABLE 5.1. Dimensions of the Advanced LIGO ETM and an equivalent ideal cylinder used for COMSOL simulation

that has a resonance frequency of 1 Hz when all displacements, for this study, are at frequencies far above the resonance (10 Hz and above). The dimensions and the mass of the test mass and the ideal cylinder are extracted from the 3D model and are listed in Table 5.1. Additionally, the physical parameters of the material (fused silica) that the test masses are composed of are listed in Table 5.2.

Quantity	Symbol	COMSOL Library	Fine Tuned
Density [kg m^{-3}]	ρ	2200	2203
Young's modulus [Pa]	E	70×10^9	72.6×10^9
Poisson Ratio	ν	0.17	0.1631

TABLE 5.2. Physical Parameters of the aLIGO ETM and an equivalent cylinder used for COMSOL simulation

5.4.2. Eigenfrequencies and Eigenmodes

Eigenfrequencies are set of frequencies at which the object is prone to vibrate and the corresponding shapes of the vibrational deformations are called the eigenmode shapes. The eigenfrequencies and thus the eigenmodes depend on the physical properties of the material and the also the shape of the test mass. In order to estimate the eigenfrequencies of the Advanced LIGO test mass, finite element analysis was performed with the parameters of the test mass material (fused silica) as found in the COMSOL material library. These parameters were later fine tuned such that the eigenfrequencies of the test mass from the COMSOL simulation match the measured eigenfrequencies of the test mass. The parameters from the COMSOL library and the fine-tuned parameters used for all of the studies reported here are listed in Table. 5.2. The eigenfrequencies of the lower-order *butterfly* and *drumhead* modes calculated using COMSOL using the parameters described above are listed in Table 5.3.

There are a number of higher order modes (see Table 5.4) but we will try to qualitatively understand the sensed displacement due to bulk elastic deformation in terms of the two lowest frequency modes, the *butterfly* and the *drumhead* mode. Later, we will show that the contributions from the higher order modes are important as well

Mode	COMSOL Library	Fine Tuned	
	Advanced LIGO ETM	Advanced LIGO ETM	Cylinder
Butterfly	5826	5946	5969
Drumhead	8028	8153	8109

TABLE 5.3. Eigenfrequencies of the lower order *drumhead* and the *butterfly* mode for Advanced LIGO ETM (for two different physical parameters from Table 5.2) and a cylinder.

and thus the best approach is to use the cumulative contributions from all possible modes.

In order to reduce the effect of the *drumhead* mode, the Pcal beams can be placed at the nodal circle of this mode, the position at which Pcal forces produce the least excitation, of the *drumhead* mode. This increases the deformation due to *butterfly* mode but for a perfectly centered interferometer beam the effect of the *butterfly* mode integrates out to zero for an ideal cylinder because of symmetry. This is not the case for the Advanced LIGO test masses because of the flats on the sides, which introduces asymmetry, but is still minimal at frequencies below 5 kHz for optimally located Pcal beams.

Additionally, one can notice from Table 5.4 that there are two *butterfly* mode eigenfrequencies for the Advanced LIGO ETM, shown in Fig. 5.6. The lack of azimuthal symmetry due to the flats and the ears attached to them creates two butterfly modes, unlike only one in the case of a symmetric cylinder.

| Advanced LIGO ETM | | Cylinder |
COMSOL	Measured	COMSOL
5946	5948	5969
6051	6052	
8153	8156	8109
8262		8252
8312	8312	
9097	9099	9198
9333	9330	
9418		9409
9827	9827	9826
9879	9878	

TABLE 5.4. List of eigenfrequencies between 5 kHz and 10 kHz for the Advanced LIGO ETM as determined using COMSOL (first column) and measured using the interferometer OMC DCPD signal (second column) [85, 86]. Corresponding eigenfrequencies of a perfect cylinder obtained from COMSOL simulation are listed in the third column.
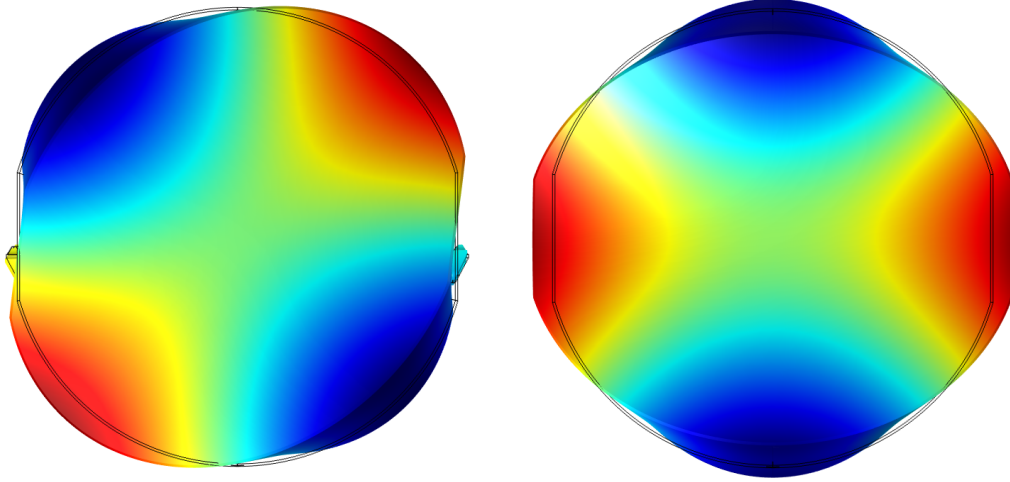
FIGURE 5.6. The two lowest order butterfly modes of the Advanced LIGO test masses. The first one is at 5946 Hz and the second at 6051 Hz.

5.4.3. Nodal Circle of the Drumhead Mode

As discussed earlier, placing the Pcal beams at the nodal circle of the *drumhead* mode minimizes the effect of elastic deformation due to that mode. In order to determine the nodal circle we use the mode shape, shown in Fig 5.7, generated using COMSOL. We determine the *least displacement* along the radius of the cylinder as a function of angle and consider angles at every 0.5 degrees. Here *least displacement* refers to the smallest absolute displacement in the direction (z-direction) to which the interferometer is sensitive to length variation.

As shown in Fig. 5.8, the ideal cylinder has a circular nodal circle at a distance of 108.9 mm from the center. The nodal circle of the Advanced LIGO test mass is elliptical in shape with a larger radius along vertical axis and smaller along horizontal axis due to the lack of symmetry. The nodal circle crosses the vertical axis at ±110.9 mm. In the case where the effect of other modes, most importantly the *butterfly* mode, is negligible, the nodal circle is the optimal position for the Pcal beams. But
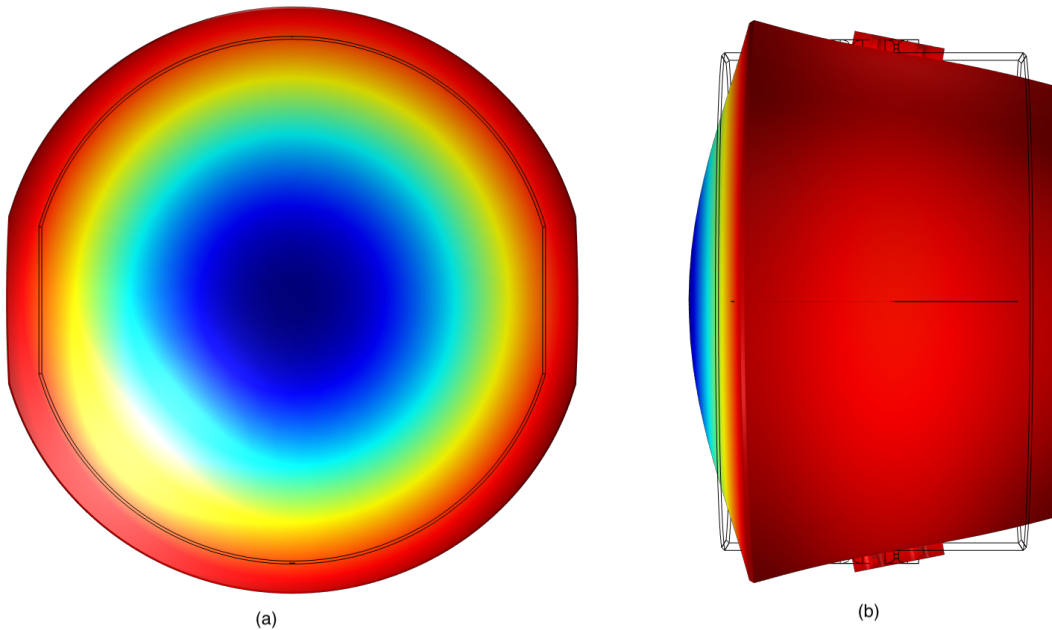
FIGURE 5.7. The shape of the *drumhead* mode of the Advanced LIGO test mass, at a frequency of 8153 Hz. (a) shows the face of the optic where interferometer beam and Pcal beams are reflected off and (b) shows the z-displacement of the same face of the optic as a result of the *drumhead* mode excitation.

in order to account for the effect of other modes, we define the optimal positions as Pcal beam positions at which the value of $\mathcal{G}_{(a,b)}(f)$ in Eq. 5.4 is closest to 1 at frequencies between 10 Hz and 5 kHz. Using this definition, the optimal positions of the Pcal beams for the Advanced LIGO test mass are determined to be at $(0, \pm 111.6$ mm) on the face of the test mass.

5.4.4. Effect of deformation as a function of Pcal & IFO beam positions

The deviation from the rigid body motion is estimated, in COMSOL, by measuring the total surface displacement of the test mass weighted by the main interferometer beam gaussian profile and comparing it to the rigid body motion of the test mass. The total displacement, x_{total} (in Eq. 5.4), which includes the rigid-body motion and the displacement due to the deformation, is the overlap of the surface

125
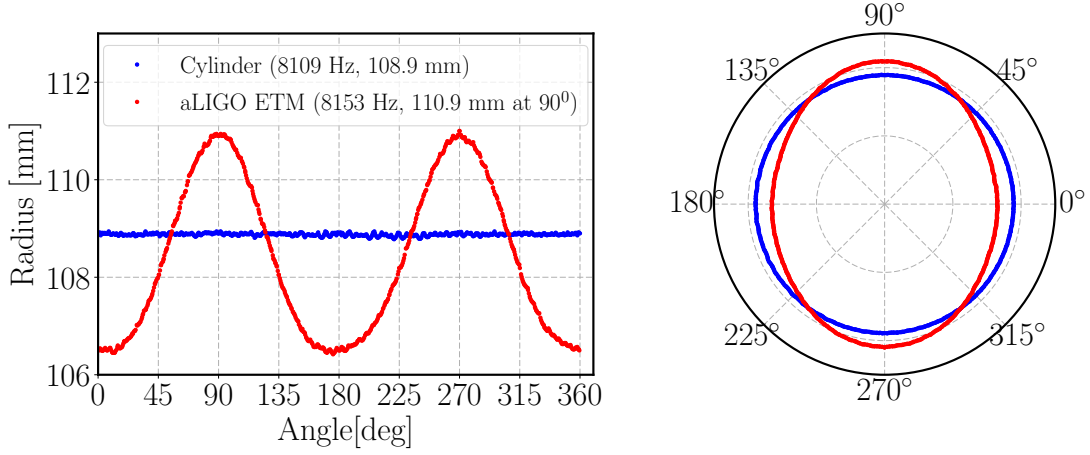
FIGURE 5.8. Nodal radius of the *drumhead* mode of a perfect cylinder (same diameter and thickness as Advanced LIGO ETM) and an actual aLIGO ETM. The cylinder has a circular nodal radius at 108.9 mm. The Advanced LIGO ETM has an elliptical nodal radius because of the flats on two sides of the optic. The nodal radius on y-axis, where the Pcal beams are placed, is at approx 110.9 mm.

displacement over the Gaussian interferometer beam and is given by [53, 59, 83]

$$x_{\text{total}}(f) = k_I \int_\Omega w(x, y; f) \cdot I(x, y, z) dx dy \tag{5.5}$$

where k_I is the normalization constant such that $k_I \int_\Omega I(x, y, z) dx dy = 1$, "w" is the actual displacement of the test mass surface in the z direction and $I(x, y, z)$ is the profile of the interferometer beam given by:

$$I(x, y, z) = \exp\left(-2\frac{(x - x_0)^2 + (y - y_0)^2}{\omega(z)^2}\right) \tag{5.6}$$

Here $[x_0, y_0]$ are the coordinates of the interferometer beam center. They are [0,0] for a centered interferometer beam. $\omega(z)$ describes the interferometer beam spot size given by

$$\omega(z) = r_{ifo} \times \sqrt{1 + \frac{z}{z_R}} \tag{5.7}$$

126

where r_{ifo} is the average interferometer beam radius at the test mass, z_R is called the Rayleigh range and accounts for the reduction of beam in the z-direction. Since $z <<< z_R$, the quantity inside the square root is approximately equal to 1 and for practical purpose, $\omega(z) \approx r_{ifo}$ is a valid approximation.

To estimate the rigid-motion of the test mass, $\mathrm{x_{rigid}}$ (in Eq. 5.4), center-of-mass motion is estimated in COMSOL and the effect of rotation is added by calculating it analytically.

Using the technique described above we estimated the deviation of test mass displacement from a rigid body motion, given by Eq. 5.4, for configurations at which the interferometer beam is centered and the Pcal beam positions are varied. For this study, we moved the Pcal beams away and towards the center of the test mass surface, from their optimal positions, along the vertical axis (y-axis). Given that the Pcal beam positions are $(0,\pm y)$, we define Pcal beam displacement, $\Delta y = y - 111.6$ where $+\Delta y$ denotes that the Pcal beams have moved away from the center and $-\Delta y$ denotes that the Pcal beams have moved towards the center from their optimal positions.

The result of such simulations is shown in Fig. 5.9 for various Pcal beam positions. The results show that for optimally located Pcal beams the deviation is less than 1% below 4 kHz but reaches 3% at 5 kHz. However, for Pcal beams that are even a few mm away from their optimal positions, the deviation from the rigid body motion increases dramatically at frequencies above 2 kHz. The results also show that the estimation of displacement is underestimated for Pcal beams that have moved towards the center and is overestimated for Pcal beams displaced away from the center. This is consistent with the shape of the *drumhead* mode as shown Fig. 5.7(b) and its resultant z-displacement. However, one can also notice that the plots start to curve
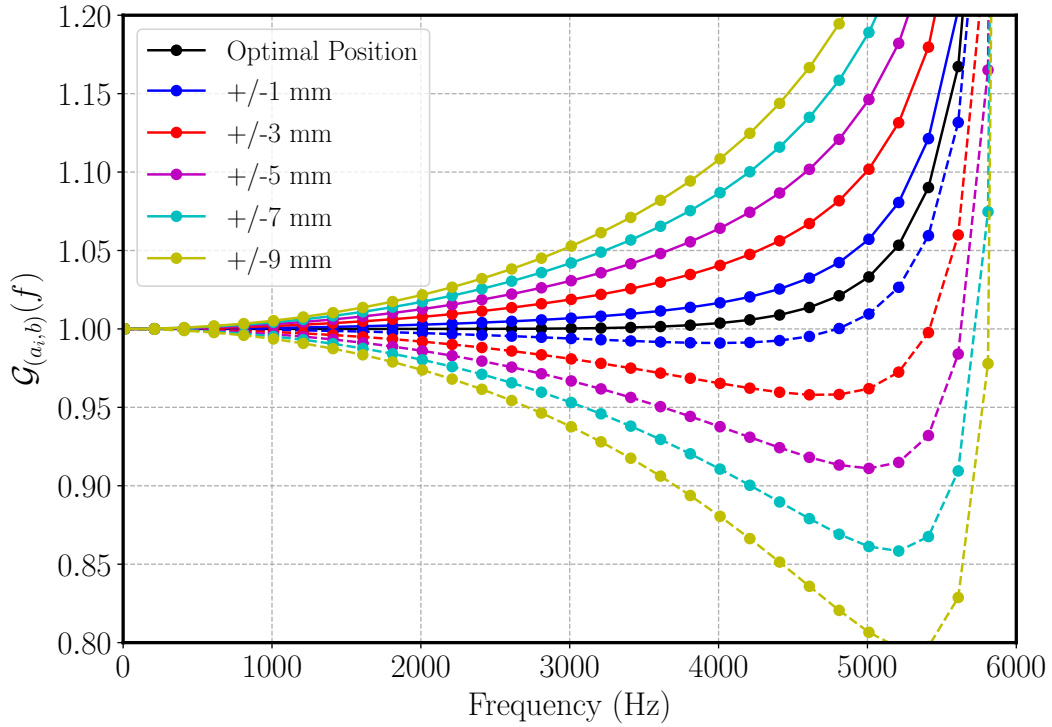
FIGURE 5.9. Deviations from the rigid body motion of the test mass as a function of Pcal beam positions. Results are estimated using finite element analysis, COMSOL Multiphysics, for Pcal beams displaced symmetrically away from (solid lines) and toward (dashed lines) the center of the test mass from their ideal locations.

back towards the positive y-axis at higher frequencies for all Pcal beam configurations. This is because the frequency approaches the resonance of the butterfly mode and the butterfly mode dominates.

A similar study for a perfect cylinder is shown in Fig. 5.10. The results show that the impact of the lower order frequency butterfly mode ($f = 5969$ Hz) indeed averages to zero for an ideal symmetric cylinder. However, the optimal locations are not on the nodal circle of the *drumhead* mode. This is because the higher order modes impact the motion at lower frequencies as well. The optimal radius for an ideal cylinder, based on FEA results, is ≈ 113 mm.
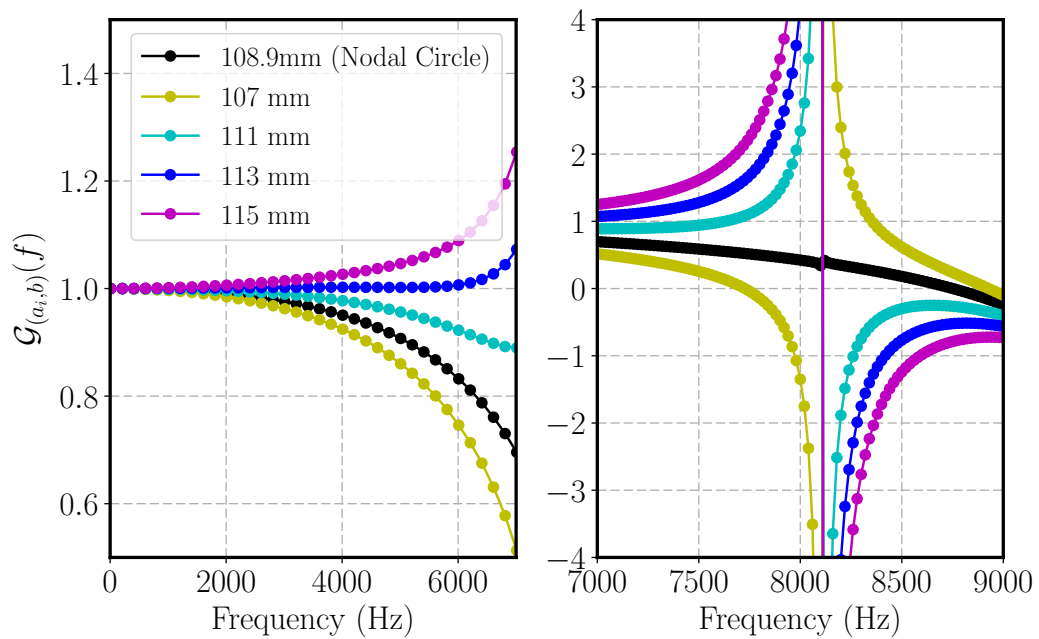
FIGURE 5.10. Deviations from rigid body motion for Pcal beam offsets symmetrically from their optimal locations (113 mm) for an ideal cylinder estimated using finite element analysis.
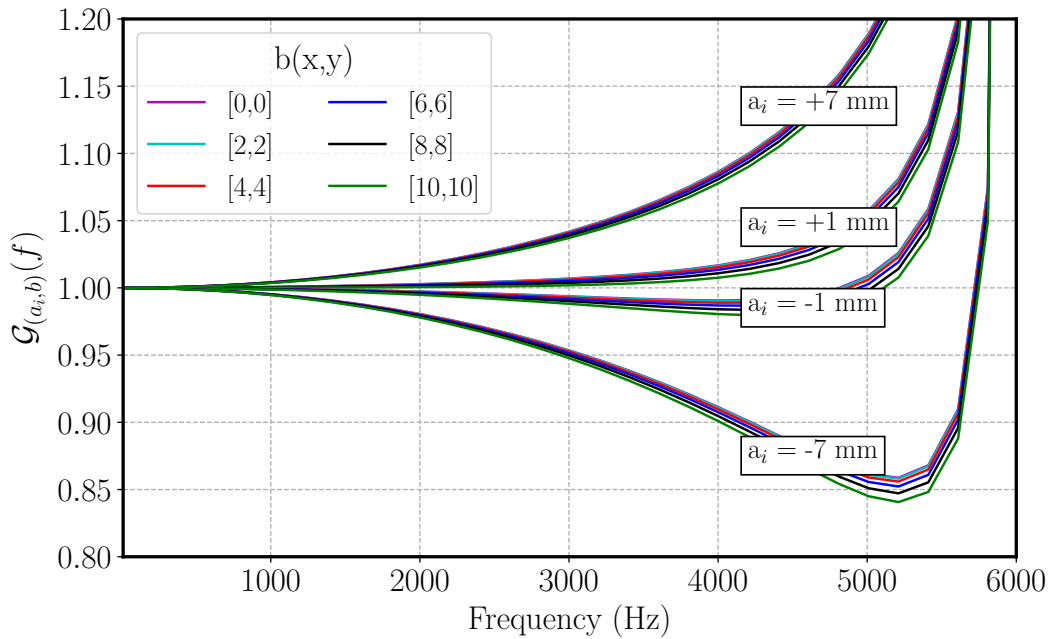
FIGURE 5.11. Deviations from rigid body motion as a function of Pcal and interferometer beam positions. The "a_i" denotes the Pcal beam offset and the legend denotes the x and y-coordinates of the interferometer beam position in mm where [0,0] is the center of the test mass surface.

In order to study the impact of interferometer beam position offset, the longitudinal displacement of the test mass as sensed by the interferometer beam was calculated for various beam position offset from the center for each set of Pcal beam position offsets. The results are shown in Fig. 5.11, where "a_i" denotes the position of Pcal beam offset and the coordinates in the legend denote the center of the interferometer beam where [0,0] is the center of test mass face. The results show that the deviations are smaller for interferometer beam position offsets than they are for the Pcal beam position offset of the same amplitude. However, even for an optimized Pcal beam locations, the deviations are as large as 2% at frequencies between 4 and 5 kHz for an interferometer beam that is as far as 1 cm from its optimal position.
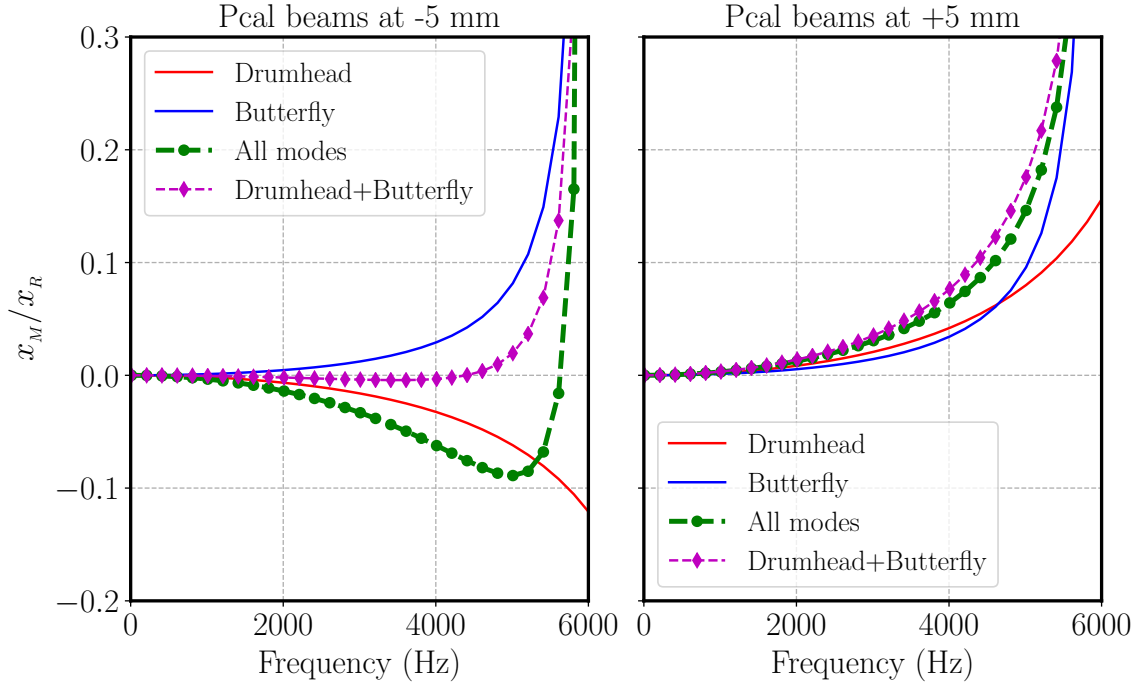
FIGURE 5.12. Displacement of the test mass due to *butterfly* and *drumhead* modes as sensed by a centered Gaussian interferometer beam from are plotted in solid lines. The curve with diamond is the sum of displacement due to the *butterfly* and *drumhead* mode and with circle is the overall sensed displacement due to bulk elastic deformation.

5.4.5. Single Mode Analysis

In order to understand the contribution of each normal mode of the test mass, simulations were run such that impact of a single mode was captured in each simulation. The Pcal beams were placed at two configuration, +5 mm and -5 mm (same sign convention as used in analysis before) from their optimal positions. The results are plotted in Fig. 5.12 and the result shows that the overall sensed displacement is different from the sum of the displacement due to *butterfly* and *drumhead* mode. In order to check the contribution of the higher order modes we ran simulations for single-mode contributions for Pcal beam configuration at -5 mm for the modes as high as 15 kHz. The result is plotted in Fig. 5.13. The result
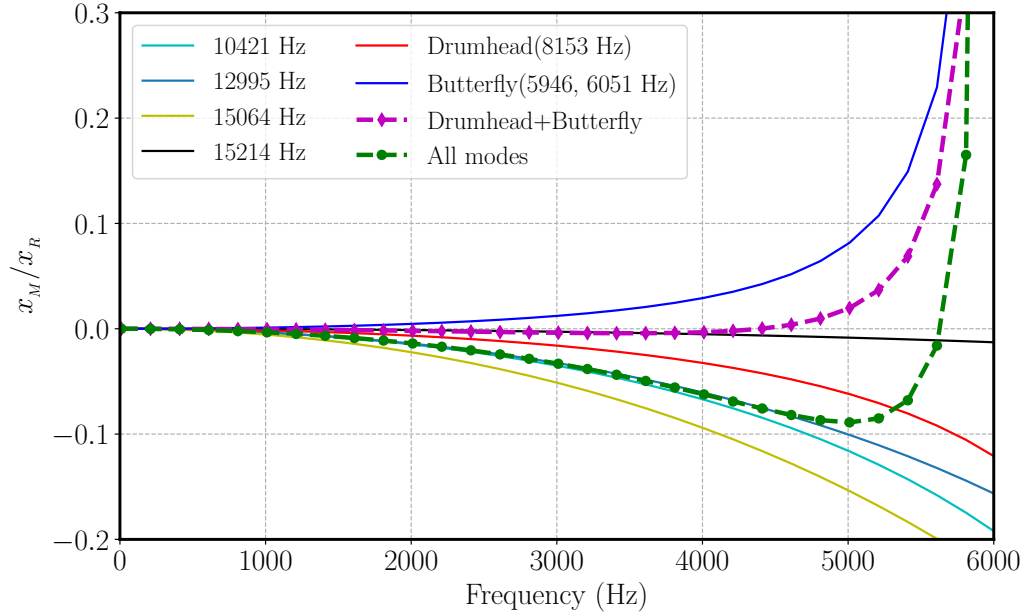
FIGURE 5.13. Contribution of normal modes to the overall sensed displacement of the test mass.

indicates that the contributions from some of these higher order modes are indeed much larger than expected. A further study is required for more detail understanding.

5.5. Bulk Elastic Deformation: Measurement

To assess the impact of the *bulk elastic deformation* described above and to compare experimental results with the predictions of finite element analysis (COMSOL Multiphysics), a series of measurements were made using the two LIGO interferometers during Advanced LIGO's second observing run. The Pcal beams were moved to desired positions on the test mass surface with the aid of the Pcal beam localization system described in detail in Chapter 3. Three configurations, first at optimal positions (111.6 mm above and below the center of the test mass surface), second where both beams were offset 14 mm away from the center(+14 mm) and
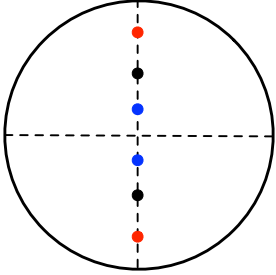
Config.	Pcal Beam Position			Beam Config.
	Beam	Target (mm)	Actual (mm)	
OP	Upper	[0, 111.6]	[0.8, 112.2]	
	Lower	[0,-111.6]	[-0.8, -111.8]	
P14	Upper	[0, 127.6]	[1.2, 126.1]	
	Lower	[0, -127.6]	[-0.5, -125.7]	
M8	Upper	[0, 103.6]	[2.5, 103.2]	
	Lower	[0, -103.6]	[-1.3, -103.0]	

TABLE 5.5. Positions of Pcal beams on the surface of the test mass for three different beam configurations. The illustration on the right shows optimal positions (OP) in black, P14 in red and M8 in blue.

the third where both beams were offset 8 mm towards the center(-8 mm) from the optimal positions, were used. These configurations are referred to as OP, P14 and M8 from here onward and are illustrated in Table 5.5.

The beams were moved symmetrically to avoid unwanted rotation of the test mass. After the beams were placed approximately at the desired positions, the Pcal system was used to inject sinusoidal excitations at frequencies between 1000 Hz and 5000 Hz. Since the Pcal laser power required to produce a given displacement of the test mass increases as the square of the frequency at which the displacement is made, for these "high frequency" excitations, a single excitation was introduced at one given time using all available laser power. The excitations were left on for at least 24 hours and sometimes even for days, depending on the duty cycle of the interferometer. An automated script was used to change the frequency of the excitation if and when the interferometer went out of lock and enough data had been collected at that frequency.

For the times when the excitation lines were on and the interferometer was in lock, data from relevant channels were demodulated at the excitation frequency.

During demodulation, the integration time was set to 10 minutes for frequencies below 2500 Hz, 30 minutes for frequencies between 2500 Hz and 4000 Hz and and one hour for frequencies above 4000 Hz to achieve an appreciable SNR for each data point. The estimate of the displacement from the interferometer strain channel was compared with the displacement estimated using the Pcal read-back signals. The displacement recorded by the interferometer strain channel (x_{GDS}) includes the impact of *bulk elastic deformation* while the displacement estimated from the Pcal read-back channel (x_T) assumes the test mass is a rigid body. In order to account for temporal variations in interferometer configurations between different excitations, the displacement at each frequency were normalized to a $\sim$1 kHz excitation running at all times.

The interferometer strain channel uses an approximation that the interferometer response to length variations is described by a single pole. In order to account for the error due to this approximation, a correction factor (residual from plot shown in Fig. 5.3) is applied at each excitation frequency. Thus, the discrepancy between the observed displacement and the rigid body motion, $\mathcal{G}_{(a_i,b)}(f)_{meas}$, can be written as

$$\mathcal{G}_{(a_i,b)}(f)_{meas} = \frac{x_{GDS}(f)}{x_T(f)} \times \frac{x_T(f_0)}{x_{GDS}(f_0)} \times Q_C(f) \tag{5.8}$$

where f is the measurement frequency, f_0 is the frequency of the excitation used for normalization and $Q_C(f)$ is the correction factor that accounts for errors due to the single pole approximation of the interferometer response.

Fig. 5.14 shows the results from simulations and measurements for three different Pcal beam positions, P0, P14 and M8. The impact of the bulk elastic deformation measured using the interferometer agrees reasonably well with the results from the finite element analysis for all three beam configurations.

134
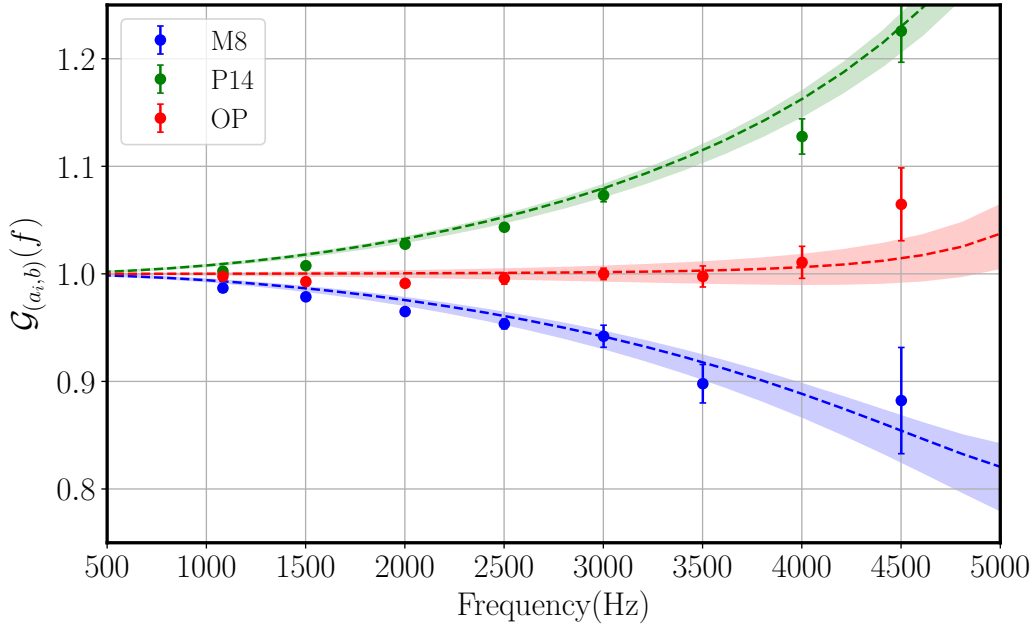
FIGURE 5.14. Deviations from the rigid body motion of the test mass as a function of Pcal beam positions. The data plotted in crosses with dashed lines are the results of COMSOL simulations for the measured Pcal beam positions and for perfectly centered interferometer beam. The shaded regions are for interferometer beam centering offsets as large as ± 10 mm. The data plotted in circles with error bars are the measured deviations, $\mathcal{G}_{(a_i,b)}(f)_{meas}$, estimated using Eq. 5.8.

Similar measurements were later made using the Livingston interferometer (L1) and the Hanford interferometer (H1), but only for the Pcal beam positions close to optimal locations and the results are shown in Fig. 5.15. The results indicates that the data agrees reasonably well with the model at most frequencies, including close to the resonance, but between 4.5 and 5.5 kHz there exists some deviations from the result estimated using finite element analysis and the data.

By looking at the interferometer response at some of these frequencies at times when the excitation was present and comparing it to the times when the excitations were absent indicates that these are produced due to calibration forces and are not inherent to the interferometer. Additional studies will be required to understand
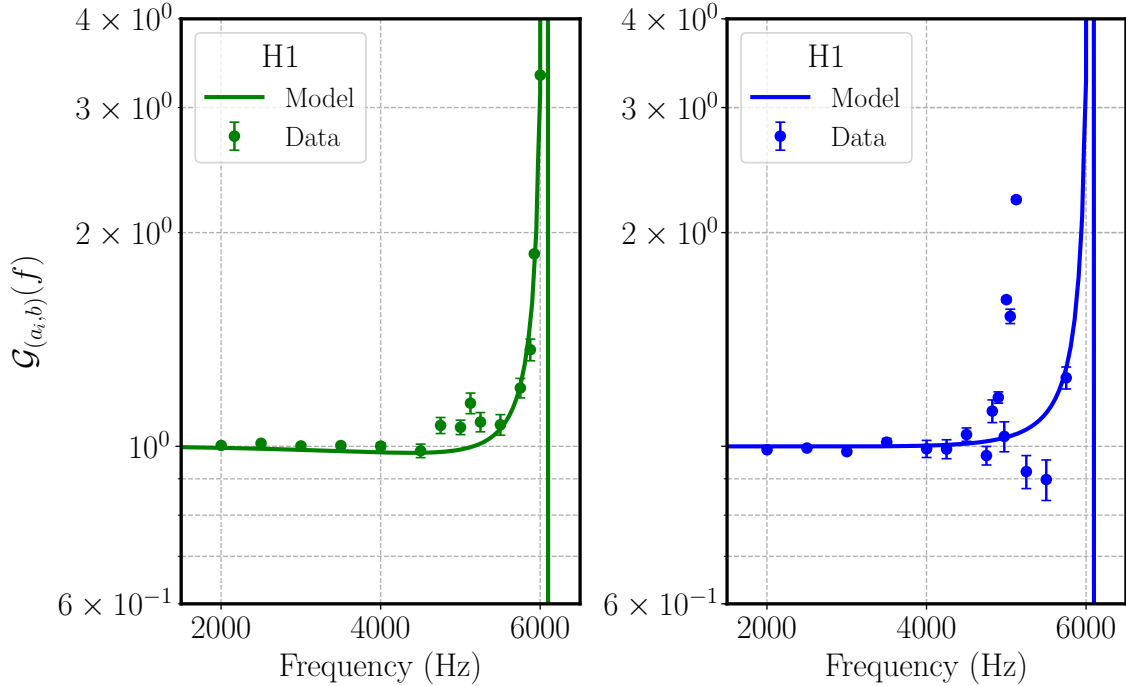
FIGURE 5.15. Plot showing the deviations from the rigid body motion of the test mass. Both Hanford (H1) and Livingston (L1) data shows feature between 4.5 kHz and 5.5 kHz, where the measurement results deviate from the modeled result.

these features. One can avoid exciting these features by restricting the calibration lines up to 4.5 kHz and extrapolating the calibration to 5 kHz.

5.6. Application to interferometer calibration

We have shown that the calibration forces excite the natural vibrational modes of the test mass causing it to deviate from the rigid body motion, especially when the measurement (excitation) frequency reaches the resonant frequency of these modes. So when using calibration forces, these effects need to be accounted for to achieve a better calibration of the interferometer data.

During Advanced LIGO's first and second observing runs, these deviations of the interferometer response from rigid body motion were simply folded into the calibration

uncertainty as systematic error. This method might be sufficient if the Pcal and the interferometer beams are optimally located and the calibration uncertainty is deemed satisfactory at a level of 10%. However, we have shown that the deviation increases significantly if Pcal and/or interferometer beam are not optimally located. More importantly, if and when there is a detection of gravitational-wave signals with signal content at higher frequencies, the calibration requirements at these frequencies will become stringent. So in order to meet these requirements, correction to the deviation due to bulk elastic deformation is essential.

For frequencies above 1 kHz, where the response function is dominated by the sensing function and the open loop gain is negligible, the sensing function measured using Pcal excitations can be approximated using Eq. 4.3. However, in order to account for the effect of bulk elastic deformation, the sensing function needs to be written as

$$C'(f)_{meas} \approx \frac{d_{err}(f)}{x_{\mathrm{T}}(f)} \times \frac{1}{\mathcal{G}_{(a_i,b)}(f)} \tag{5.9}$$

where $\mathcal{G}_{a_i,b}(f)$ is estimated from COMSOL simulation, using Eq. 5.4, for a given Pcal and interferometer beam positions. This shows that the ability to determine the location of the Pcal and interferometer beams will directly influence the calibration accuracy in this regime.

The sensing function shown in Fig. 4.2 is recalculated, correcting for the bulk elastic deformation using Eq. 5.9, and plotted as shown in Fig. 5.16. The improvement below 4 kHz is minimal with a few % improvement in calibration error between 4 and 5 kHz.
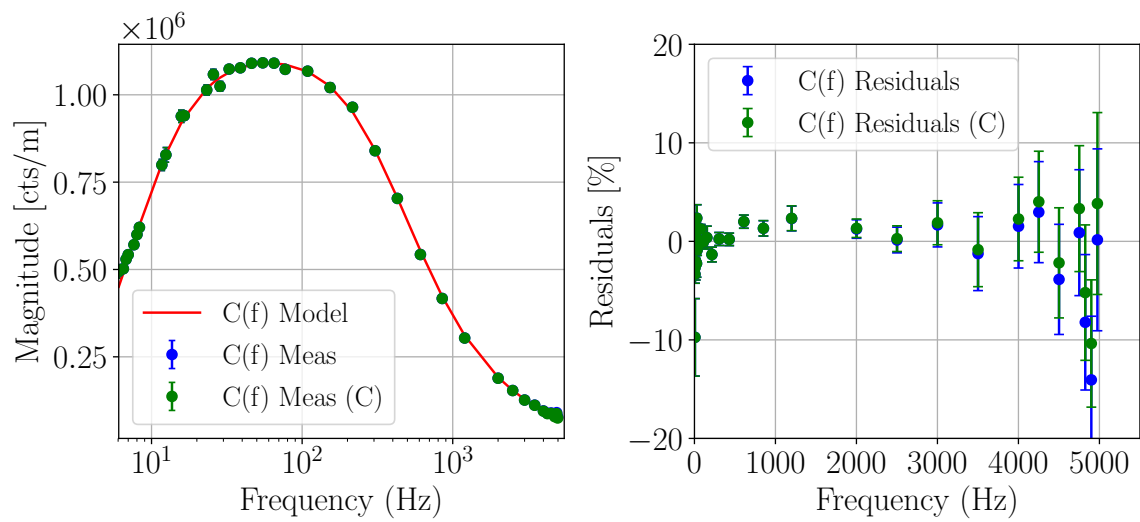
FIGURE 5.16. Magnitude of the Sensing Function showing the comparison between modeled and measured sensing function for H1 detector. The blue data shows results where the bulk elastic deformation has not been corrected for. The green data, after applying the corrections due to bulk elastic deformation, shows decrease in the residuals and thus the uncertainty.

CHAPTER 6

DISCUSSION AND CONCLUSIONS

In light of the gravitational wave detections during the past few years and their enormous astrophysical implications, accurate calibration of gravitational wave detectors has become even more important. This dissertation is an attempt to describe the aspects of astrophysics that rely on accurate calibration and the methods employed within the LIGO project to achieve the calibration accuracy required to maximize the astrophysical and cosmological information extracted from these signals.

The first direct detection of gravitational waves was in itself a great scientific achievement. But the gravitational-wave community has always been motivated by the astrophysics and precision cosmology studies that are possible with these detected signals. The gravitational waves provide information about the physical parameters [87] and the dynamics of the sources [36] that produce them as well as the environment in which these sources reside and evolve [88].

Since gravitational wave signals are reconstructed from interferometer output signals registered on photodetectors as power fluctuations using a calibration pipeline [89], the astrophysical information that is contained within the signals is affected by the calibration. Better calibration accuracy ensures that low SNR signals that arrive at the detectors are not missed, and for detected signals it ensures that the parameters of the sources are accurately determined. In 2009, Lee Lindblom estimated that calibration accuracy in the order of 5% in magnitude and 5 deg in phase is required to optimize signal detection efficiency and an order of magnitude better calibration accuracy, 0.5%, is required to optimally extract astrophysical parameters from these signals [31].

For the detections made during the Advanced LIGO's first and second observing runs, improved calibration accuracy resulted in more constrained values for source parameters that include progenitor masses, chirp mass, spin, and luminosity distance, among others [90].

As suggested and described for the first time in [91] and many other papers there after, the luminosity distance measured using the gravitational waves, along with the red-shift determined from an electromagnetic (EM) counterpart signals enables an independent measurement of the Hubble parameter. This technique has already been used to determine the Hubble parameter from the gravitational wave signal generated by a pair of binary neutron stars merger, GW170817, with an EM counterpart with an uncertainty of 15% [42]. Using such EM-bright gravitational wave sources referred to as "standard sirens", Hsin-Yu Chen, et al. [46] have predicted that this method will enable measurement of the Hubble parameter with an uncertainty of 4% with approximately twenty such events. It will require approximately 100 events to reach the level of 1%.

In cases where an EM counterpart is absent, as in the case of binary black hole mergers, for sources that are well-localized using a network of gravitational wave detectors, red-shift information from galaxy catalogs can be utilized to make a statistical measurement of the Hubble parameter [92]. Gravitational wave signals from the binary black hole merger GW170814, which had better source localization due to the involvement of three detectors – two LIGO detectors and a Virgo detector – have been used in conjunction with the galaxy catalog from the Dark Energy Survey (DES) to make such a measurement of the Hubble parameter. The study estimates that using GW170814-like events where EM counterpart is absent, referred to as

"dark standard sirens", the Hubble parameter measurement with an uncertainty of approximately 4.5% can be achieved with 100 such events [93].

Since the luminosity distance of the gravitational wave sources used in these studies is directly dependent on the amplitude of the gravitational wave signals, calibration of the gravitational wave data with an accuracy of 1% or better will be required when enough signals have been detected to constrain the Hubble parameter with an uncertainty close to 1%. With improved detector sensitivity, involvement of multiple detectors, and updated rate estimates [94], measurement of the Hubble parameter with an uncertainty of 4% can be achieved within the next few years and 1% within a decade [46].

This dissertation discusses the design, implementation and characterization of an upgraded radiation-pressure-based calibration tool called the Photon calibrator (Pcal) that is used as the primary calibration reference for the Advanced LIGO detectors. During the Advanced LIGO first and second observing runs, using Pcal systems, we were able to generate calibrated displacement fiducials with an uncertainty of 0.75 %. The main contributor to this uncertainty (0.51%) was the calibration of power sensors used to monitor the Pcal laser power. The calibration was performed at National Institute of Standards and Technology (NIST) and is traceable to SI units. A robust method to transfer calibration from a NIST-calibrated power sensor to the power sensors in the Pcal modules at the end station that monitor the laser power at all times has been established without introducing significant uncertainty. This procedure involves series of responsivity ratio measurements between different power sensors. Rotation of the test mass due to misaligned Pcal beam spots and the allocation of optical losses inside the vacuum enclosure were other significant sources

of uncertainty during the first and second observing runs. These have been improved since then.

Frequency dependent calibration of the LIGO interferometers is obtained by measuring the response function, $R(f)$, which relates the strain sensed by the interferometer, $h(f)$, to the error signal of the differential length control servo, $d_{err}(f)$, recorded by the output photodetector as: $h(f) = (1/L)R(f)d_{err}(f)$, where $R(f)$ is given by

$$R(f) = \frac{1 + A(f)D(f)C(f)}{C(f)} = \frac{1 + G(f)}{C(f)} \tag{6.1}$$

Based on the absolute displacement calibration achieved using the Pcal systems, series of swept sine measurements are made to determine the actuation function $A(f)$ and sensing function $C(f)$ and thus obtain the response function, $R(f)$, of the interferometer. The discrepancy between the measurements and the models of these actuation and sensing function provides the measure of uncertainty in the response function. The transfer function of the digital filters, $D(f)$, is known to a negligible uncertainty.

Calibration lines were placed at different frequencies to determine calibration factors that were used to track and compensate temporal changes in the interferometer response. The frequency independent scalar factors were applied in low latency (on order of tens of seconds) within the calibration pipeline during both first and second observing runs providing overall calibration accuracy in order of 10% in magnitude and 10 deg in phase. Corrections of known systematic error were applied later during second observing run to produce an offline calibrated data-stream referred to as 'C01' with 1-σ calibration uncertainty of 6.1% in magnitude and 2.2 deg in phase for H1 and 4.8% in magnitude and 2.2 deg in phase for L1 at frequencies between 20 Hz and 2048 Hz [95]. Frequency dependent lowest order "cavity-pole" frequency fluctuations

142
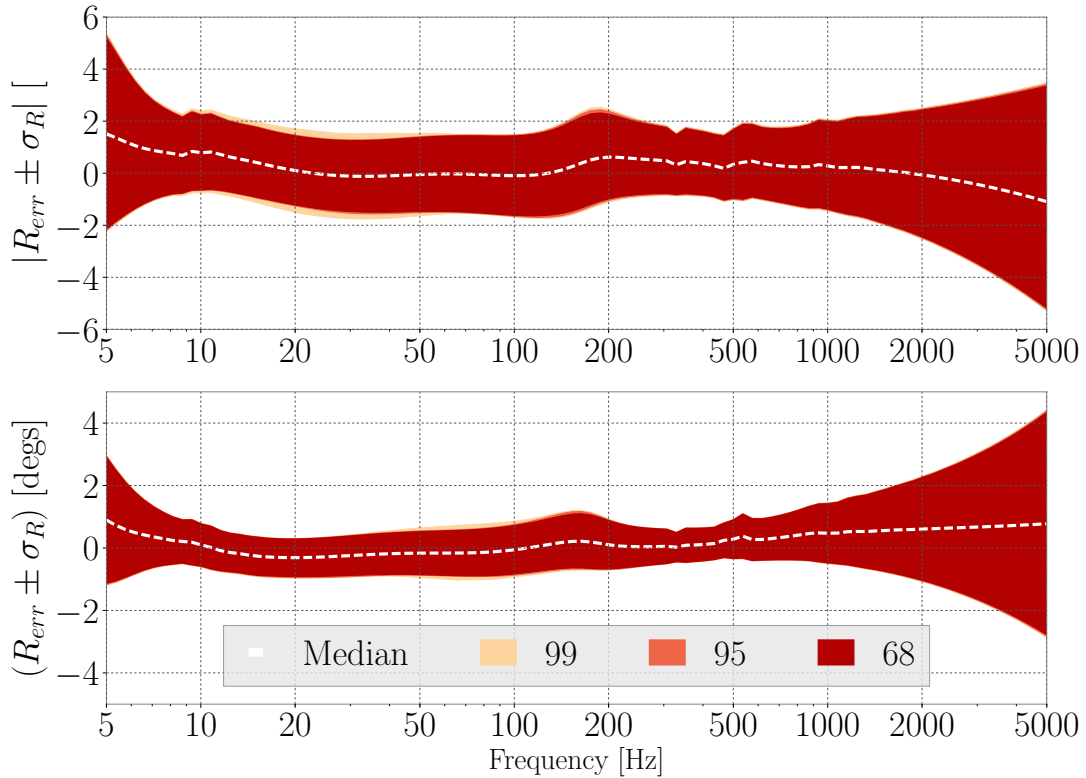
FIGURE 6.1. Frequency dependent systematic error and uncertainty in the response function of LIGO H1 detector during the entire second observing run. The central dashed line represents the estimated systematic error from the modeled interferometer response and the color band represents the uncertainty about the median.

was left as a systematic error during first observing run and corrected offline (in high latency) during the second observing run, producing data referred to as 'C02' with improved 1-σ calibration uncertainty of 2.6% in magnitude and 2.4 deg in phase for H1 and 3.9% in magnitude and 2.2 deg in phase for L1 across the same frequency band as above [95]. This is a significant improvement from its predecessor, Enhanced LIGO, where calibration uncertainty was at the level of 10-15% in magnitude and 5 deg in phase [96]. For illustration, Fig. 6.1 shows the overall frequency dependent calibration uncertainty for H1 detector during the entire second observing run corrected for all time-varying calibration parameters.

Further improvement in detector calibration will require improvement in absolute displacement calibration accuracy, reducing the systematic error in the interferometer response function, and reduction of uncertainty in the measurement of actuation and sensing functions. There have been numerous small, yet crucial, improvements towards better accuracy of the absolute displacement calibration for the planned third observing run (O3) and beyond.

Within LIGO, the power measurement standards have been reconfigured to increase the power sensor stability and decrease laser speckle. This increases the reliability of the power sensors and reduces the uncertainty in photodetector responsivity measurements. The accuracy of the placement of the Pcal beams on the test mass surface has been improved to within ± 2 mm using in-chamber targets mounted to the test mass suspension frame during vents. The interferometer beam is expected to be centered on the test mass within ± 5 mm during the O3 run. These improvements will reduce the uncertainty due to rotation of the test mass by approximately a factor of four ($0.40\% \rightarrow 0.10\%$) for O3. Similarly, uncertainty arising from the optical losses within the Pcal system has been improved by making in-vacuum measurements of power and apportioning the losses between the input (incident) and output (reflected) sides. The associated uncertainty has thus been reduced by about a factor of four as well ($0.37\% \rightarrow\sim 0.10\%$).

A collaborative effort between NIST and the LIGO Scientific Collaboration has been initiated to get better calibration accuracy on power sensor measurements. For the most recent calibration measurement of the updated Pcal Gold Standard, NIST provided an improved uncertainty of 0.31% (1-σ) compared to 0.44% in the past. This is a significant step in our goal of improving the absolute displacement calibration accuracy using Pcal.

144

Parameter	Relative Uncertainty (Expected O3)
NIST -> GS $[\rho_{GS}]$	0.31 %
WS/GS $[\alpha_{WG}]$	0.03 %
Rx/WS $[\alpha'_{RW}]$	0.05 %
Optical efficiency $[\mathcal{E}_T]$	0.10 %
Angle of incidence $[\cos\theta]$	0.07 %
Mass of test mass $[M]$	0.005 %
Rotation $[(\vec{a} \cdot \vec{b})M/I]$	0.10 %
Overall	**0.35 %**

TABLE 6.1. Expected Pcal uncertainty for planned third LIGO observing run (O3).

With these improvements, as shown in Table 6.1, a calibration accuracy of $\sim$ 0.35% could be achieved for the absolute displacement introduced using the Pcal system for the third LIGO observing run. If realized as expected, this would be an improvement in excess of a factor of two ($0.75\% \rightarrow 0.35\%$) compared to the Advanced LIGO first and second observing runs.

Reducing frequency-dependent systematic errors will require better understanding of the interferometer to accurately model its response. One such improvement is the implementation of the full response of the interferometer to length variations instead of the single-pole approximation that is currently being used. Additionally, compensation for the impact of analog electronics and digital systems used within LIGO controls and data acquisition system should be carefully considered. Although it is a straight forward measurements, the sheer number of these transfer functions,

as shown in the *Calibration Subway Map* in Appendix D, makes this task challenging. Improvements in actuation and sensing function measurement uncertainty will require more measurements and thus more interferometer time. For the planned third observing run, time-varying calibration parameters, including the cavity-pole frequency, will be compensated within the front-end of the Advanced LIGO data acquisition system, thus providing the most accurate calibration in real-time.

Along with its contributions to accurate detector calibration, the Pcal systems have been used as actuators to inject simulated gravitational wave signals to understand the response of the interferometer and test the robustness and efficiency of the detection pipelines used for gravitational wave analysis [56]. Additionally, use of Pcal system as a low-noise actuator for the interferometer length control was demonstrated during Advanced LIGO's second observing run [76] and plans are underway to establish it as an alternative to electrostatic drives (ESD) for low-noise operation during the upcoming observation run.

This dissertation also explores the impact of bulk elastic deformation of the test mass in response to calibration forces, which could result in significant calibration errors at frequencies above 1 kHz. This effect was modeled using finite element analysis (FEA) simulations. The FEA results presented here are in agreement with the results from previous studies shown in [59]. However, the overall impact of the *bulk elastic deformation* is not only due to the lower order vibrational modes, the *butterfly* ($\sim$6 kHz) and the *drumhead* ($\sim$8 kHz) modes, as previously believed. This study shows that the contribution of the higher order modes, with resonant frequency as high as 15 kHz, were significant and much larger than expected. So, in order to estimate the impact of bulk elastic deformation even at frequencies well below some

146

of the resonant modes, all possible natural vibrational modes of the test mass needs to be included.

Through precise positioning of Pcal beams and using the Pcal system to drive the test mass at higher frequencies, it was shown that the modeled calibration error at these frequencies agree reasonably with the measurements, across most frequencies, while leaving some yet unexplained features between 4.5 to 5.5 kHz. As shown in Chapter 5, this understanding has provided a way to correct for the error due to bulk elastic deformation at higher frequencies and reduce calibration uncertainty at these frequencies. However, these calibration errors are a result of applying calibration forces, so alternative calibration techniques that do not rely on applying forces on the test mass such as frequency modulation based methods might be a good alternative to probe the calibration at these frequencies. This could be a topic of future study.

Accurate calibration at higher frequencies will be particularly important for the signals from binary neutron star mergers. The binary neutron star mergers are predicted to have characteristic post-merger signals at frequencies between 1 and 5 kHz. These post-merger frequency estimates are model-dependent and depend on the radius of the neutron star, thus providing an important parameter for determining the equation of state of the neutron star [79]. It is estimated that the post merger signal from a GW170817-like event would be an order of magnitude below the current Advanced LIGO sensitivity [80]. But it is likely that the post-merger signals from binary neutron stars will be detected with the next generation of gravitational wave detectors. Further improvement of the calibration in the high frequency regime will be necessary to understand these signals and decipher the information they carry.

6.1. Future Prospects

The astrophysical and cosmological implications of the multiple gravitational wave detections that have been made in the past few years and many more that will be detected in the near future are enormous. With improved detector sensitivity, the prospect of detections with an SNR of 1000 are becoming reality rather than fantasy, pushing the calibration requirement to the level of 0.1%. The direct bearing that absolute laser power calibration has on LIGO science, coupled with the expected need for improved uncertainty has stimulated a lot of interest among global metrology institutes that provide absolute laser power calibration used for the calibration of gravitational-wave detectors.

NIST is coordinating with global metrology institutes to initiate a study that would enable calibration of power standards at the 1-W level among different institutes. This is in response to the requirements of the gravitational wave community and the differences in calibration of laser power sensors (at a level of 3%) observed during one such comparative study performed more than a decade ago [67]. Additionally, NIST is expected to roll out a new type of calibration tool based on cryogenic radiometers that will provide a calibration of laser power sensors with an uncertainty of 0.1% (1-σ) within the next few years [97].

The procedure to transfer the calibration from the LIGO Gold Standard to the power sensors in Pcal systems has been shared with the Japanese GW detector, KAGRA, and propagating this process to the Virgo detector is in progress. These are steps towards the goal of standardizing the calibration of all ground-based gravitational-wave detectors to ensure that relative calibration errors among the network of detectors are minimized.

148

In conjunction with the Pcal system, a method that employs varying Newtonian gravitational fields to produce displacement of a test mass, called Newtonian calibrator (Ncal) has been demonstrated as a calibration tool in an interferometer setting in Virgo detector [98]. Variants of these Ncals are being investigated by LIGO and KAGRA [99]. Although these system will be limited to lower frequencies and a detailed estimates of its systematic and measurement uncertainties needs to be undertaken, they hold a good promise as a viable alternative absolute calibrator because of their relative simplicity and well understood physics.

The prospect of utilizing the gravitational wave signals, especially the ones from standard sirens, those with an EM counterpart, to calibrate the GW detectors has been proposed and studied. Current estimates show that uncertainty in amplitude calibration within 10% can be obtained for a source at 100 Mpc and the uncertainty increases and plateaus around 25% for a source at 250 Mpc and beyond [100, 101]. Such level of amplitude calibration might not be on par in accuracy and precision achieved using current methods but will provide an independent verification of the calibration methods currently employed. However, astrophysical calibration of the GW detectors, especially when multiple detectors are involved, has a potential to provide a good accuracy on the relative calibration between the detectors.

Accurate and precise calibration of interferometric gravitational-wave detectors is a key aspect of gravitational-wave detection and the science that can be extracted using these detections. Optimizing scientific rewards will require that the calibration techniques that are currently employed are constantly improved and new techniques be considered and developed for improved and better calibration accuracy.

APPENDIX A

PCAL POWER SENSORS RESPONSIVITY MEASUREMENTS

[Note: The work presented in this Appendix is produced in collaboration with Darkhan Tuyenbayev, Shivaraj Kandhasamy and Richard Savage and has previously been described in LIGO-T1500219.]

A.1. Working Principle

Responsivity relates the electrical output of the power sensor to the optical power input. Within Advanced LIGO Pcal systems, the following notation is used to describe the responsivity of different power sensors in units of volts per watts (V/W).

1. ρ_{G} - Gold Standard (GS),

2. ρ_{W_X} - Working Standard (WS),

3. ρ_{R} - receiver module power sensor (RxPD), and

4. ρ_{T} - transmitter module power sensor (TxPD).

Measuring the relative responsivity of the Pcal power sensors (RxPD and TxPD) to a Working Standard (WS) requires making measurements of powers in each Pcal beam at various positions in the Pcal beam path.

The following definitions will be used to express absolute powers in watts at different positions within the Pcal system:

1. $P_{ti}(t), P_{to}(t)$ - laser power in the inner and outer beams coming out of the transmitter module and going into the viewport, in watts;

2. $P_{ri}(t), P_{ro}(t)$ - laser power in the inner and outer beams going into the receiver module, in watts;

3. $P_t(t)$ - combined laser power in the inner and outer beams coming out of the transmitter module, $P_t(t) = P_{ti}(t) + P_{to}(t)$;

4. $P_r(t)$ - combined laser power in the inner and outer beams going into the receiver module, $P_r(t) = P_{ri}(t) + P_{ro}(t)$.

We can express the ratio of the absolute powers in the two beams at the output of the transmitter module (Tx) as

$$r_{io} = \frac{P_{ti}(t)}{P_{to}(t)} \tag{A.1}$$

Then we can write $P_{ti}(t)$ and $P_{to}(t)$ in terms of $P_t(t)$ and r_{io} as

$$P_{ti}(t) = P_t(t)\left(\frac{r_{io}}{1 + r_{io}}\right) \tag{A.2}$$

$$P_{to}(t) = P_t(t)\left(\frac{1}{1 + r_{io}}\right) \tag{A.3}$$

Defining the optical efficiency of each of the two beams as $e_i = P_{ri}(t)/P_{ti}(t)$ and $e_o = P_{ro}(t)/P_{to}(t)$ and using Eqs. A.2 and A.3 we can write the total power at the receiver module (Rx) as

$$P_r(t) = P_{ri}(t) + P_{ro}(t)$$

$$= P_{ti}(t)e_i + P_{to}(t)e_o$$

$$= P_t(t)\left[\frac{r_{io}}{1 + r_{io}}e_i + \frac{1}{1 + r_{io}}e_o\right] \tag{A.4}$$

151

The overall (combined) optical efficiency, e, of the system is given by

$$e = \frac{P_r(t)}{P_t(t)}$$

$$= \frac{r_{io}}{1 + r_{io}} e_i + \frac{1}{1 + r_{io}} e_o$$

$$= \frac{1}{1 + r_{io}} (r_{io} e_i + e_o) \tag{A.5}$$

The TxPD receives only a small fraction of the laser power which is proportional to $P_t(t)$ whereas the RxPD and the WS receive all the laser power in the beam they are measuring.

A.2. Ratio Measurements

Pcal power sensors to working standard relative responsivity measurements carried out at the end stations involve taking measurements in six different configurations. Using the definitions described above, for each measurement, we can write the voltage recorded by the power sensor (V) in terms of actual laser power (P) and the responsivity of the power sensor (ρ).

1. First, the outer beam is blocked and the laser power in the inner beam is measured with WS at the output of the transmitter module. Considering that the full output power (in both beams, including the one blocked) is $P_t(t_{1,i})$, we obtain the following time series.

   - $V_T(t_{1,i}) = P_t(t_{1,i}) \rho_T$

   - $V_{W_X}(t_{1,i}) = P_{ti}(t_{1,i}) \rho_{W_X} = P_t(t_{1,i}) \left(\dfrac{r_{io}}{1 + r_{io}} \right) \rho_{W_X}$

The ratio of these two gives[1]

$$R_{WtiT} = \frac{1}{N_1} \sum_{i=1}^{N_1} \frac{V_{W_X}(t_{1,i})}{V_T(t_{1,i})} = \left(\frac{r_{io}}{1 + r_{io}}\right) \frac{\rho_{W_X}}{\rho_T} \equiv m_1 \qquad (A.6)$$

2. The inner beam is blocked and the outer beam is measured with WS at the output from the transmitter module. The full output power is $P_t(t_{2,i})$.

    – $V_T(t_{2,i}) = P_t(t_{2,i})\rho_T$

    – $V_{W_X}(t_{2,i}) = P_{to}(t_{2,i})\rho_{W_X} = P_t(t_{2,i})\left(\dfrac{1}{1 + r_{io}}\right)\rho_{W_X}$

$$R_{WtoT} = \frac{1}{N_2} \sum_{i=1}^{N_2} \frac{V_{W_X}(t_{2,i})}{V_T(t_{2,i})} = \left(\frac{1}{1 + r_{io}}\right) \frac{\rho_{W_X}}{\rho_T} \equiv m_2 \qquad (A.7)$$

3. The outer beam is again blocked and the inner beam is measured with WS at the receiver module. The full output power is $P_t(t_{3,i})$.

    – $V_T(t_{3,i}) = P_t(t_{3,i})\rho_T$

    – $V_{W_X}(t_{3,i}) = P_{ti}(t_{3,i})e_i\rho_{W_X} = P_t(t_{3,i})\left(\dfrac{r_{io}}{1 + r_{io}}\right)e_i\rho_{W_X}$

$$R_{WriT} = \frac{1}{N_3} \sum_{i=1}^{N_3} \frac{V_{W_X}(t_{3,i})}{V_T(t_{3,i})} = \left(\frac{r_{io}}{1 + r_{io}}\right) e_i \frac{\rho_{W_X}}{\rho_T} \equiv m_3 \qquad (A.8)$$

4. The inner beam is blocked and the outer beam is measured with WS at the receiver module. The full output power is $P_t(t_{4,i})$.

    – $V_T(t_{4,i}) = P_t(t_{4,i})\rho_T$

    – $V_{W_X}(t_{4,i}) = P_{to}(t_{4,i})e_o\rho_{W_X} = P_t(t_{4,i})\left(\dfrac{1}{1 + r_{io}}\right)e_o\rho_{W_X}$

---

[1]In R_{WtiT}, R denotes *ratio* and WtiT denotes *Working* standard at *transmitter* module *inner* beam to *TxPD*.

$$R_{WroT} = \frac{1}{N_4} \sum_{i=1}^{N_4} \frac{V_{W_X}(t_{4,i})}{V_T(t_{4,i})} = \left(\frac{1}{1 + r_{io}}\right) e_o \frac{\rho_{W_X}}{\rho_T} \equiv m_4 \qquad (A.9)$$

5. The outer beam is blocked and the inner beam is measured with RxPD. The full output power is $P_t(t_{5,i})$.

  – $V_T(t_{5,i}) = P_t(t_{5,i})\rho_T$

  – $V_R(t_{5,i}) = P_{ti}(t_{5,i})e_i\rho_R = P_t(t_{5,i})\left(\frac{r_{io}}{1 + r_{io}}\right) e_i\rho_R$

$$R_{RiT} = \frac{1}{N_5} \sum_{i=1}^{N_5} \frac{V_R(t_{5,i})}{V_T(t_{5,i})} = \left(\frac{r_{io}}{1 + r_{io}}\right) e_i \frac{\rho_R}{\rho_T} \equiv m_5 \qquad (A.10)$$

6. The inner beam is blocked and the outer beam is measured with RxPD. The full output power is $P_t(t_{6,i})$.

  – $V_T(t_{6,i}) = P_t(t_{6,i})\rho_T$

  – $V_R(t_{6,i}) = P_{to}(t_{6,i})e_o\rho_R = P_t(t_{6,i})\left(\frac{1}{1 + r_{io}}\right) e_o\rho_R$

$$R_{RoT} = \frac{1}{N_6} \sum_{i=1}^{N_6} \frac{V_R(t_{6,i})}{V_T(t_{6,i})} = \left(\frac{1}{1 + r_{io}}\right) e_o \frac{\rho_R}{\rho_T} \equiv m_6 \qquad (A.11)$$

A background measurement is taken for each unique measurement setup. There are three unique measurement setups: one when the Working Standard is in the transmitter module (m_1 and m_2), second when the Working Standard is in the receiver module (m_3 and m_4) and the third when Working Standard is off the Pcal system (m_5 and m_6). The background is subtracted from each data point in the time series before calculating the ratios defined above.

A.3. Responsivity and optical efficiency calculations

After having obtained all the necessary measurements and calculating six basic ratios, m_1-m_6, these ratios can be used to obtain the overall optical efficiencies of the

system and relative responsivities between the Pcal power sensors and the Working Standard.

Power ratios between Pcal beams

The ratio of the absolute powers in the two beams at the transmitter module, r_{io}, can be obtained from ratios between (A.6) and (A.7).

$$\frac{m_1}{m_2} = \frac{\left(\dfrac{r_{io}}{1 + r_{io}}\right) \dfrac{\rho_{\mathrm{W}_X}}{\rho_{\mathrm{T}}}}{\left(\dfrac{1}{1 + r_{io}}\right) \dfrac{\rho_{\mathrm{W}_X}}{\rho_{\mathrm{T}}}} = r_{io} \tag{A.12}$$

Optical efficiencies

The optical efficiencies of the inner and outer beams, e_i and e_o, respectively, can be obtained from ratios between (A.6), (A.7), (A.8) and (A.9) as

$$\frac{m_3}{m_1} = \frac{\left(\dfrac{r_{io}}{1 + r_{io}}\right) e_i \dfrac{\rho_{\mathrm{W}_X}}{\rho_{\mathrm{T}}}}{\left(\dfrac{r_{io}}{1 + r_{io}}\right) \dfrac{\rho_{\mathrm{W}_X}}{\rho_{\mathrm{T}}}} = e_i \tag{A.13}$$

$$\frac{m_4}{m_2} = \frac{\left(\dfrac{1}{1 + r_{io}}\right) e_o \dfrac{\rho_{\mathrm{W}_X}}{\rho_{\mathrm{T}}}}{\left(\dfrac{1}{1 + r_{io}}\right) \dfrac{\rho_{\mathrm{W}_X}}{\rho_{\mathrm{T}}}} = e_o \tag{A.14}$$

The overall optical efficiency, e, can be derived by substituting Eqs. (A.12), (A.13) and (A.14) into Eq. (A.5).

$$
\begin{aligned}
e &= \left(\frac{1}{1 + r_{io}} \right) (r_{io} e_i + e_o) \\[2ex]
&= \left(\frac{1}{1 + \dfrac{m_1}{m_2}} \right) \left(\frac{m_1}{m_2} \frac{m_3}{m_1} + \frac{m_4}{m_2} \right) \\[2ex]
&= \left(\frac{m_2}{m_2 + m_1} \right) \left(\frac{m_3 + m_4}{m_2} \right)
\end{aligned}
$$

$$
\boxed{e = \frac{m_3 + m_4}{m_1 + m_2}} \tag{A.15}
$$

Relative responsivities

Adding Eqs. A.6 and A.7 we get

$$
m_1 + m_2 = \left(\frac{r_{io}}{1 + r_{io}} \right) \frac{\rho_{W_X}}{\rho_T} + \left(\frac{1}{1 + r_{io}} \right) \frac{\rho_{W_X}}{\rho_T} = \frac{\rho_{W_X}}{\rho_T}
$$

The relative responsivity between TxPD and the Working Standard, α_{TW}, can be written as

$$
\boxed{\alpha_{TW} \equiv \frac{\rho_T}{\rho_{W_X}} = \frac{1}{m_1 + m_2}} \tag{A.16}
$$

The ratio between the responsivity of the receiver module power sensor (RxPD) and the Working Standard (WS) can be obtained in two different ways using Eqs. A.8,

A.9, A.10, and A.11

$$\frac{m_5}{m_3} = \frac{\left(\dfrac{r_{io}}{1+r_{io}}\right) e_i \dfrac{\rho_R}{\rho_{\mathrm{T}}}}{\left(\dfrac{r_{io}}{1+r_{io}}\right) e_i \dfrac{\rho_{\mathrm{W}_X}}{\rho_{\mathrm{T}}}} = \frac{\rho_R}{\rho_{\mathrm{W}_X}} \tag{A.17a}$$

or

$$\frac{m_6}{m_4} = \frac{\left(\dfrac{1}{1+r_{io}}\right) e_o \dfrac{\rho_R}{\rho_{\mathrm{T}}}}{\left(\dfrac{1}{1+r_{io}}\right) e_o \dfrac{\rho_{\mathrm{W}_X}}{\rho_{\mathrm{T}}}} = \frac{\rho_R}{\rho_{\mathrm{W}_X}} \tag{A.17b}$$

In theory these two values should be equal but due to errors present in measurement data, we estimate the relative responsivity between RxPD and the Working Standard, α_{RW}, as the average of the two.

$$\boxed{\alpha_{RW} \equiv \frac{\rho_{\mathrm{R}}}{\rho_{\mathrm{W}_X}} = \frac{1}{2}\left(\frac{m_5}{m_3} + \frac{m_6}{m_4}\right)} \tag{A.18}$$

A.4. Uncertainty

The *effective* relative responsivities, α'_{TW} and α'_{RW}, are used to estimate the power on the test mass surface based on relative responsivity measured at transmitter and receiver module, α_{TW} and α_{RW}, and the optical efficiency, e, of the system. Since relative responsivity and optical efficiency are calculated from the same set of measurements, combining the two before uncertainty calculation avoids double-counting and thus overestimation of uncertainty.

A.4.1. TxPD to WS *effective* relative responsivity

The *effective* relative responsivity between TxPD and WS, α'_{TW}, is given by

$$\alpha'_{TW} = \frac{2}{(1+e)}\alpha_{TW}$$

$$= \left[\frac{2}{1+\dfrac{m_3+m_4}{m_1+m_2}}\right]\frac{1}{m_1+m_2}$$

$$\boxed{\alpha'_{TW} = \frac{2}{m_1+m_2+m_3+m_4}} \tag{A.19}$$

This assumes that the optical efficiency of the system is close to 1. If the optical efficiency is far from 1, it will grossly underestimate the laser power at the test mass.

The statistical uncertainty on this quantity is determined by taking the partial derivatives with respect to each ratio measurement

$$\frac{\partial \alpha'_{TW}}{\partial m_1} = \frac{\partial \alpha'_{TW}}{\partial m_2} = \frac{\partial \alpha'_{TW}}{\partial m_3} = \frac{\partial \alpha'_{TW}}{\partial m_4} = \frac{-2}{(m_1+m_2+m_3+m_4)^2} \tag{A.20}$$

and combining it in quadrature.

$$\sigma_{\alpha'_{TW}} = \left[\sum_{i=1}^{4}\left(\frac{\partial \alpha'_{TW}}{\partial m_i}\sigma_{m_i}\right)^2\right]^{\frac{1}{2}} \tag{A.21}$$

$$= \frac{\partial \alpha'_{TW}}{\partial m_1}\left[\sum_{i=1}^{4}\left(\sigma_{m_i}\right)^2\right]^{\frac{1}{2}} \tag{A.22}$$

Thus we can write the relative uncertainty in α'_{TW} as

$$\left(u_{rel}, \alpha'_{TW}\right)_{stat} = \frac{\sigma_{\alpha'_{TW}}}{\alpha'_{TW}} = \frac{\left[(\sigma_{m_1})^2 + (\sigma_{m_2})^2 + (\sigma_{m_3})^2 + (\sigma_{m_4})^2\right]^{\frac{1}{2}}}{|(m_1 + m_2 + m_3 + m_4)|} \qquad (\text{A.23})$$

A.4.2. RxPD to WS *effective* relative responsivity

The *effective* relative responsivity between RxPD and WS, α'_{RW}, is given by (again assuming that the optical efficiency is close to 1)

$$\alpha'_{RW} = \frac{2e}{(1+e)}\alpha_{RW}$$

$$= \left[\frac{2}{1 + \dfrac{m_3 + m_4}{m_1 + m_2}}\right]\left[\frac{(m_3 + m_4)}{(m_1 + m_2)}\right]\frac{1}{2}\left[\frac{m_5}{m_3} + \frac{m_6}{m_4}\right]$$

$$= \left[\frac{m_3 + m_4}{m_1 + m_2 + m_3 + m_4}\right]\left[\frac{m_5}{m_3} + \frac{m_6}{m_4}\right]$$

$$\alpha'_{RW} = \frac{1}{m_1 + m_2 + m_3 + m_4}\left[m_5 + \frac{m_3 m_6}{m_4} + \frac{m_4 m_5}{m_3} + m_6\right] \qquad (\text{A.24})$$

In order to make the uncertainty calculation simpler we define,

$$\alpha'_{RW} = \frac{A}{a} \qquad (\text{A.25})$$

where $A = \left[m_5 + \dfrac{m_3 m_6}{m_4} + \dfrac{m_4 m_5}{m_3} + m_6\right]$ and $a = (m_1 + m_2 + m_3 + m_4)$.

The partial derivative of α'_{RW} with respect to each measurement quantities results in following components

$$\frac{\partial \alpha'_{RW}}{\partial m_1} = \frac{A}{a}\left(-\frac{1}{a}\right) \tag{A.26}$$

$$\frac{\partial \alpha'_{RW}}{\partial m_2} = \frac{A}{a}\left(-\frac{1}{a}\right) \tag{A.27}$$

$$\frac{\partial \alpha'_{RW}}{\partial m_3} = \frac{1}{a}\left(\frac{m_6}{m_4} - \frac{m_4 m_5}{m_3^2} - \frac{A}{a}\right) \tag{A.28}$$

$$\frac{\partial \alpha'_{RW}}{\partial m_4} = \frac{1}{a}\left(\frac{m_5}{m_3} - \frac{m_3 m_6}{m_4^2} - \frac{A}{a}\right) \tag{A.29}$$

$$\frac{\partial \alpha'_{RW}}{\partial m_5} = \frac{1}{a}\left(1 + \frac{m_4}{m_3}\right) \tag{A.30}$$

$$\frac{\partial \alpha'_{RW}}{\partial m_6} = \frac{1}{a}\left(1 + \frac{m_3}{m_4}\right) \tag{A.31}$$

The standard uncertainty in α'_{RW} is given by

$$\sigma_{\alpha'_{RW}} = \left[\sum_{i=1}^{6}\left(\frac{\partial \alpha'_{RW}}{\partial m_i}\sigma_{m_i}\right)^2\right]^{\frac{1}{2}} \tag{A.32}$$

Thus we can write the relative uncertainty in α'_{RW} as

$$\left(u_{rel}, \alpha'_{RW}\right) = \frac{\sigma_{\alpha'_{RW}}}{\alpha'_{RW}} = \frac{1}{A}\left\{\left(\frac{A}{a}\right)^2 \sigma_{m_1}^2 + \left(\frac{A}{a}\right)^2 \sigma_{m_2}^2 \cdots \right.$$
$$+ \left(\frac{m_6}{m_4} - \frac{m_4 m_5}{m_3^2} - \frac{A}{a}\right)^2 \sigma_{m_3}^2 \cdots$$
$$+ \left(\frac{m_5}{m_3} - \frac{m_3 m_6}{m_4^2} - \frac{A}{a}\right)^2 \sigma_{m_4}^2 \cdots$$
$$\left. + \left(1 + \frac{m_4}{m_3}\right)^2 \sigma_{m_5}^2 + \left(1 + \frac{m_3}{m_4}\right)^2 \sigma_{m_6}^2\right\}^{\frac{1}{2}} \tag{A.33}$$

APPENDIX B

ACCOUNTING FOR IN-VACUUM OPTICAL LOSS MEASUREMENTS

During O1 and O2 observing runs, in-vacuum optical loss measurement was not possible so, laser powers measured at the transmitter and receiver modules, outside the vacuum enclosure, were used to estimate the power at the test mass. An assumption was made that the power loss between the input (incident) and output (reflected) sides were equal, which happens to be a good approximation.

During the vent between O2 and O3 observing runs, in-vacuum measurements of powers were made, allowing to apportion the losses between the input and output sides. A method to use that in-vacuum optical efficiency information to apportion the overall optical efficiency change measured from outside the vacuum in the future is described below. Here instead of assuming the power loss is equal on both sides, we make an assumption that the optical efficiency between the input and output sides remain constant.

B.1. Corrections for Optical Efficiencies

Six quantities, e_T^i, e_T^o, e_M^i, e_M^o, e_R^i and e_R^o are derived from measurements made inside and outside the vacuum envelope at the end stations. In accordance with the layout shown in Fig. B.1, e_T, e_M and e_R can be defined as the optical efficiency between T1 and T2, T2 and R2, and R2 and R1 respectively and the superscript "i" and "o" denote the inner (upper) and outer (lower) beams.

Assuming that the power in the inner and the outer beams are equal (they are within 2% of each other) we can write the combined optical efficiency as an average

161
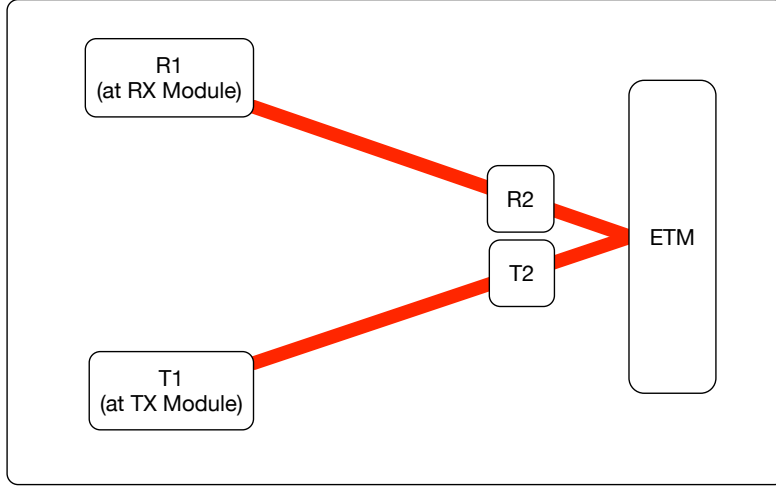
FIGURE B.1. Layout showing the position of the power senors at different locations of the Pcal beams for in-vacuum optical efficiency measurements (Only one beam is shown for clarity). Positions T1 and R1 are outside the vacuum at transmitter and receiver module respectively. Positions T2 and R2 are inside the vacuum, just in front of the test mass, on incident and reflected light respectively.

of the inner and the outer beam optical efficiencies.

$$e_T \equiv \frac{1}{2}(e_T^i + e_T^o) \tag{B.1a}$$

$$e_M \equiv \frac{1}{2}(e_M^i + e_M^o) \tag{B.1b}$$

$$e_R \equiv \frac{1}{2}(e_R^i + e_R^o) \tag{B.1c}$$

While we can use these data to measure the reflectivity of the test mass we impose the constraint that this reflectivity is unity[1]. To accomplish this, we multiply the transmitted-side and reflected-side optical efficiencies by the square root of the measured test mass optical efficiency. The transmitter and receiver side optical efficiencies, calculated based on the in-chamber measurements and corrected for unity

---

[1]We expect, based on numerous measurements, that the reflectivity is greater than 0.9999

test mass reflectivity are denoted by ϵ_{T0} and ϵ_{R0} and given in Eq. B.2.

$$\epsilon_{T0} \equiv \sqrt{e_M}\, e_T \tag{B.2a}$$

$$\epsilon_{R0} \equiv \sqrt{e_M}\, e_R \tag{B.2b}$$

The initial, calculated overall optical efficiency is thus given by

$$\epsilon_0 \equiv \epsilon_{T0} \times \epsilon_{R0} \tag{B.3}$$

Later, when measurements inside the vacuum envelope are not feasible, overall optical efficiencies for the two Pcal beams, e^i and e^o, can be measured with the transmitter-side and receiver-side Pcal power sensors and the measured overall efficiency is given by

$$e \equiv \frac{1}{2}(e^i + e^o) \tag{B.4a}$$

$$\equiv \epsilon \equiv \epsilon_T \times \epsilon_R \tag{B.4b}$$

where ϵ_T and ϵ_R are the new transmitter and receiver side optical efficiencies that will be determined from future out of vacuum measurements.

The ratio of optical efficiencies between the input and output side is defined as:

$$\beta \equiv \frac{\epsilon_{T0}}{\epsilon_{R0}} \tag{B.5}$$

We require that the ratio of the optical efficiencies for the transmitter and receiver sides, β, remains the same, i.e. we apportion changes in the overall optical efficiency

between the two sides using

$$\frac{\epsilon_T}{\epsilon_R} = \beta \tag{B.6}$$

Using Eq. B.4b and Eq. B.5 we can write the calculated transmitter and receiver side optical efficiencies, based on measurements made outside the vacuum envelope and with the assumption that the ETM reflectivity is unity, as

$$\epsilon_T = [\beta \, e]^{1/2} \tag{B.7a}$$

$$\epsilon_R = \left[\frac{e}{\beta}\right]^{1/2} \tag{B.7b}$$

where β is derived from one set of initial in-vacuum measurements and the total optical efficiency e is measured each time the end-station ratio measurements are made. We will also define a term η such that it tracks the change in overall optical efficiency of the system over time.i.e

$$\eta \equiv \frac{e}{\epsilon_0} = \frac{\epsilon}{\epsilon_0} \tag{B.8}$$

Alternatively, we can write the optical efficiency factors, ϵ_T and ϵ_R from Eqs. B.7, in terms of η and their original values as

$$\epsilon_T = \sqrt{\eta} \, \epsilon_{T0} \tag{B.9a}$$

$$\epsilon_R = \sqrt{\eta} \, \epsilon_{R0} \tag{B.9b}$$

Thus, η keeps track of both the optical efficiency $\epsilon(e)$ and its component values from the transmitter and the receiver sides.

With the power incident on the mirror denoted by $P_M(t)$, we can estimate that power using the following relations

$$P_M(t) = P_T(t)\ \epsilon_T \tag{B.10a}$$

$$P_M(t) = P_R(t)/\epsilon_R \tag{B.10b}$$

where $P_T(t)$ and $P_R(t)$ are the powers measured at the transmitter and receiver modules respectively. Using Eqs. B.7 and B.10, we can write $P_T(t)$ and $P_R(t)$ as

$$P_T(t) = \left[\frac{1}{\beta\ e}\right]^{1/2} P_M(t) \equiv \mathcal{E}_T\ P_M(t) \tag{B.11a}$$

$$P_R(t) = \left[\frac{e}{\beta}\right]^{1/2} P_M(t) \equiv \mathcal{E}_R\ P_M(t) \tag{B.11b}$$

where $\mathcal{E}_T$ and $\mathcal{E}_R$ are the correction factors associated with change in optical efficiency. Using the definitions of responsivity from Eq. 3.18, we can write the voltages measured by the transmitter and receiver module power sensors as:

$$V_T(t) = P_T(t)\rho_T = P_M(t) \underbrace{\left[\mathcal{E}_T\ \rho_T\right]}_{\rho'_T} \tag{B.12a}$$

$$V_R(t) = P_R(t)\rho_R = P_M(t) \underbrace{\left[\mathcal{E}_R\ \rho_R\right]}_{\rho'_R} \tag{B.12b}$$

Here ρ'_T and ρ'_R are responsivity of the transmitter and receiver module power sensor corrected for optical efficiency such that they represent the power measured at the

Parameter	O2 Method	O3 Method
$\mathcal{E}_T$	$2/(1 + e)$	$(1/\beta \, e)^{1/2}$
$\mathcal{E}_R$	$2e/(1 + e)$	$(e/\beta)^{1/2}$

TABLE B.1. $\mathcal{E}_T$ and $\mathcal{E}_R$ translate the power measured at the transmitter and receiver module to the power at the test mass (mirror). These terms for O2 (without in-vacuum measurements) and O3 (with in-vacuum measurements) are slightly different and are listed above.

test mass and can be written in more expanded form using Eq. B.13.

$$\rho'_T = \mathcal{E}_T \, \alpha_{TW} \, \alpha_{WG} \, \rho_G \tag{B.13a}$$

$$\rho'_R = \mathcal{E}_R \, \alpha_{RW} \, \alpha_{WG} \, \rho_G \tag{B.13b}$$

These equations (Eqs. B.13) have the same form as the equations of ρ'_T and ρ'_R in 3.28 but the crucial difference is the definition of $\mathcal{E}_T$ and $\mathcal{E}_R$. Symbolic values of $\mathcal{E}_T$ and $\mathcal{E}_R$ for the old method (O2) and the new method (O3) are listed in Table B.1.

B.2. Uncertainty

To estimate the uncertainty we can write *effective* relative responsivities of the transmitter and receiver module power sensors, α'_{TW} and α'_{RW}, as:

$$\alpha'_{TW} = \mathcal{E}_T \, \alpha_{TW} = \frac{1}{\sqrt{\beta e}} \, \alpha_{TW} \tag{B.14a}$$

$$\alpha'_{RW} = \mathcal{E}_R \, \alpha_{RW} = \sqrt{\frac{e}{\beta}} \, \alpha_{TW} \tag{B.14b}$$

Given that β does not change over time the uncertainty associated with β comes from the measurement uncertainty. We can write β in terms of the optical efficiency measurements made inside the vacuum as

$$\beta = \frac{e_T^i + e_T^o}{e_R^i + e_R^o} \tag{B.15}$$

Defining $e_T^i = e_1$, $e_T^o = e_2$, $e_R^i = e_3$, and $e_R^o = e_4$ to make the uncertainty calculations easier and differentiating with respect to each component the statistical uncertainty on β can be written as

$$(u_{rel}, \beta)_{stat} = \frac{\sigma_\beta}{\beta} = \left[\frac{(\sigma_{e_1})^2 + (\sigma_{e_2})^2}{(e_1 + e_2)^2} + \frac{(\sigma_{e_3})^2 + (\sigma_{e_4})^2}{(e_3 + e_4)^2} \right]^{\frac{1}{2}} \tag{B.16}$$

To estimate the uncertainty in the rest of the quantities we can rewrite α_{TW}' and α_{RW}' in terms of six measurement ratios $(m_1 - m_6)$ that we make during the end-station calibration measurement.

B.2.1. TxPD to WS *effective* relative responsivity (α_{TW}')

From Eq. B.14a we can write TxPD to WS *effective* relative responsivity as

$$\alpha_{TW}' = \frac{1}{\sqrt{\beta e}} \, \alpha_{TW}$$

$$= \frac{1}{\sqrt{\beta}} \left[\sqrt{\frac{(m_1 + m_2)}{(m_3 + m_4)}} \right] \frac{1}{m_1 + m_2}$$

$$\alpha_{TW}' = \frac{1}{\sqrt{\beta}} \left[\frac{1}{\sqrt{(m_1 + m_2)(m_3 + m_4)}} \right] \tag{B.17}$$

167

Now taking partial derivatives of α'_{TW} with respect to measurement quantities results in

$$\frac{\partial \alpha'_{TW}}{\partial m_1} = \frac{\partial \alpha'_{TW}}{\partial m_2} = -\frac{1}{2} \frac{1}{\sqrt{\beta(m_1 + m_2)(m_3 + m_4)}} \frac{1}{(m_1 + m_2)} \tag{B.18}$$

$$\frac{\partial \alpha'_{TW}}{\partial m_3} = \frac{\partial \alpha'_{TW}}{\partial m_4} = -\frac{1}{2} \frac{1}{\sqrt{\beta(m_1 + m_2)(m_3 + m_4)}} \frac{1}{(m_3 + m_4)} \tag{B.19}$$

$$\frac{\partial \alpha'_{TW}}{\partial \beta} = -\frac{1}{2} \frac{1}{\sqrt{\beta(m_1 + m_2)(m_3 + m_4)}} \frac{1}{\beta} \tag{B.20}$$

Using these partial derivatives we can write the relative uncertainty in α'_{TW} as

$$\left(u_{rel}, \alpha'_{TW}\right)_{stat} = \frac{\sigma_{\alpha'_{TW}}}{\alpha'_{TW}} = \frac{1}{2} \left[\frac{(\sigma_{m_1})^2 + (\sigma_{m_2})^2}{(m_1 + m_2)^2} + \frac{(\sigma_{m_3})^2 + (\sigma_{m_4})^2}{(m_3 + m_4)^2} + \left(\frac{\sigma_\beta}{\beta}\right)^2 \right]^{\frac{1}{2}}$$

$$\tag{B.21}$$

B.2.2. RxPD to WS *effective* relative responsivity (α'_{RW})

From Eq. B.14b we can write RxPD to WS *effective* relative responsivity as

$$\alpha'_{RW} = \sqrt{\frac{e}{\beta}} \, \alpha_{RW}$$

$$= \frac{1}{\sqrt{\beta}} \left(\sqrt{\frac{(m_3 + m_4)}{(m_1 + m_2)}} \right) \left[\frac{1}{2} \left(\frac{m_5}{m_3} + \frac{m_6}{m_4} \right) \right]$$

$$\alpha'_{RW} = \frac{1}{2\sqrt{\beta}} \left[\sqrt{\frac{(m_3 + m_4)}{(m_1 + m_2)}} \left(\frac{m_5}{m_3} + \frac{m_6}{m_4} \right) \right] \tag{B.22}$$

In order to make the uncertainty calculation simpler we define,

$$\alpha'_{RW} = \frac{1}{2\sqrt{\beta}} \, A \, a \tag{B.23}$$

such that,

$$A = \sqrt{\frac{(m_3 + m_4)}{(m_1 + m_2)}}$$

$$a = \left(\frac{m_5}{m_3} + \frac{m_6}{m_4} \right)$$

The partial derivative of α'_{RW} with respect to each measurement quantity results in following components:

$$\frac{\partial \alpha'_{RW}}{\partial m_1} = \frac{Aa}{2\sqrt{\beta}} \left(-\frac{1}{2} \frac{1}{(m_1 + m_2)} \right) \tag{B.24}$$

$$\frac{\partial \alpha'_{RW}}{\partial m_2} = \frac{Aa}{2\sqrt{\beta}} \left(-\frac{1}{2} \frac{1}{(m_1 + m_2)} \right) \tag{B.25}$$

$$\frac{\partial \alpha'_{RW}}{\partial m_3} = \frac{Aa}{2\sqrt{\beta}} \left(\frac{1}{2} \frac{1}{(m_3 + m_4)} - \frac{1}{a} \frac{m_5}{m_3^2} \right) \tag{B.26}$$

$$\frac{\partial \alpha'_{RW}}{\partial m_4} = \frac{Aa}{2\sqrt{\beta}} \left(\frac{1}{2} \frac{1}{(m_3 + m_4)} - \frac{1}{a} \frac{m_6}{m_4^2} \right) \tag{B.27}$$

$$\frac{\partial \alpha'_{RW}}{\partial m_5} = \frac{Aa}{2\sqrt{\beta}} \left(\frac{1}{a} \frac{1}{m_3} \right) \tag{B.28}$$

$$\frac{\partial \alpha'_{RW}}{\partial m_6} = \frac{Aa}{2\sqrt{\beta}} \left(\frac{1}{a} \frac{1}{m_4} \right) \tag{B.29}$$

$$\frac{\partial \alpha'_{RW}}{\partial \beta} = \frac{Aa}{2\sqrt{\beta}} \left(-\frac{1}{2\beta} \right) \tag{B.30}$$

Using these partial derivatives we can write the relative uncertainty in α'_{RW} as

$$
\left(u_{rel}, \alpha'_{RW}\right)_{stat} = \left\{ \left(\frac{1}{2}\frac{1}{(m_1 + m_2)}\right)^2 \sigma_{m_1}^2 + \left(\frac{1}{2}\frac{1}{(m_1 + m_2)}\right)^2 \sigma_{m_2}^2 \cdots \right.
$$
$$
+ \left(\frac{1}{2}\frac{1}{(m_3 + m_4)} - \frac{1}{a}\frac{m_5}{m_3^2}\right)^2 \sigma_{m_3}^2 + \left(\frac{1}{a}\frac{1}{m_3}\right)^2 \sigma_{m_5}^2 \cdots
$$
$$
+ \left(\frac{1}{2}\frac{1}{(m_3 + m_4)} - \frac{1}{a}\frac{m_6}{m_4^2}\right)^2 \sigma_{m_4}^2 + \left(\frac{1}{a}\frac{1}{m_4}\right)^2 \sigma_{m_6}^2 \cdots
$$
$$
\left. + \frac{1}{4}\left(\frac{\sigma_\beta}{\beta}\right)^2 \right\}^{\frac{1}{2}}
$$

(B.31)

where σ_{m_i} are the standard deviations of the corresponding ratios.

B.2.3. Systematic uncertainty in β, $\mathcal{E}_T$, and $\mathcal{E}_R$

The uncertainty described above is only the statistical uncertainty that comes from the measurements. However to get the accuracy of the calibration right we need to understand the systematic uncertainty in our measurements.

One way of estimating the overall uncertainty in β is by comparing the optical efficiency calculated using the measurements made at the transmitter and receiver modules with the optical efficiency calculated by multiplying the optical efficiencies between the transmitter and receiver sides from measurements made inside the vacuum enclosure. The former assumes unity for the test mass power reflectivity. This assumption is justified based on the resonance of light on the interferometer arm cavities that sets the upper limit on losses (transmission, scattering and absorption) of less than 0.001%. The latter measures the overall losses, without this assumption of unity reflectivity, and thus provides an estimate of the uncertainty in our calculation of $e0 = \epsilon_{T0} \times \epsilon_{R0}$, and thus also of $\beta = \epsilon_{T0}/\epsilon_{R0}$. Similarly, calculating the test mass

reflectivity from in-chamber measurements and evaluating the deviation from unity enables estimating the uncertainty in β.

$\mathcal{E}_T$ and $\mathcal{E}_R$, the coefficients that convert powers measured at the transmitter module and receiver modules to estimated power incident on and reflected from the test mass, based on transmitter and receiver side optical efficiencies, ϵ_T and ϵ_R, are given by

$$\mathcal{E}_T = \frac{1}{\epsilon_T} = \frac{1}{\sqrt{\alpha}\,\epsilon_{T0}} \tag{B.32}$$

$$\mathcal{E}_R = \epsilon_R = \sqrt{\alpha}\,\epsilon_{R0} \tag{B.33}$$

where $\alpha = e/e_0$ is the measured relative change in the overall optical efficiency.

While we have assumed that β is constant to estimate, ϵ_T and ϵ_R, to conservatively estimate uncertainty in these correction factors, we use *Type-B* uncertainty.

So for $\epsilon_T = \sqrt{\alpha}\,\epsilon_{T0}$, the values could be between $\alpha\epsilon_{T0}$ and ϵ_{T0} and for $\epsilon_R = \sqrt{\alpha}\,\epsilon_{R0}$, the values could be between $\alpha\epsilon_{R0}$ and ϵ_{R0}. Using these we can write the relative uncertainty in ϵ_T and ϵ_R as

$$u_{rel},\epsilon_T = \frac{1}{\sqrt{3}}\left(\frac{\epsilon_{T0} - \alpha\,\epsilon_{T0}}{\epsilon_{T0} + \alpha\,\epsilon_{T0}}\right) = \frac{1}{\sqrt{3}}\left(\frac{1-\alpha}{1+\alpha}\right) \tag{B.34}$$

$$u_{rel},\epsilon_R = \frac{1}{\sqrt{3}}\left(\frac{\epsilon_{R0} - \alpha\,\epsilon_{R0}}{\epsilon_{R0} + \alpha\,\epsilon_{R0}}\right) = \frac{1}{\sqrt{3}}\left(\frac{1-\alpha}{1+\alpha}\right) \tag{B.35}$$

Thus the uncertainty in $\mathcal{E}_T$ and $\mathcal{E}_R$ is given by

$$u_{rel},\mathcal{E}_T = u_{rel},\mathcal{E}_R = \frac{1}{\sqrt{3}}\left(\frac{1-\alpha}{1+\alpha}\right) \tag{B.36}$$

171

For illustration, if the overall optical efficiency is to change from 0.987 to 0.982, a change in optical loss from 1.3% to 1.6%, the estimated relative uncertainties in $\mathcal{E}_T$ and $\mathcal{E}_R$ would be ~0.10%.

APPENDIX C

CALIBRATION SUBWAY MAP
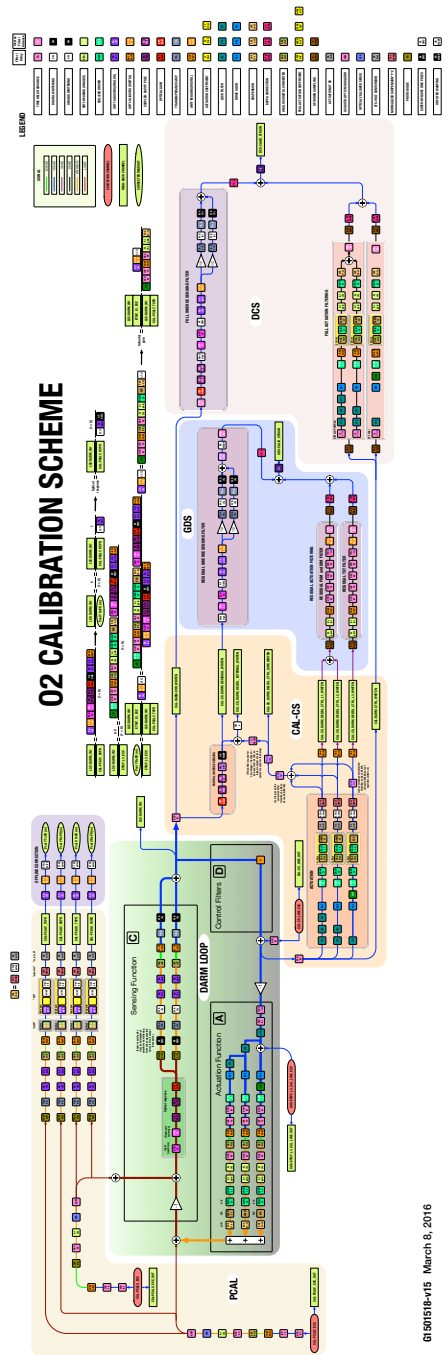
FIGURE C.1. Advanced LIGO Calibration Scheme shown using blocks and arrows.

173

APPENDIX D

ABBREVIATIONS

LIGO   Laser Interferometer Gravitational-wave Observatory

GRB   Gamma Ray Bursts

GW   Gravitational Wave

GPS   Global Positioning System

Mpc   Megaparsec

H1   Hanford interferometer 1

BS   Beam Splitter

Nd:YAG   Neodymium-doped Yttrium Aluminum Garnet

IMC   Input Mode Cleaner

PRM   Power Recycling Mirror

SRM   Signal Recycling Mirror

OMC   Output Mode Cleaner

O2   Observing run 2

FSM   Free-swinging Michelson

ETM   End Test Mass

PDH   Pound-Drever-Hall

Pcal	Photon calibrator
L1	Livingston interferometer 1
DARM	Differential ARM
SHoES	Supernova, H0, for the Equation of State of Dark energy
CMB	Cosmic Microwave Background
SNR	Signal-to-Noise Ratio
BNS	Binary Neutron Star
EoS	Equation of State
PN	Post-Newtonian
CW	Continuous Wave
RxPD	Receiver module Photo Diode (Power Sensor)
AOM	Acousto-Optic Modulator
Nd:YLF	Neodymium-doped Yttrium Lithium Fluoride
BRDF	Bidirectional Reflectance Distribution Function
RF	Radio Frequency
InGaAs	Indium Gallium Arsenide
TxPD	Transmitter module Photo Diode (Power Sensor)
ACB	Arm Cavity Baffles

OFS	Optical Follower Servo
OFSPD	Optical Follower Servo Photo-diode
RPN	Relative Power Noise
O1	Observing run 1
ESD	Electrostatic Drive
NIST	National Institute of Standards and Technology
GS	Gold Standard
WS	Working Standard
LHO	LIGO Hanford Observatory
LLO	LIGO Livingston Observatory
WSH	Working Standard Hanford
WSL	Working Standard Livingston
CS	Checking Standard
WBS	Wedged Beam Splitter
AA	Anti-aliasing
DTD	Digital Time Delay
IOP	Input Output Processor
DFT	Discrete Fourier Transform

PUM   Penultimate Mass

UIM   Upper Intermediate Mass

TST   Test Mass

GDS   Global Diagnostic System

IIR   Infinite Impulse Response

EM   Electromagnetic

BED   Bulk Elastic Deformation

IFO   Interferometer

DES   Dark Energy Survey

FEA   Finite Element Analysis

REFERENCES CITED

[1] A. Einstein. On the electrodynamics of moving bodies. *Annalen Phys.*, 17: 891–921, 1905.

[2] A. Einstein. The Field Equations of Gravitation. *Sitzungsber. Preuss. Akad. Wiss. Berlin (Math. Phys.)*, 1915:844–847, 1915.

[3] K. D. Kokkotas. Gravitational wave Physics. *Encyclopedia of Physical Science and Technology*, 7, 2002.

[4] J. A. Wheeler. *Geons, Black holes, and Quantum foam: A life in physics.* New York, USA: Norton, 2000.

[5] A. Einstein. Approximative Integration of the Field Equations of Gravitation. *Sitzungsber. Preuss. Akad. Wiss. Berlin (Math. Phys.)*, 1916:688–696, 1916.

[6] G. M. Clemence. The Relativity Effect in Planetary Motions. *Reviews of Modern Physics*, 19:361–364, October 1947.

[7] C. W. Chou, D. B. Hume, T. Rosenband, and D. J. Wineland. Optical Clocks and Relativity. *Science*, 329(5999):1630–1633, 2010.

[8] N. S. Hetherington. Sirius B and the gravitational redshift - a historical review. *Royal Astronomical Society, Quarterly Journal*, 21:246–252, September 1980.

[9] S. R. G. Joyce, M. A. Barstow, J. B. Holberg, H. E. Bond, S. L. Casewell, and M. R. Burleigh. The gravitational redshift of Sirius B. , 481:2361–2370, Dec 2018.

[10] S. S. Shapiro, J. L. Davis, D. E. Lebach, et al. Measurement of the Solar Gravitational Deflection of Radio Waves using Geodetic Very-Long-Baseline Interferometry Data, 1979–1999. *Phys. Rev. Lett.*, 92:121101, Mar 2004.

[11] P. R. Saulson. *Fundamentals of Interferometric Gravitational Wave Detectors.* World Scientific, 1994. ISBN 9789810218201.

[12] J. M. Antelis and C. Moreno. Obtaining gravitational waves from inspiral binary systems using LIGO data. *Eur. Phys. J. Plus*, 132(1):10, 2017.

[13] B. P. Abbott et al. Observation of gravitational waves from a binary black hole merger. *Phys. Rev. Lett.*, 116:061102, Feb 2016.

[14] Paul D. Lasky. Gravitational Waves from Neutron Stars: A Review. *Publications of the Astronomical Society of Australia*, 32:e034, 2015.

[15] B. P. Abbott et al. First narrow-band search for continuous gravitational waves from known pulsars in advanced detector data. *Phys. Rev.*, D96(12):122006, 2017.

[16] P. Jaranowski, A. Królak, and B. F. Schutz. Data analysis of gravitational-wave signals from spinning neutron stars: The signal and its detection. *Phys. Rev. D*, 58:063001, Aug 1998.

[17] Joseph D. Romano and Neil J. Cornish. Detection methods for stochastic gravitational-wave backgrounds: a unified treatment. *Living Rev. Rel.*, 20(1):2, 2017.

[18] Benjamin P. Abbott et al. Upper Limits on the Stochastic Gravitationa-Wave Background from Advanced LIGOs First Observing Run. *Phys. Rev. Lett.*, 118 (12):121101, 2017.

[19] O. D. Aguiar. The Past, Present and Future of the Resonant-Mass Gravitational Wave Detectors. *Res. Astron. Astrophys.*, 11:1–42, 2011.

[20] M. E. Gertsenshtein and V. I. Pustovoit. On the Detection of Low Frequency Gravitational Waves. *Sov. Phys. JETP*, 16:433, 1962.

[21] R. Weiss. Electronically Coupled Broadband Gravitational Antenna. *Quarterly Progress Report-Research Laboratory of Electronics (MIT)*, 105:54, 1972.

[22] R. A. Hulse and J. H. Taylor. Discovery of a pulsar in a binary system. *The Astrophysical Journal Letters*, 195:L51–L53, Jan 1975.

[23] Thomas J. Kane and Robert L. Byer. Monolithic, unidirectional single-mode Nd:YAG ring laser. *Opt. Lett.*, 10(2):65–67, Feb 1985.

[24] P. Kwee, C. Bogan, K. Danzmann, et al. Stabilized high-power laser system for the gravitational wave detector advanced LIGO. *Opt. Express*, 20(10): 10617–10634, May 2012.

[25] B. P. Abbott et al. Sensitivity of the Advanced LIGO detectors at the beginning of gravitational wave astronomy. *Phys. Rev.*, D93(11):112004, 2016.

[26] J. Aasi et al. Advanced LIGO. *Class. Quant. Grav.*, 32:074001, 2015.

[27] S. M. Aston et al. Update on quadruple suspension design for advanced LIGO. *Classical and Quantum Gravity*, 29(23):235004, Oct 2012.

[28] R. Adhikari, G. Gonzalez, M. Landry, et al. Calibration of the LIGO detectors for the First LIGO Science Run. *Classical and Quantum Gravity*, 20(17): 903–914, September 2003.

[29] E. Goetz and R. L. Savage. Calibration of the LIGO displacement actuators via laser frequency modulation. *Classical and Quantum Gravity*, 27(21):215001, 2010.

[30] E. Goetz et al. Accurate calibration of test mass displacement in the LIGO interferometers. *Class. Quantum Grav.*, 27:084024, 2010.

[31] L. Lindblom. Optimal Calibration Accuracy for Gravitational Wave Detectors. *Phys. Rev.*, D80:042005, 2009.

[32] M Rakhmanov, R.L Savage, D.H Reitze, and D.B Tanner. Dynamic resonance of light in FabryPerot cavities. *Physics Letters A*, 305(5):239 – 244, 2002.

[33] A. Sottile. Characterization of the Photon Calibrator data from LIGO's sixth Science Run. Master's thesis, University of Pisa, 2011.

[34] B. P. Abbott et al. Calibration of the Advanced LIGO detectors for the discovery of the binary black-hole merger GW150914. *Phys. Rev. D*, 2016.

[35] C. Cahillane et al. Calibration uncertainty for Advanced LIGO's first and second observing runs. *Phys. Rev. D*, 96:102001, Nov 2017.

[36] B. P. Abbott et al. Tests of general relativity with GW150914. *Phys. Rev. Lett.*, 116(22):221101, 2016.

[37] B. P. Abbott et al. On the Progenitor of Binary Neutron Star Merger GW170817. *Astrophys. J.*, 850(2):L40, 2017.

[38] B. P. Abbott et al. Properties of the binary neutron star merger GW170817. *Phys. Rev. X*, 2018.

[39] B. P. Abbott et al. Estimating the Contribution of Dynamical Ejecta in the Kilonova Associated with GW170817. *Astrophys. J.*, 850(2):L39, 2017.

[40] A. Albert et al. Search for High-energy Neutrinos from Binary Neutron Star Merger GW170817 with ANTARES, IceCube, and the Pierre Auger Observatory. *Astrophys. J.*, 850(2):L35, 2017.

[41] B. P. Abbott et al. GW170817: Measurements of Neutron Star Radii and Equation of State. *Phys. Rev. Lett.*, 121:161101, Oct 2018.

[42] B. P. Abbott et al. A gravitational-wave standard siren measurement of the Hubble constant. *Nature*, 551(7678):85–88, 2017.

[43] B. P. Abbott et al. Gravitational Waves and Gamma-rays from a Binary Neutron Star Merger: GW170817 and GRB 170817A. *Astrophys. J.*, 848(2): L13, 2017.

[44] A. G. Riess et al. A 2.4% Determination of the Local Value of the Hubble Constant. *Astrophys. J.*, 826(1):56, 2016.

[45] P. A. R. Ade et al. Planck 2015 results. XIII. Cosmological parameters. *Astron. Astrophys.*, 594:A13, 2016.

[46] H. Y. Chen, M. Fishbach, and D. E. Holz. A two percent Hubble constant measurement from standard sirens within five years. *Nature*, 562(7728): 545–547, 2018.

[47] Jose Mara Ezquiaga and Miguel Zumalacrregui. Dark Energy in light of Multi-Messenger Gravitational-Wave astronomy. *Front. Astron. Space Sci.*, 5: 44, 2018.

[48] S. Vitale et al. Effect of calibration errors on Bayesian parameter estimation for gravitational wave signals from inspiral binary systems in the Advanced Detectors era. *Phys. Rev.*, D85:064034, 2012.

[49] D. A. Clubley et al. Calibration of the Glasgow 10 m prototype laser interferometric gravitational wave detector using photon pressure. *Phys. Lett. A*, 283:85, 2001.

[50] K. Mossavi et al. A photon pressure calibrator for the GEO600 gravitational wave detector. *Phys. Lett. A*, 353:1, 2006.

[51] Justice Bruursema. Calibration of the LIGO Interferometer Using the Recoil of Photons. *LIGO Document Control Center*, T030266, 2003.

[52] D. Sigg. Strain Calibration in LIGO. *LIGO Document Control Center*, T970101, 1997.

[53] S. Hild et al. Photon Pressure Induced Test Mass Deformation in GravitationalWave Detectors. *Class. Quantum Grav.*, 24:56815688, 2007.

[54] E. Goetz et al. Precise calibration of LIGO test mass actuators using photon radiation pressure. *Class. Quant. Grav.*, 26:245011, 2009.

[55] S. Karki, D. Tuyenbayev, S. Kandhasamy, et al. The Advanced LIGO photon calibrators. *Rev. of Sci. Inst.*, 87, 2016.

[56] C. Biwer et al. Validating gravitational-wave detections: The Advanced LIGO hardware injection system. *Phys. Rev. D*, 95:062002, Mar 2017.

[57] L. Canete et al. Optical Follower Servo design for the calibration of a gravitational wave detector. *LIGO Document Control Center*, T130442, 2013.

[58] LIGO Photon Calibrator Team. Pcal Final Design Document. *LIGO Document Control Center*, T1100068, 2015.

181

[59] H. P. Daveloza et al. Controlling calibration errors in gravitational-wave detectors by precise location of calibration forces. *Journal of Physics: Conference Series*, 363:012007, 2012.

[60] Photon calibrator Team. Photon Calibrator Gold Standard NIST calibration. *LIGO Document Control Center*, T1800104, 2018.

[61] S. Erickson. Investigation of Variations in the Absolute Calibration of the Laser Power Sensors for the LIGO Photon Calibrators. *LIGO Document Control Center*, T080316, 2008.

[62] B.N. Taylor and C.E. Kuyatt. Guidelines for Evaluating and Expressing the Uncertainty of NIST Measurement Results. *National Institute of Standards and Technology*, 2001.

[63] Photon calibrator Team. LHO Y-End RxPD and TxPD Calibration Trends. *LIGO Document Control Center*, T1500131-v8, 2016.

[64] Photon calibrator Team. LHO X-End RxPD and TxPD Calibration Trends. *LIGO Document Control Center*, T1500129-v10, 2016.

[65] Photon calibrator Team. LLO Y-End RxPD and TxPD Calibration Trends. *LIGO Document Control Center*, T1500160-v6, 2016.

[66] Photon calibrator Team. LLO X-End RxPD and TxPD Calibration Trends. *LIGO Document Control Center*, T1500161-v6, 2016.

[67] Stefan Kück. Final report on EUROMET comparison EUROMET.PR-S2 (Project No. 156): Responsivity of detectors for radiant power of lasers. *Metrologia*, 47(1A):02003, 2010.

[68] S. Kandhasamy, C Blair, et al. Frequency dependence of Pcal calibration due to electronics. *aLIGO Log Book*, 2015.
https://alog.ligo-la.caltech.edu/aLOG/index.php?callRep=18106.

[69] D. Tuyenbayev. Optimization of calibration line frequencies with Fisher matrices. *LIGO Document Control Center*, T1600386-v1, 2016.

[70] E.D. Hall. Fisher-matrix-based calibration line placement. *LIGO Document Control Center*, T1600327-v1, 2016.

[71] S. Kandhasamy et al. h(t) sign convention measurement using Pcal. *aLIGO Log Book*, 2015.
https://alog.ligo-la.caltech.edu/aLOG/index.php?callRep=18406.

[72] Y. Aso et al. Accurate measurement of the time delay in the response of the LIGO gravitational wave detectors. *Class. Quantum Grav.*, 26(5):055010, 2009.

[73] D. Tuyenbayev, S. Karki, et al. Improving LIGO calibration accuracy by tracking and compensating for slow temporal variations. *Class. Quant. Grav.*, 34(1):015002, 2017.

[74] Cahillane C. Kissel, J. and M. Hulko. O2 C02 Calibration Uncertainty Results Review/Update/Summary. *LIGO Document Control Center*, G1800319-v1, 2018.

[75] D. Tuyenbayev. Extending the scientific reach of Advanced LIGO by compensating for temporal variations in the calibration of the detectors. *LIGO Document Control Center*, T1700451-v1, 2017.

[76] S. Kandhasamy. DARM Actuation using PCAL. *aLIGO Log Book*, 2016. `https://alog.ligo-la.caltech.edu/aLOG/index.php?callRep=28500`.

[77] Kentaro Takami, Luciano Rezzolla, and Luca Baiotti. Spectral properties of the post-merger gravitational-wave signal from binary neutron stars. *Phys. Rev.*, D91(6):064001, 2015.

[78] K. Hotokezaka et al. Mass ejection from the merger of binary neutron stars. *Physical Review D - Particles, Fields, Gravitation and Cosmology*, 87(2):1–27, 2013.

[79] A. Bauswein, H. T. Janka, K. Hebeler, et al. Equation-of-state dependence of the gravitational-wave signal from the ring-down phase of neutron-star mergers. *Phys. Rev.*, D86:063001, 2012.

[80] B. P. Abbott et al. Search for Post-merger Gravitational Waves from the Remnant of the Binary Neutron Star Merger GW170817. *Astrophys. J.*, 851(1): L16, 2017.

[81] M. Rakhmanov, R. L. Savage, D. H. Reitze, et al. Dynamic resonance of light in Fabry-Perot cavities . *Physics Letters A*, 305:239–244, December 2002.

[82] M. A.Badhan et al. Analyzing Elastic Deformation of Test Masses in LIGO. *LIGO Document Control Center*, T09004010-v1, 2009.

[83] N. DeLillo. Effect of ETM deformation in calibration. *LIGO Document Control Center*, T1700213-v1, 2017.

[84] T. Accadia et al. Reconstruction of the gravitational wave signal $h(t)$ during the Virgo science runs and independent validation with a photon calibrator. *Class. Quant. Grav.*, 31:165013, 2014.

[85] C. Blair. LLO ETMX Resonant Modes. *LIGO Document Control Center*, T1600165-v1, 2016.

[86] C. Blair. Identification of Test mass Resonant Modes. *LIGO Document Control Center*, T1600080-v1, 2016.

[87] B. P. Abbott et al. Properties of the Binary Black Hole Merger GW150914. *Phys. Rev. Lett.*, 116(24):241102, 2016.

[88] B. P. Abbott et al. Binary Black Hole Population Properties Inferred from the First and Second Observing Runs of Advanced LIGO and Advanced Virgo. 2018.

[89] A. D. Viets, M. Wade, A.L. Urban, et al. Reconstructing the calibrated strain signal in the Advanced LIGO detectors. *Classical and Quantum Gravity*, 35(9): 095015, 2018.

[90] K. Chatziioannou et al. PE update for 170729 in C02 data. *LIGO Document Control Center*, G1800842, 2018.

[91] Bernard F. Schutz. Determining the Hubble Constant from Gravitational Wave Observations. *Nature*, 323:310–311, 1986. doi: 10.1038/323310a0.

[92] D. E. Holz and S. A. Hughes. Using gravitational-wave standard sirens. *Astrophys. J.*, 629:15–22, 2005.

[93] LVC-DES Collaboration. First measurement of the Hubble constant from a dark standard siren using the Dark Energy Survey galaxies and the LIGO/Virgo binary black hole merger GW170814. *LIGO Document Control Center*, T1800338, 2018.

[94] B. P. Abbott et al. GWTC-1: A Gravitational-Wave Transient Catalog of Compact Binary Mergers Observed by LIGO and Virgo during the First and Second Observing Runs. 2018.

[95] Calibration Team. O2 C02 calibration Uncertainty Review. *LIGO Document Control Center*, G1800319, 2018.

[96] J. Abadie et al. Calibration of the LIGO Gravitational Wave Detectors in the Fifth Science Run. *Nucl. Instrum. Meth.*, A624:223–240, 2010.

[97] J. Lehman, A. Steiger, N. Tomlin, et al. Planar hyperblack absolute radiometer. *Opt. Express*, 24(23):25911–25921, Nov 2016.

[98] D. Estevez, B. Lieunard, F. Marion, et al. First Tests of a Newtonian Calibrator on an Interferometric Gravitational Wave Detector. *Class. Quant. Grav.*, 35 (23):235009, 2018.

[99] Y. Inoue, S. Haino, N. Kanda, et al. Improving the absolute accuracy of the gravitational wave detectors by combining the photon pressure and gravity field calibrators. *Phys. Rev.*, D98(2):022005, 2018.

[100] M. Pitkin, C. Messenger, and L. Wright. Astrophysical calibration of gravitational-wave detectors. *Phys. Rev.*, D93(6):062002, 2016.

[101] Reed Essick and Daniel E. Holz. Calibrating gravitational-wave detectors with GW170817. 2019.